

REF ID: A71267
AFOSR-TR-89-1284

**DENSE-SPRAY PROPERTIES:
STRUCTURE AND TURBULENCE MODULATION**

by

G. A. Ruff, R. N. Parthasarathy and G. M. Faeth
Gas Dynamics Laboratories
Department of Aerospace Engineering
Ann Arbor, Michigan 48109-2140

Final Report

15 July 1985 - 14 July 1989

Grant No. AFOSR-85-0244
Air Force Office of Scientific Research
Bolling AFB, DC 20332-6448
J. M. Tishkoff, Technical Manager

The views and conclusions contained in this document are those of the authors and should not be interpreted as representing the official policies, or endorsements, either expressed or implied, of the Air Force Office of Scientific Research or the U.S. Government.

August 1989

DTIC
ELECTED
OCT 25 1989
S D
C B

**DENSE-SPRAY PROPERTIES:
STRUCTURE AND TURBULENCE MODULATION**

by

G. A. Ruff, R. N. Parthasarathy and G. M. Faeth
Gas Dynamics Laboratories
Department of Aerospace Engineering
Ann Arbor, Michigan 48109-2140

Final Report

15 July 1985 - 14 July 1989

Grant No. AFOSR-85-0244
Air Force Office of Scientific Research
Bolling AFB, DC 20332-6448
J. M. Tishkoff, Technical Manager

The views and conclusions contained in this document are those of the authors and should not be interpreted as representing the official policies, or endorsements, either expressed or implied, of the Air Force Office of Scientific Research or the U.S. Government.

August 1989

Table of Contents

	<u>Page</u>
Abstract	i
List of Tables.....	iv
List of Figures.....	v
Nomenclature.....	vii
Acknowledgements.....	ix
1. Introduction	1
2. Dense-Spray Structure.....	1
2.1 Introduction	1
2.2 Experimental Methods	5
2.2.1 Apparatus.....	5
2.2.2 Instrumentation	7
2.2.3 Test Conditions	9
2.3 Theoretical Methods.....	11
2.3.1 General Description	11
2.3.2 Formulation	11
2.3.3 Computations	12
2.4 Results and Discussion	12
2.4.1 Flow Visualization.....	12
2.4.2 All-Liquid Core	17
2.4.3 Multiphase Mixing Layer.....	24
2.4.4 Discussion.....	42
2.5 Conclusions	43
3. Turbulence Modulation	45
3.1 Introduction	45
3.2 Experimental Methods	48
3.2.1 Apparatus.....	48
3.2.2 Instrumentation	50
3.2.3 Particle Properties	53
3.2.4 Test Conditions	55
3.3 Theoretical Methods.....	59
3.3.1 Continuous Phase	59
3.3.2 Dispersed Phase	68
3.4 Results and Discussion	71
3.4.1 Apparatus Evaluation.....	71
3.4.2 Continuous-Phase Properties	74
3.4.3 Dispersed-Phase Properties	90
3.5 Summary of Results.....	100
4. Summary of Investigation.....	101
4.1 Articles and Papers	101
4.2 Participants	102
4.3 Oral Presentations	102
References	104

List of Tables

<u>Table</u>	<u>Title</u>	<u>Page</u>
1	Round Liquid Jet Breakup Regimes.....	2
2	Liquid-Jet Test Conditions	10
3	Summary of Self-Induced Particle Motion Properties.....	54
4	Representative Homogeneous Particle-Flow Test Conditions	56
5	Summary of Integral Length and Time Scales	88
6	Ratios of Particle/Liquid Velocity Fluctuations	93
7	Results of Sensitivity Study of Particle Properties	95

List of Figures

<u>Figure</u>	<u>Captions</u>	<u>Page</u>
1	Sketch of the near-injector region of pressure-atomized sprays.....	3
2	Sketch of the test apparatus.....	6
3	Flash photographs of the 9.5 mm diameter injector for fully-developed flow: (a) first wind-induced breakup; (b) second wind-induced breakup; (c) atomization breakup.....	13
4	Time-averaged liquid volume fractions along axis for fully-developed flow	18
5	Time-averaged liquid volume fractions along axis for slug flow	19
6	Radial profiles of time-averaged liquid volume fractions for fully-developed flow and atomization breakup (19.1 mm diameter injector) ...	21
7	Radial profiles of time-averaged liquid volume fractions for fully-developed flow and atomization breakup (9.5 mm diameter injector)....	22
8	Radial profiles of time-averaged liquid volume fractions for slug flow and atomization breakup (9.5 mm diameter injector).....	23
9	Hologram reconstruction near the outer edge of the multiphase mixing layer: fully-developed flow, $x/d = 12.5$, $r/x = 0.150$	26
10	Hologram reconstruction near the middle of the multiphase mixing layer: fully-developed flow, $x/d = 12.5$, $r/x = 0.100$	27
11	Hologram reconstruction near the inner edge of the multiphase mixing layer: fully-developed flow, $x/d = 12.5$, $r/x = 0.050$	28
12	Dispersed-phase properties for fully-developed flow and atomization breakup at $x/d = 12.5$	29
13	Dispersed-phase properties for fully-developed flow and atomization breakup at $x/d = 25$	30
14	Dispersed-phase properties for fully-developed flow and atomization breakup at $x/d = 50$	31
15	Dispersed-phase properties for fully-developed flow and atomization breakup at $x/d = 100$	32
16	Dispersed-phase properties for slug flow and atomization breakup at $x/d = 12.5$	34
17	Dispersed-phase properties for slug flow and atomization breakup at $x/d = 25$	35

<u>Figure</u>	<u>Captions</u>	<u>Page</u>
18	Dispersed-phase properties for slug flow and atomization breakup at $x/d = 50$	36
19	Dispersed-phase properties for slug flow and atomization breakup at $x/d = 100$	37
20	Liquid volume fractions and fluxes at various distances from the injector for atomization breakup and fully-developed and slug flow.....	39
21	Entrainment rates as a function of distance from the injector for fully-developed and slug flow.....	41
22	Turbulence modulation in a particle-laden jet.....	46
23	Sketch of homogeneous particle-flow apparatus.....	49
24	Individual particle flow field	64
25	Particle number flux distribution ($d_p = 1.0$ mm).....	72
26	Liquid streamwise velocity fluctuation distribution ($d_p = 1.0$ mm).....	73
27	Liquid velocity fluctuations.....	75
28	Probability density function of liquid streamwise velocity fluctuations...	78
29	Probability density function of liquid crosstream velocity fluctuations ...	79
30	Temporal spectral density of liquid streamwise velocity fluctuations	80
31	Temporal spectral density of liquid crosstream velocity fluctuations.....	81
32	Lateral spatial correlation of liquid streamwise velocity fluctuations	85
33	Longitudinal spatial correlation of liquid streamwise velocity fluctuations	87
34	Particle velocities	91
35	Probability density function of particle streamwise velocity fluctuations .	97
36	Probability density function of particle crosstream velocity fluctuations..	98

Nomenclature

<u>Symbol</u>	<u>Description</u>
a	acceleration of gravity
a_k	random shock in stochastic simulation
A_{ij}	weighting factor in stochastic simulation
C_D	particle drag coefficient
d	diameter of injector
d_{\max}, d_{\min}	maximum and minimum diameters of liquid elements
d_p	particle diameter
e_p	drop or liquid element effective ellipticity
$E_G(f)$	temporal spectral density of G
f	mixture fraction, frequency
g	liquid flux
$g(r, \phi, t)$	individual particle effect
$G(t)$	effect of all particles
k	turbulence kinetic energy
ℓ	characteristic wake diameter
ℓ_K	Kolmogorov length scale
ℓ_p	mean particle spacing
L	injector passage length
L_{ux}, L_{uy}	longitudinal and lateral integral length scale of streamwise velocity fluctuations
M_A	acceleration modulus
n	number of particles per unit time
n''	particle number flux
Oh	Ohnesorge number
$P(\phi)$	probability density function of ϕ
r	radial distance
r_0	distance to point of observation from center of sphere
Re	Reynolds number
$Re\ell$	local wake Reynolds number
SMD	Sauter mean diameter
t	time
t_0	time at start of integration
T_0, T_∞	lower and upper limits of integration in wake

<u>Symbol</u>	<u>Description</u>
T_u, T_v	integral time scale of streamwise and crosstream velocity fluctuations
u, v, w	streamwise, radial and tangential velocities
u_i, u_{ri}	velocity and relative velocity in the i-th direction
U_∞	terminal velocity of particle
We_i	Weber number based on density of phase i
x, y, z	streamwise and crosstream distances
x_i	component of distance in the i-th direction
X, Y	position in streamwise and crosstream directions
α	volume fraction
Δ_A, Δ_H	correction of virtual mass and Basset history forces
ϵ	rate dissipation of turbulence kinetic energy
θ	momentum diameter of wake
μ	viscosity
ν	kinematic viscosity
ρ	density
σ	surface tension
τ	time delay
ϕ	azimuthal angle, generic property
<u>Subscripts</u>	
a	air property
av	average property
c	centerline value
f	liquid property
g	gas property
mw	effect due to mean wake properties
p	particle or drop property
pc	effect due to potential flow region
s	effect due to self-induced particle motion
tw	effect due to wake turbulence
o	initial condition
∞	ambient condition
<u>Superscripts</u>	
$(\cdot)(\cdot)'$	time-averaged mean and r.m.s. fluctuating quantity
$(\cdot)(\cdot)''$	Favre-averaged mean and r.m.s. fluctuating quantity

Acknowledgements

The authors wish to acknowledge helpful discussions with L. P. Bernal, W.J.A. Dahm, D. R. Glass and W. W. Willmarth of the University of Michigan; as well as the assistance of A. D. Sagar during the early states of the investigation. We also wish to acknowledge the contributions of the staff of the Gas Dynamics Laboratories at the University of Michigan: C. J. Iott, W. C. Eaton, T. L. Griffin and G. L. Gould for assisting apparatus development; and S. C. Bauerle for helping to prepare this report.

This research was sponsored by the Air Force Office of Scientific Research, Air Force Systems Command, under grant No. AFOSR-85-0244. The U.S. Government is authorized to reproduce and distribute copies of this report for Governmental Purposes notwithstanding any copyright notation thereon.

1. INTRODUCTION

The potential value of rational design procedures for liquid-fueled combustors has motivated numerous efforts to develop methods for analyzing spray evaporation and combustion processes. The goal is to reduce the time and cost of cut-and-try combustor development. This investigation seeks to contribute to the development of this methodology by studying several fundamental phenomena associated with sprays — particularly the dense-spray region near the exit of the fuel injector passage. The research has application to airbreathing propulsion systems, e.g., liquid-fueled primary combustors and afterburners; liquid-fueled rocket engines; fuel-injected internal-combustion engines; diesel engines; furnaces, etc. Finally, the research also involves examination of turbulence/dispersed-phase interactions that are present for a wider class of dispersed turbulent flows, including processes relevant to solid rocket motors, particle-laden exhaust plumes, sedimentation, and atmospheric turbulence associated with precipitation.

The investigation is divided into two main tasks relevant to the near-injector dense region of sprays, as follows: (1) direct consideration of the structure of the near-injector dense-spray region of pressure-atomized sprays; and (2) the modification of the turbulence properties of the continuous phase by direct action of the dispersed phase (often called "turbulence modulation"). This is a final report of the investigation. Other descriptions of the research can be found in Parthasarathy (1989), Parthasarathy & Faeth (1987, 1987a, 1987b, 1988), Parthasarathy et al. (1986, 1988), Ruff & Faeth (1987), and Ruff et al. (1987, 1989, 1989a).

The report begins with consideration of the structure of dense sprays, followed by discussion of turbulence modulation. The report concludes with a summary of articles, participants and oral presentations of the study.

2. DENSE-SPRAY STRUCTURE

2.1 Introduction

The investigation of dense-spray phenomena considered the near-injector region of nonevaporating, pressure-atomized, round water jets injected into still air. Further definition of the flow requires consideration of breakup regimes. Ranz (1958) prescribed four regimes of liquid jet breakup (drip, Rayleigh, wind-induced and atomization), based on the liquid and gas Weber numbers of the flow, which are defined as follows:

$$We_{(f \text{ or } g)} = (\rho_f \text{ or } \rho_g) u_0^2 d / \sigma \quad (2.1)$$

The properties of the four regimes, and their breakup criteria, are summarized in Table 1. Reitz (1978) further subdivides wind-induced breakup into first and second wind-induced breakup regimes, which are also noted in the table. The present investigation was limited to the wind-induced and atomization breakup regimes, since they are the most important regimes for practical applications. In particular, the second-wind-induced and atomization breakup regimes involve breakup near or at the injector exit, respectively, yielding drop diameters much smaller than the injector passage diameter — attributes that are needed for high-intensity combustion processes.

There are several flow regions within a spray when it is operating in the atomization breakup regime, as illustrated in Fig. 1. Within the injector, and far downstream (if the

REPORT DOCUMENTATION PAGE			
1a. REPORT SECURITY CLASSIFICATION Unclassified	1b. RESTRICTIVE MARKINGS		
2a. SECURITY CLASSIFICATION AUTHORITY	3. DISTRIBUTION/AVAILABILITY OF REPORT Approved for public release; distribution is unlimited.		
2b. DECLASSIFICATION/DOWNGRADING SCHEDULE			
4. PERFORMING ORGANIZATION REPORT NUMBER(S)	5. MONITORING ORGANIZATION REPORT NUMBER(S) AFOSR-TR- 89-1284		
6a. NAME OF PERFORMING ORGANIZATION Dept. of Aerospace Engineering The University of Michigan	6b. OFFICE SYMBOL (If applicable)	7a. NAME OF MONITORING ORGANIZATION AFOSR/NA	
6c. ADDRESS (City, State, and ZIP Code) 217 Aerospace Engineering Building Ann Arbor, MI 48109-2140	7b. ADDRESS (City, State, and ZIP Code) Building 410, Bolling AFB DC 20332-6448		
8a. NAME OF FUNDING/SPONSORING ORGANIZATION AFOSR/NA	8b. OFFICE SYMBOL (If applicable) <i>NH</i>	9. PROCUREMENT INSTRUMENT IDENTIFICATION NUMBER AFOSR-85-0244	
9c. ADDRESS (City, State, and ZIP Code) Building 410, Bolling AFB DC 20332-6448	10. SOURCE OF FUNDING NUMBERS		
	PROGRAM ELEMENT NO. 61102F	PROJECT NO. 2308	TASK NO. A2
	WORK UNIT ACCESSION NO.		
11. TITLE (Include Security Classification) (U) Dense-Spray Properties: Structure and Turbulence Modulation			
12. PERSONAL AUTHOR(S) G. A. Ruff, R. N. Parthasarathy and G. M. Faeth			
13a. TYPE OF REPORT Final Technical	13b. TIME COVERED FROM 7/15/85 TO 7/15/89	14. DATE OF REPORT (Year, Month, Day) 15 August 1989	15. PAGE COUNT 118
16. SUPPLEMENTARY NOTATION			
17. COSATI CODES		18. SUBJECT TERMS (Continue on reverse if necessary and identify by block number) Multiphase flow Sprays Particle-laden flow	
FIELD	GROUP	SUB-GROUP	
19. ABSTRACT (Continue on reverse if necessary and identify by block number) A theoretical and experimental study of aspects of dense sprays is described, considering: the structure and mixing properties of the near-injector, dense-spray region of pressure-atomized sprays; and the direct effect of particle (drop) motion on the turbulence properties of multiphase flows (which is often called turbulence modulation). The structure of dense sprays was studied using large-scale (9.5 and 19.1 mm jet exit diameters) water sprays in still air. Measurements included: flow visualization using flash photography; liquid volume fractions using gamma-ray absorption; streamwise mean and fluctuating velocities at the injector exit, and entrainment velocities, using laser velocimetry; and dispersed-phase properties using single- and double-flash holography. Predictions based on the locally-homogeneous flow (LHF) approximation of multiphase			
20. DISTRIBUTION/AVAILABILITY OF ABSTRACT <input checked="" type="checkbox"/> UNCLASSIFIED/UNLIMITED <input checked="" type="checkbox"/> SAME AS RPT <input type="checkbox"/> DTIC USERS		21. ABSTRACT SECURITY CLASSIFICATION Unclassified	
22a. NAME OF RESPONSIBLE INDIVIDUAL Julian M Tishkoff		22b. TELEPHONE (Include Area Code) (202) 767- <i>0463</i>	22c. OFFICE SYMBOL AFOSR/NA

DD Form 1473, JUN 86

Previous editions are obsolete.

SECURITY CLASSIFICATION OF THIS PAGE

Unclassified

89 10 24 094

19. Abstract (continued)

flow theory were also evaluated using the measurements. Measurements showed that mixing was strongly influenced by the degree of flow development at the injector exit and the breakup regime: fully-developed flow and atomization breakup yielded the fastest mixing rates. The near-injector region involved an all-liquid core surrounded by a multiphase mixing layer. The inner portion of the mixing layer contained large irregularly-shaped liquid elements and drops while the proportion of spherical drops increased and drop sizes decreased with increasing radial distance. The all-liquid core and the large liquid elements caused mean liquid volume fractions to be high near the axis. However, the gas-containing region of the mixing layer was relatively dilute at each instant. The velocities of large drops were generally much larger than small drops, providing direct evidence of significant separated-flow effects in the flow. The degree of flow development at the jet exit also had a substantial effect on the dispersed phase in the mixing layer, with increased turbulence levels increasing the number and size of large irregular liquid elements through distortion of the surface of the all liquid core. This enhanced rates of removal of liquid from the core as well as lateral mixing of liquid in the multiphase atomization breakup when liquid volume fractions were greater than 0.2 but were not satisfactory for other breakup regimes or in regions where the sprays were dilute and separated-flow effects begin to dominate the process.

Turbulence modulation was studied by considering nearly monodisperse spherical glass particles falling in a stagnant water bath, where effects of turbulence modulation were responsible for the entire turbulence field. Measurements included phase velocities, as well as the temporal and spatial correlations of continuous-phase velocities, using a two-point phase-discriminating laser velocimeter; and calibration of particle motion properties using motion-picture shadowgraphs. Flow properties were analyzed using stochastic methods, assuming linear superposition of randomly-arriving particle velocity fields for liquid-phase properties and performing random-walk calculations based on statistical time-series methods for particle trajectories. Liquid velocity fluctuations were highly anisotropic (the ratio of streamwise to crosstream fluctuations was roughly 2:1) and could be correlated solely as a function of the rate of dissipation of kinetic energy in the liquid. Correlation coefficients and spectra were independent of particle loading, with temporal spectra yielding a large range of frequencies, even at low particle Reynolds numbers, since both mean and fluctuating velocities in the particle wakes contribute to the spectra because particle arrivals are random. The stochastic analysis predicted many of the features of the continuous phase but must be improved to obtain better estimates of spatial and temporal scales. The particles exhibited self-induced lateral motion due to eddy-shedding and irregularities of shape and large streamwise velocity fluctuations due to varying terminal velocities because of size variations, as well as effects of turbulent dispersion. After accounting for effects of self-induced motion and particle size variations, the stochastic simulation predicted particle velocities reasonably well.

Table 1 Round Liquid Jet Breakup Regimes

Breakup Regime	Properties		Breakup Criteria ^a	
	Location	Drop Diameter	We _f	We _g
Drip	x = 0	> d	< 8	< 0.4
Rayleigh	x > 0	> d	> 8	< 0.4
Wind-Induced	x > 0		> 8	0.4-4.13 ^b
First		0.1d-d		
Second		< d		
Atomization	x = 0	<< d	> 8	13 ^b <

^aCriteria due to Ranz (1958).

^bMiesse (1955) recommends 40.3 instead of 13 for transition to atomization.

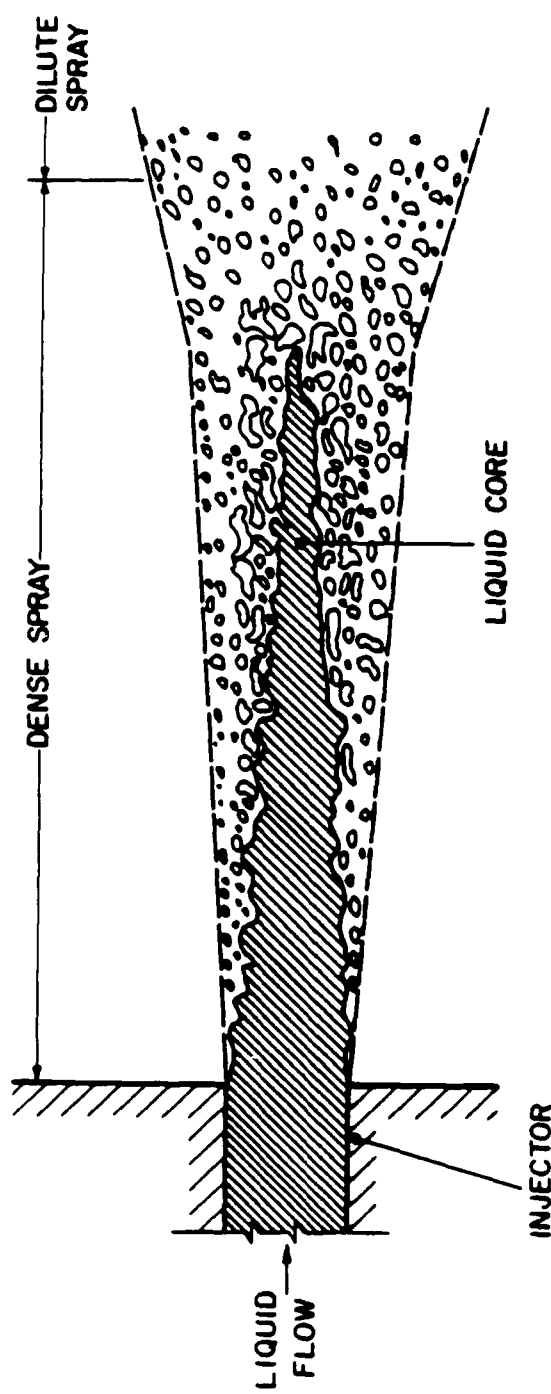


Figure 1 Sketch of the near-injector region of pressure-atomized sprays.

liquid is evaporating) we have single-phase flows. The dense-spray region is near the injector exit and involves an all-liquid core surrounded by a multiphase mixing layer. The portion of the mixing layer near the liquid core contains a complex flow configuration that results from removal of liquid from the core as part of the atomization process: globules of liquid, ligaments and drops. The outer edge of the mixing layer, however, has characteristics similar to a dilute spray, consisting of rather widely spaced spherical drops with liquid volume fractions less than 1 percent. The boundary between the dense- and dilute-spray regions is not well defined. However, most studies of dilute sprays have been limited to the region downstream of the all-liquid core, as illustrated in Fig. 1. This region can be quite far from the injector, e.g., liquid cores can extend 200-400 injector diameters from the jet exit for injection into atmospheric-pressure gases. Thus, although little is known about the dense spray region, processes in dense sprays clearly have an important influence on the structure and mixing properties of sprays.

Past studies of dense sprays have been reviewed by Faeth (1977, 1983, 1987) and only the main features of earlier work will be considered here. Earlier work has been relatively limited due to the difficulties of making measurements in a multiphase flow where liquid volume fractions vary over a wide range. Phinney (1973), Hiroyasu et al. (1982) and Chehroudi et al. (1985) have attempted to measure the length of the all-liquid core, however, their results scatter widely and are not in good agreement.

In an attempt to circumvent the difficulties of dealing with a flow having widely varying phase topography and a variety of physical phenomena — collisions, breakup, interphase transport with closely-spaced dispersed-phase elements, etc. — use of the locally-homogeneous flow (LHF) approximation to analyze dense sprays has been studied by a number of workers. The LHF approximation implies that interphase transport rates are infinitely fast, so that relative velocities between the phases are small in comparison to flow velocities and local thermodynamic equilibrium is maintained, i.e., it is assumed that the development of a dense spray is controlled by turbulent mixing. The effectiveness of this approach, however, is controversial. Bracco (1983) and Wu et al. (1983, 1984) report measurements of spray angles and drop velocities in nonevaporating pressure-atomized sprays at high pressures, concluding that LHF analysis was effective for their test conditions. On the other hand, Faeth (1983, 1987), Mao et al. (1980, 1981), Shearer et al. (1979), Shuen et al. (1983, 1985, 1986), Solomon et al. (1985, 1985a, 1985b), Sun & Faeth (1986, 1986a), Sun et al. (1986) and Parthasarathy & Faeth (1987), all working in this laboratory, generally found that the LHF approach overestimates the rate of development of multiphase jets. Even findings in high-pressure sprays suggested problems with LHF analysis, since drop inertia is significant in the rapidly decelerating flow field of typical sprays (Mao et al., 1980, 1981). Experimental evidence on both sides of the controversy generally comes from dilute portions of the spray, however, and its relevance to dense-spray processes is questionable.

The present investigation was undertaken to help resolve controversies concerning the structure and extent of the dense spray region, as well as the effectiveness of the LHF approximation for analyzing dense sprays. The objectives were to complete nonintrusive measurements of spray structure near the injector in order to better understand the breakup and mixing properties of the flow. The experiments involved nonevaporating water jets, injected into still air at atmospheric pressure, and operating within the wind-induced and atomization breakup regimes. Measurements included: flow visualization using flash photography, liquid volume fractions using gamma-ray absorption, properties of the dispersed phase (liquid element sizes and velocities and liquid volume fractions) within the multiphase mixing layer using single- and double-flash holography, and air entrainment rates and mean and fluctuating liquid velocities at the injector exit using laser velocimetry. Measurements were compared with predictions based on the LHF approximation along the

lines of Mao et al. (1980, 1981), after calibration of model parameters using measurements in single-phase flows (Faeth, 1987).

This portion of the report begins with descriptions of theoretical and experimental methods. Results are then considered, treating flow visualization, the properties of the all-liquid core, and the properties of the multiphase mixing layer, in turn.

2.2 Experimental Methods

2.2.1 Apparatus

Issues that were studied relate to the dynamics of turbulent spray mixing processes, which are not thought to be strongly influenced by the injector diameter. Therefore, large-scale (9.5 and 19.1 mm injector diameters) jets were used in order to get adequate spatial resolution for observations. The experimental arrangement is illustrated in Fig. 2. Water was used as the test liquid, injected vertically downward in still air. The water was collected in a tub at the downstream end of the spray and discharged to a drain. Baffles within the tub eliminated splashing of liquid back up into the area where measurements were made.

City water was supplied to the injector using a centrifugal water pump (Pennsylvania Pump and Compressor Co., Type 2-1/2" 2-S OMSR). The rate of water flow was adjusted using a bypass system and measured with an Oilgear Co. PV meter (Type 15T TD2, Model PL15C-2A1S/UNO-25-0100-005-003) with a digital readout. The flow meter was calibrated by collecting water for timed intervals.

Instrumentation was mounted rigidly; therefore, the injector was traversed (1 m horizontally and 2 m vertically) to measure flow structure. The injector was mounted on a plate which traversed horizontally on a linear bearing assembly (25 mm diameter) whose position was adjusted by a Velmex, Inc. Unislide lead screw and stepping motor (Models B4036Q1J, M092-FD08 and 4-8311). The horizontal position was recorded using a Velmex, Inc. Digital Position Readout (4-8518), readable to 5 μm . The vertical traverse used 25 mm diameter linear bearings also, mounted on two I-beams which were attached at the ceiling and the floor. The vertical position was set with a cable and winch, since only fixed axial stations were considered. The vertical position was measured with a ruler, accurate to 0.5 mm.

Three injectors were used: a slug-flow injector having an exit diameter of 9.5 mm and two fully-developed flow injectors having diameters of 9.5 and 19.1 mm. The slug-flow injector consisted of a honeycomb flow straightener (1.6 mm cells, 25 mm long), two screens to calm the flow (0.018 mm diameter wire, 16 \times 16 square mesh), followed by a smooth converging section from the 35 mm diameter water supply tube to the 9.5 mm exit diameter. The converging section provided a uniform exit flow, following a contour prescribed by Smith & Wang (1944). The fully-developed flow injectors had a flow straightener similar to the slug flow injector, followed by a simple circular converging section to a constant-area passage having a length of 41 passage diameters. Both arrangements provide no swirl at the jet exit, while minimizing problems of cavitation within the passage. Measurements at the injector exit showed that the designs provide the desired slug and fully-developed pipe flow exit conditions (Ruff et al., 1987, 1988).

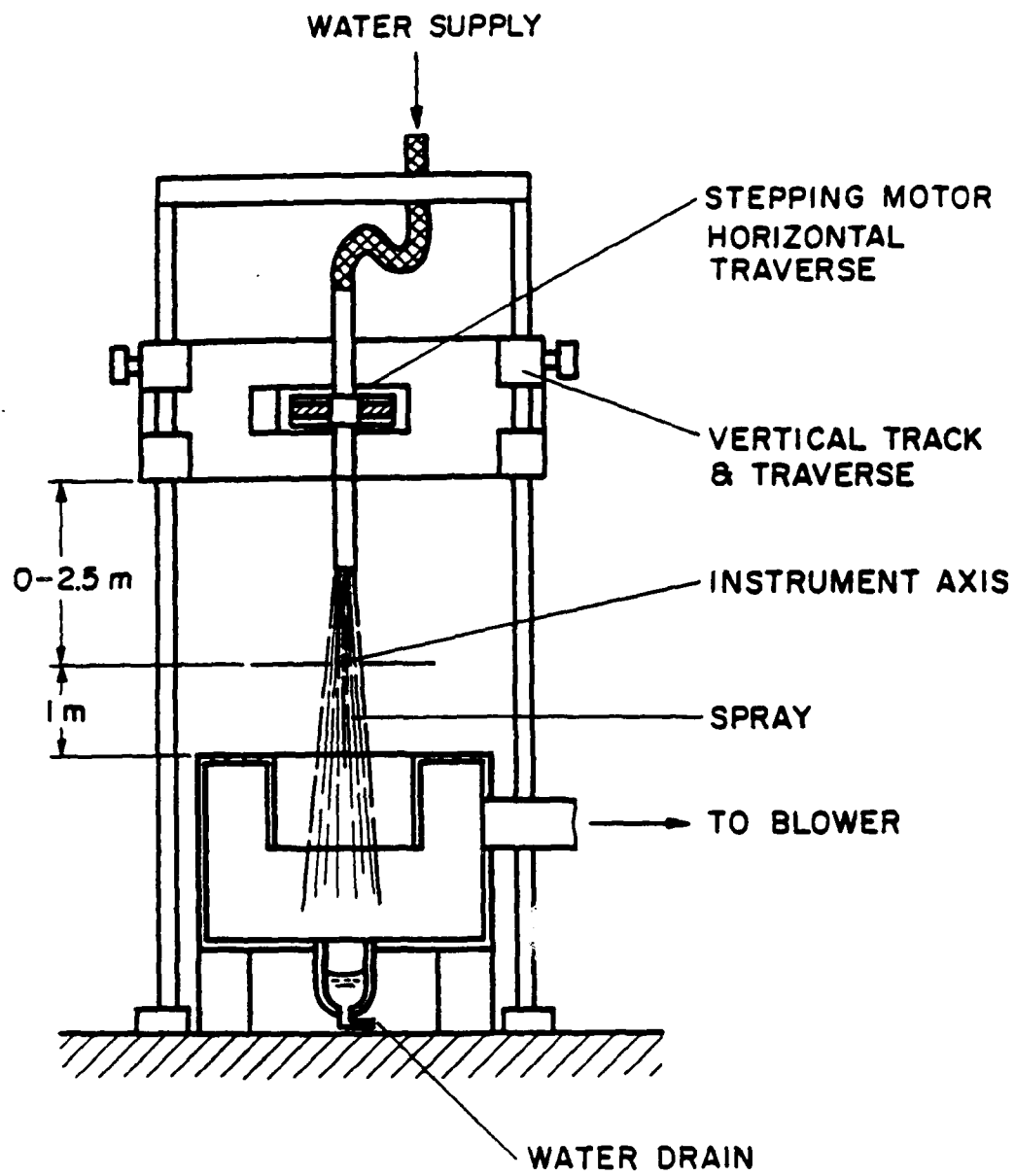


Figure 2 Sketch of the test apparatus.

2.2.2 Instrumentation

Measurements included the following: flow visualization using flash photography, liquid volume fractions using gamma-ray absorption, streamwise mean and fluctuating velocities at the injector exit and entrainment velocities using laser velocimetry, and dispersed-phase properties in the multiphase mixing layer using single- and double-flash holography.

Flow Visualization. Flash photography was based on a Xenon Corporation High-Intensity Micropulse System (Model 457A) which can provide a 10 J light pulse with a 1 μ s duration. Photographs were obtained in a darkened room using an open camera shutter and with the flash lamp controlling the time of exposure. The photographs were taken with a 4 \times 5 Speed Graphic camera using Polaroid Type 57, 3000 ASA black and white film. The camera was directed normal to the spray axis, from a position near the flash lamp. The jets were quite long. Therefore, they were photographed in sections, each roughly 250 mm long, in order to adequately resolve the flow.

Gamma-Ray Absorption. The general design of the gamma-ray absorption system followed Gomi and Hasegawa (1984), Ohba (1979) and Schrock (1969). An Iodine 125 isotope source (2 mCi, emitting primarily at 27.47 keV) provided a soft gamma-ray source, yielding optimum absorption levels in order to minimize experimental uncertainties for the absorption measurements. The source was placed in a lead casket with a 1.6 mm diameter \times 13 mm long collimating aperture. The front of the casket was fitted with a 12 mm thick removable lead shield to cover the source during periods when it was not in use. Gamma rays passing through the flow were detected and counted using a Bicron Model 1 \times M.040/1.54 X-ray probe. A lead aperture (1.5-6 mm in diameter, depending on position, and 12 mm long) was placed in front of the detector to define the path observed through the flow. The data acquisition system used an EG&G Ortec single-channel analyzer and counter/timer (Models 556, 590A, 970). The energy window of the analyzer was centered at 27.5 keV to minimize spurious counts due to background radiation and Compton scattering (the latter effect was not large, however, in the present energy range). Detector output was stored and processed using an IBM AT personal computer.

Absorption measurements were made for 30-60 parallel paths through the flow. These measurements were very symmetric; therefore, measurements on both sides of the axis were averaged and smoothed to provide a single set of absorption measurements for a given cross-section of the flow. The line-of-sight measurements were deconvoluted, following Santoro et al. (1981), to yield radial distributions of void fraction. Schrock (1969) and Gomi and Hasegawa (1984) point out that this method has a fundamental uncertainty depending on whether parallel or normal liquid laminae are assumed. However, the narrow absorption paths used during the present experiments reduced this effect to less than 5 percent.

The gamma-ray absorption system was calibrated using water-filled cells to measure the linear absorption coefficient. Data involves 30-60 absorption measurements (varying with the width of the flow) and ca. 25,000 counts at each position. Richardson extrapolation of these results to their limits indicated experimental uncertainties of centerline void fraction less than 5 percent, with proportionately higher values elsewhere.

Laser Velocimetry. Mean and fluctuating liquid velocities at the injector exit and mean entrainment rates were measured by laser velocimetry (LV). The green line (514.5 nm) of an argon-ion laser (4W, Coherent, INNOVA 90-4) was used in a dual-beam, frequency-shifted (40 MHz Bragg cell, TSI model 9180-12) arrangement, to eliminate effects of directional bias and ambiguity. The LV signal was collected using a

photomultiplier (TSI Model 9160) and processed using a burst counter (TSI Model 1990C). All measurements involved low burst densities (one scattering particle in the measuring volume) and high data densities (time between validated signals small in comparison to integral time scales). Therefore, the analog output of the processor was time-averaged to yield unbiased time averages.

LV measurements of injector exit conditions were obtained for injection into a water-filled windowed chamber. The initial beam spacing was 50 mm, the sending and receiving optics had 250 mm focal lengths, and signal detection was 30 deg off-axis in the forward-scattering direction. This yielded a measuring volume having a diameter of 110 μm and a length of 220 μm , which was positioned in a plane 0.1 injector diameters from the injector exit. The local water supply contained adequate natural seeding. Streamwise and radial velocities were measured by orienting the laser beam plane appropriately. Experimental uncertainties (95 percent confidence) were largely governed by finite sampling times, and were less than 5 and 10 percent for mean and fluctuating velocities at the axis, and proportionately higher elsewhere.

The only change in the optical configuration for the entrainment measurements was the use of 600 mm focal length sending and receiving optics, yielding a measuring volume having a diameter of 260 μm and a length of 520 μm . Mean streamwise and radial entrainment velocities were measured near the edge of the flow, with the entire test cell seeded with condensed bay oil particles (ca. 1 μm diameter). These measurements were integrated to provide entrainment rates, with experimental uncertainties (95 percent confidence) estimated to be less than 25 percent.

Holography. An off-axis holographic arrangement was used based on the Spectron Development Laboratories Model HTRC-5000 system, with an angle of 28° between the object and reference beams. The system was modified, however, to improve performance in dense sprays. In particular, dense sprays require large light intensities so that the flow can be penetrated, and high magnification, since small drops are of interest. This was accomplished by reducing the diameter of the object beam through the spray and then subsequently expanding it (7-8:1) back to the same size as the reference beam (85 mm diameter) when the two signals were optically mixed to form a hologram. The reference beam was directed past the spray within a 300 mm diameter tube to reduce optical noise from small drops in the environment caused by the spray collection system. The holograms were produced using a ruby laser that deposited 50 mJ in roughly 20 ns. The short laser pulse time stopped the motion adequately so that drops as small as 2 μm in diameter could be observed and drops as small as 5 μm in diameter could be measured. The laser could be double pulsed with pulse separation times as short as 2 μs . This yielded holograms that could be reconstructed to show the object field at two instants of time, providing a means of measuring liquid element velocities. The holograms were obtained in a darkened room using AGFA 8E75HD-NAH unbacked photographic film plates with a 100 \times 125 mm film format.

The holograms were reconstructed using a 15 mW cw HeNe laser that was collimated at a 60 mm diameter and passed through the developed hologram to provide a real image of the spray in front of the hologram. The properties of the reconstructed spray were observed with an MTI Model 65 video camera with optics that provided fields of view of roughly 1 \times 1.2 mm and 2.5 \times 3 mm. The larger field of view was more convenient for analyzing ligaments and other large liquid elements. Computer controlled x-y traversing of the hologram (with a 1 μm resolution) and z traversing of the video camera (with 5 μm resolution) allowed the region crossed by the object beam to be studied. The video image was analyzed using a Gould FD 5000 Image Processing System. A 1 mm diameter pin

located in the region being studied provided a size and position reference point in the reconstructed image of the spray.

Drops and other more-or-less ellipsoidal-shaped liquid elements were sized by finding the maximum and minimum diameter through the centroid of the image. Assuming that the liquid element was ellipsoidal, its diameter was taken to be the diameter of an ellipsoid having the same volume, i.e., $d_p^3 = d_{\min}^2 d_{\max}$. The shape of the element was characterized by its ellipticity, defined as $e_p = d_{\max}/d_{\min}$. This approach was not appropriate for elongated liquid elements or ligaments where the centroid of the image often fell outside the boundaries of the image or where there were several necked-in points along the length of the element. In these cases, the cross-sectional area and perimeter of the image were measured and the maximum and minimum diameters of an ellipsoid having the same cross-sectional area and perimeter were computed. Given these parameters the effective diameter and ellipticity were calculated in the same manner as for drops. Results at each position in the flow were summed to find the Sauter mean diameter (SMD), the volume-averaged ellipticity, and the liquid volume fraction.

Velocity measurements were based on the motion of the centroid of the image and were correlated as a function of diameter using a least-squares fit. This allowed plots of drop velocities at fixed diameters across the width of the mixing layer while making maximum use of data on the holograms at each position. Knowing the volume and velocity of liquid elements in the flow, liquid fluxes could be computed in a straightforward manner as well.

Measurements were made at $x/d = 12.5, 25, 50$ and 100 for r/x extending from the surface of the liquid core to near the edge of the multiphase mixing layer. Measurements at each location were obtained from a $6 \times 6 \times 4$ mm volume, averaging results over no less than three holograms. The data were spatially averaged over the width of the measuring volumes, or $\pm 1/2$ the distance between adjacent radial positions, whichever was less. Measurements involved analysis of 50-150 objects for $r/x \leq 0.075$ and 150-500 objects for $r/x \geq 0.100$, with fewer objects nearer the liquid core reflecting the fact that liquid elements were generally much larger in this region.

Experimental uncertainties were generally dominated by sampling limitations rather than the resolution of liquid element properties from the reconstructed holograms. Estimates of experimental uncertainties (95 percent confidence) are as follows: Sauter mean diameter less than 10 percent, volume-averaged ellipticity less than 15 percent, liquid element velocities less than 20 percent, liquid volume fractions less than 15 percent, and liquid fluxes less than 25 percent.

2.2.3 Test Conditions

Test conditions are summarized in Table 2. Three conditions were examined for each injector, corresponding to first wind-induced, second wind-induced, and atomization breakup. These determinations were based on present observations of the flows. Ranz (1958) suggests $We_f > 8$ and $0.4 < We_g < 13$ for wind-induced breakup; and $We_f > 8$ and $We_g > 13$ for atomization; while Miesse (1955) suggests $We_g > 40.3$ for atomization. The results of Table 2 are in rough accord with these criteria, even though present injectors are an order of magnitude larger than those used by Ranz (1958) and Miesse (1955). The main difference is that the present second wind-induced conditions are slightly beyond the estimated transitions to atomization; however, in these cases, breakup was relatively close to the injector ($x/d \sim 3$) and was not far removed from atomization conditions.

Table 2 Summary of Liquid Jet Test Conditions^a

Exit Diameter (mm)	Injector Pressure Drop (kPa)	Flow Rate (kg/s)	Re_f $\times 10^{-5}$	We_f $\times 10^{-3}$	We_g	Oh $\times 10^4$	Breakup Regime
9.5 ^b	80	0.39	0.52	3.9	4.6	12.1	1 st Wind-Induced
	420	1.55	2.07	62.1	72.9	12.1	2 nd Wind-Induced
	2520	3.99	5.34	411.5	492.8	12.1	Atomization
19.1 ^c	30	1.32	0.88	5.6	6.6	8.6	1 st Wind-Induced
	360	4.50	3.00	65.4	76.7	8.6	2 nd Wind-Induced
	2070	11.00	7.32	390.7	458.6	8.6	Atomization

^aPressure-atomized water injected vertically downward into still air at 98.8 kPa.^bBoth slug flow and fully-developed pipe flow initial conditions.^cOnly fully-developed pipe flow initial condition.

2.3 Theoretical Methods

2.3.1 General Description

The LHF analysis was similar to past work in this laboratory (Faeth 1983, 1987), aside from changes needed to treat the specifics of water injection into air. In addition to the LHF approximation, the major assumptions of the analysis are as follows: steady (in the mean) axisymmetric flow with no swirl; boundary-layer approximations apply; negligible kinetic energy and viscous dissipation of the mean flow; buoyancy only affects the mean flow; and equal exchange coefficients of all species and phases. With the exception of the last, these assumptions are either conditions of the experiments or are justified by successful use in the past (Faeth 1983, 1987; Jeng & Faeth, 1984). The assumption of equal exchange coefficients of both phases is suspect wherever molecular transport is important, since molecular transport of finite-sized dispersed-phase elements is small. However, molecular transport is not very important at the high Reynolds numbers of present flows. Therefore, this approximation does not introduce serious limitations in comparison to the general uncertainties of LHF analysis for multiphase jets.

2.3.2 Formulation.

Under the present assumptions, all scalar properties are only functions of the mixture fraction (mixture fraction is defined as the fraction of mass at a point that originated from the injector). This allowed use of the conserved-scalar formalism for scalar properties, similar to Lockwood and Naguib (1975), but based on mass-weighted (Favre) averages, following Bilger (1976).

Governing equations are solved for conservation of mass, streamwise mean momentum, mean mixture fraction, turbulence kinetic energy, rate of dissipation of turbulence kinetic energy, and mean-squared mixture fraction fluctuations (see Faeth (1983, 1987) for the specific formulation and empirical constants). The present approach was successfully calibrated for a variety of constant and variable density single-phase round jets (Jeng & Faeth, 1984). The formulation and constants, however, are not very different from those used by Lockwood & Naguib (1975).

Initial conditions for the calculations were specified at the injector exit, based on the LV velocity measurements. It was found that the long injector passages yielded properties at the injector exit that were equivalent to fully-developed pipe flow. Rather than interpolate from the measurement plane (at $x/d = 0.1$), \bar{u} , k and ϵ were taken from Hinze (1975) and Schlichting (1975), while $f = 1$ and $g = 0$ by definition at the injector exit. (Note that Favre- and time-averaged quantities are identical for the single-phase flow at the injector exit.)

Flow properties were uniform at the exit of the slug-flow injector, except for a narrow layer that could not be resolved using the LV. In the constant property portion of the flow \bar{u} was known from the measurements; k was computed from measurements of \bar{u}^2 and \bar{v}^2 , assuming $\bar{w}^2 = \bar{v}^2$; and ϵ was approximated as $1.274 \times 10^{-4} \bar{u}^3/d$, similar to past work (Faeth 1983, 1987). Properties in the boundary-layer along the wall were estimated for a range of L/d , bounding reasonable estimates of flow-development lengths, assuming clean entry and no *vena contracta*. These properties were obtained from Schlichting (1979).

Under present assumptions, scalar properties are functions only of mixture fraction, called state relationships (Faeth 1983, 1985). State relationships were found by straightforward thermodynamic calculations for adiabatic mixing and equilibration of various

mixtures of injected and ambient fluid. Calculations were completed for the limiting conditions of dry and water vapor saturated ambient air. The effect of drop evaporation for dry air, however, was small. Therefore, only a water-vapor-saturated environment will be considered here.

When the ambient air is fully saturated, there is no tendency for the injected water to evaporate, and the flow corresponds to an isothermal mixing process of the gas and liquid, each having constant densities. Thus, variable-density effects are only due to mixing of the phases under the LHF approximation. Then the instantaneous mixture fraction is either 0 or 1, since a particular point only can be in either gas ($f=0$) or liquid ($f=1$), i.e., the probability density function of mixture fraction consists of Dirac delta functions at $f=0$ and 1. Taking scalar properties at the jet exit and in the environment to be ϕ_0 and ϕ_∞ , all mean scalar properties can then be found in terms of the Favre-averaged mean mixture fraction, \tilde{f} , as follows:

$$\tilde{\phi} = \phi_\infty(1 - \tilde{f}) + \phi_0\tilde{f} \quad (2.2)$$

$$\bar{\phi} = (\phi_\infty\rho_0(1 - \tilde{f}) + \phi_0\rho_\infty\tilde{f})/(\rho_0(1 - \tilde{f}) + \rho_\infty\tilde{\phi}) . \quad (2.3)$$

Similarly, higher moments of scalars — $\tilde{\phi}''$, $\bar{\phi}'$, etc. — are also only functions of $\tilde{\phi}$ for present conditions; therefore, the governing equation for mixture fraction fluctuations is not needed at this limit.

2.3.3 Computations

The governing equations were solved using GENMIX (Spalding, 1977). The large density variations of the flows caused problems of computational stability and numerical accuracy, requiring much finer grids than are usually needed for single-phase flows. Present slug and fully-developed flow computations used 360 and 720 crosstream grid nodes, with streamwise step sizes limited to 0.30 and 0.15 percent of current flow width, respectively. Doubling the number of grid nodes in both the crosstream and streamwise directions changed predictions less than one percent.

The sensitivity of present calculations was examined similar to past spray analysis (Faeth, 1987). Predictions were most sensitive to uncertainties in the initial values of k and ϵ . However, these parameters were reasonably well known for fully-developed injector flows, while effects of turbulence properties in the core of the flow were not very significant for slug flow. Thus, uncertainties in predictions, aside from well recognized limitations of k - ϵ turbulence models for boundary-layer flows, are generally within experimental uncertainties.

2.4 Results and Discussion

2.4.1 Flow Visualization.

Typical flash photographs for fully-developed flow in the first wind-induced, second wind-induced and atomization breakup regimes are illustrated in Fig. 3. These results were obtained using the 9.5 mm diameter injector. However, findings for the 19.1 mm diameter injector were similar. Four pictures are shown for each test condition: near

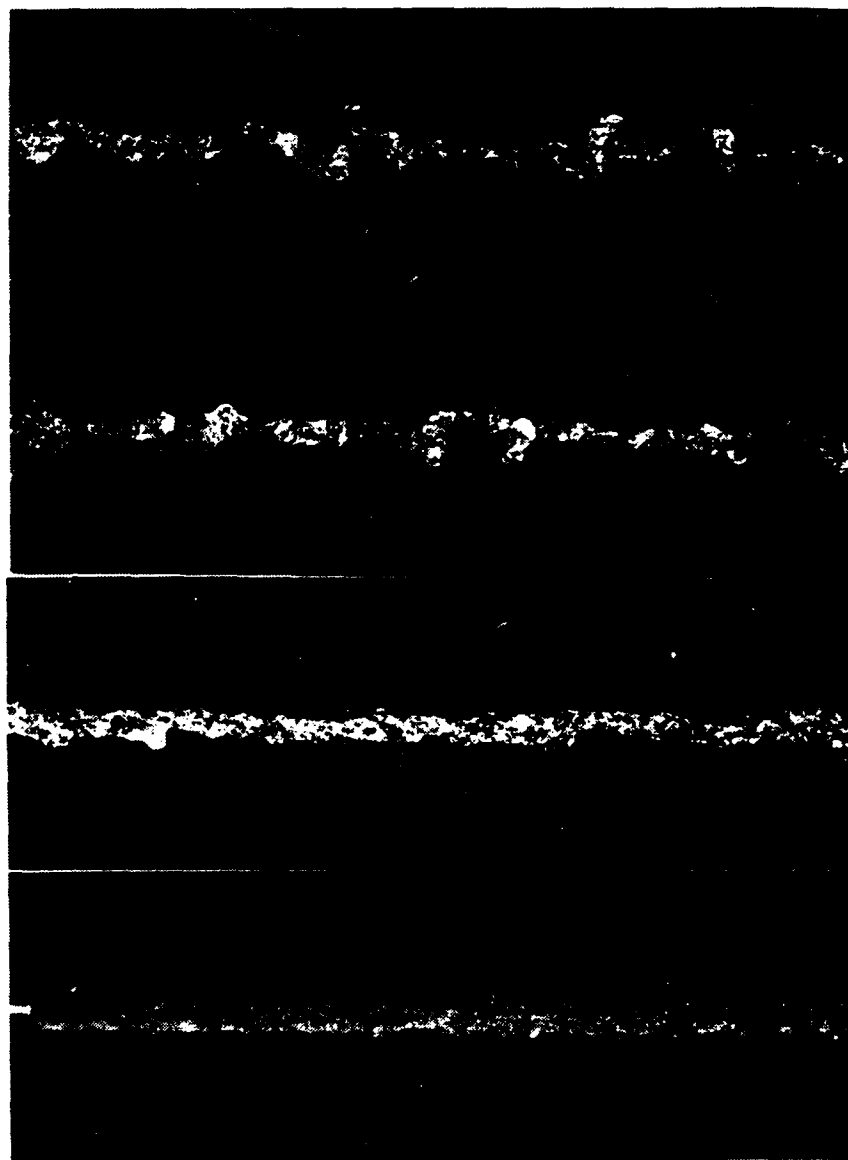


Figure 3a Flash photographs of the 9.5 mm diameter injector for fully-developed flow:
first wind-induced breakup.

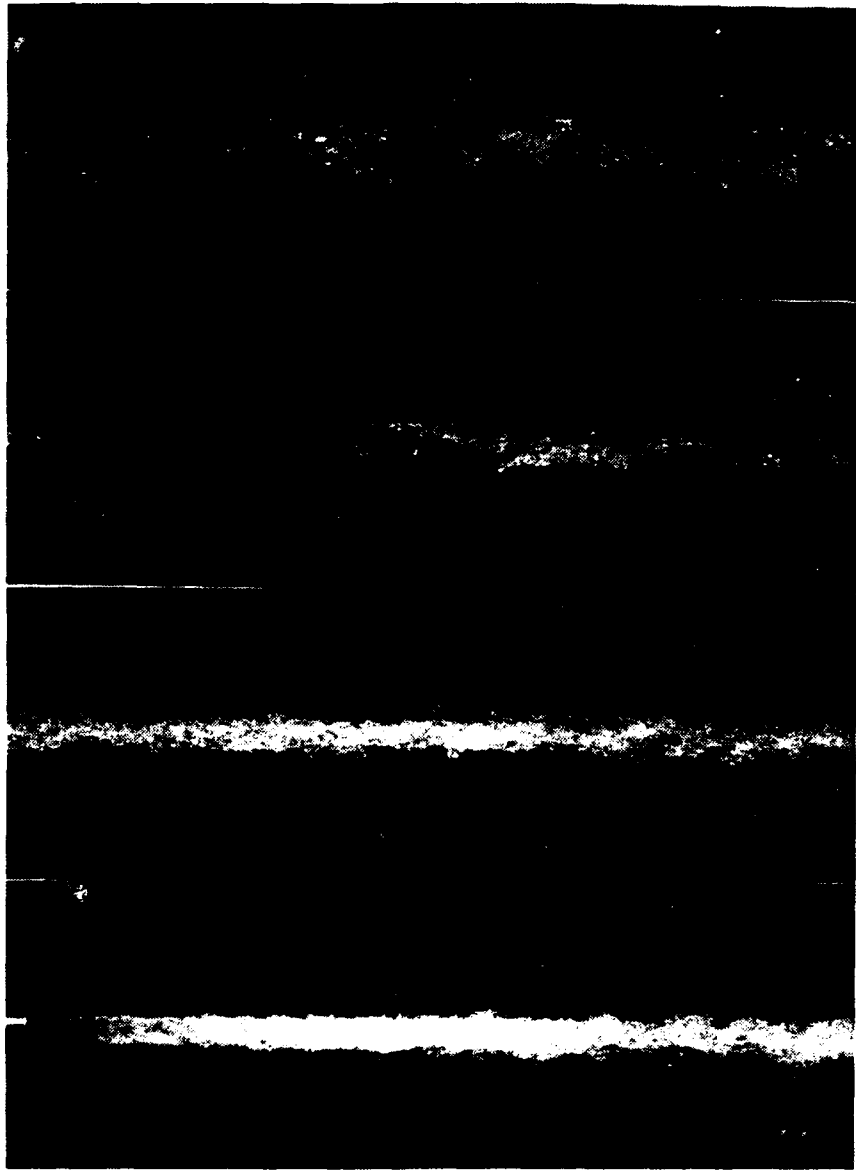


Figure 3h Flash photographs of the 9.5 mm diameter injector for fully-developed flow:
second wind-induced breakup.

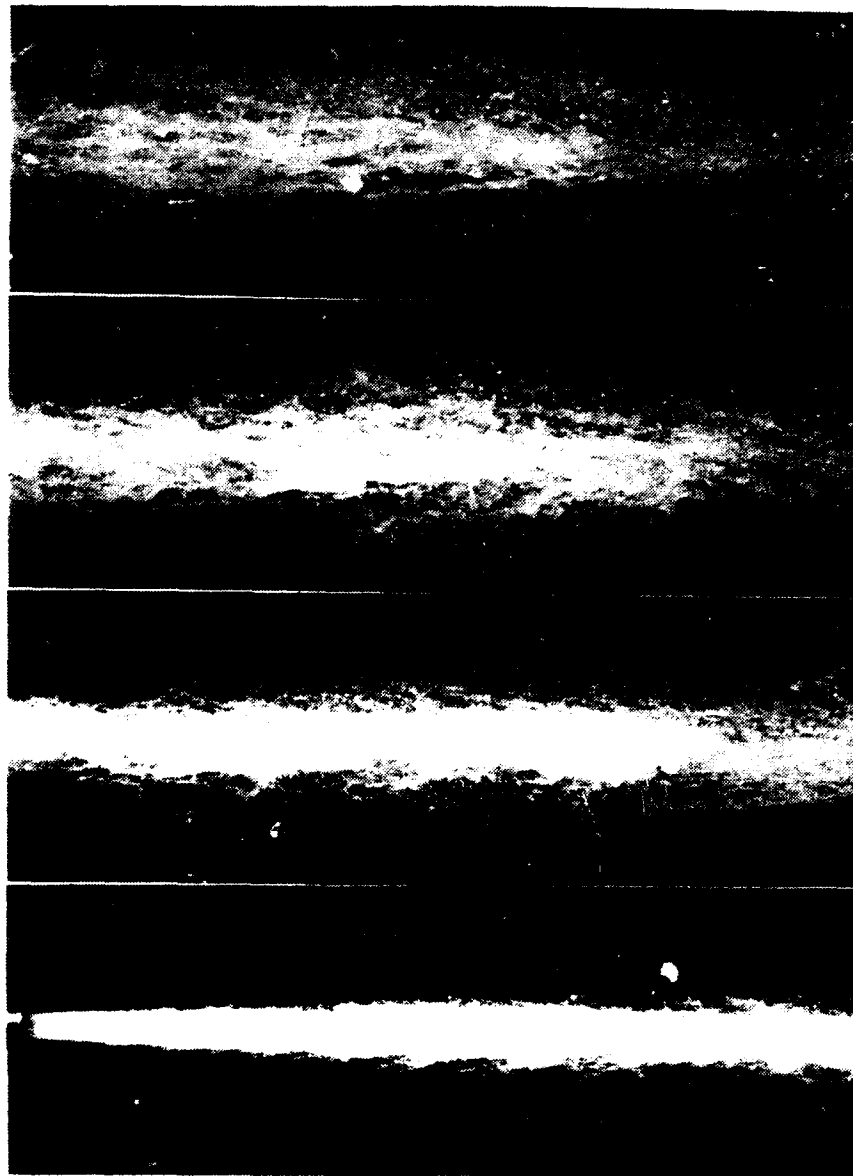


Figure 3c Flash photographs of the 9.5 mm diameter injector for fully-developed flow:
atomization breakup.

the injector exit; and centered at $x/d = 50, 100$ and 150 . The lowest position appearing in the photographs is nearly 2 m from the injector exit.

For first wind-induced breakup, the liquid surface exhibits fine-grained roughness near the injector exit, which becomes smoother, with large-scale irregularities appearing far from the injector. This suggests shifts in the turbulence spectra of both phases. Liquid-phase turbulence properties near the injector exit are governed by the injector passage. Once the flow leaves the passage, however, mean liquid velocities become more uniform since the gas cannot retard the surface velocity as effectively as the wall of the injector passage. This reduces turbulence production in the liquid, causing the turbulence to decay with the small-scale, high wave-number end of the spectrum disappearing first. The developing flow in the gas phase also favors the smallest scales near the injector exit. However, gas-phase turbulence probably does not have a strong influence on liquid surface properties at atmospheric pressure, since the gas density is small in comparison to the liquid. This was confirmed, since the liquid surface exhibited little fine-grained roughness near the injector exit for slug flow, which had low initial turbulence intensities (Ruff et al., 1987). Thus, for present conditions, liquid-phase turbulence properties at the injector exit dominate roughness of the liquid surface and probably influence drop size distributions once breakup occurs as well. For first wind-induced breakup, however, the large-scale irregularities (kinks) of the liquid column eventually cause breakup into the large liquid elements that are characteristic of this breakup regime.

In the second wind-induced breakup regime, the liquid-phase turbulence again produces small-scale surface roughness. However, these disturbances grow and are sheared from the surface, producing a cloud of drops surrounding the liquid core. The point where breakup begins is roughly three injector diameters from the injector exit for the condition illustrated in Fig. 3. The character of the surface roughness influences breakup, e.g., slug flow conditions at the same flow rate, where the liquid surface was relatively smooth, caused the point of breakup to move downstream to $25\text{-}30$ injector diameters from the exit (Ruff et al., 1987). Present criteria for breakup regime transitions do not account for effects of flow development at the injector exit, which clearly affect the onset of atomization. Extending the criteria to account for these effects is certainly needed. In spite of breakup at the surface, however, an all-liquid core can clearly be seen in the flow. This liquid core eventually breaks up far from the injector, probably yielding some rather large drops, similar to first wind-induced breakup.

As noted earlier, increasing injector velocities in the second wind-induced breakup regime causes the point of breakup of the surface of the liquid column to move toward the injector exit. When breakup reaches the exit, the atomization breakup regime is entered and is observed for all higher injector flow rates. The atomization condition illustrated in Fig. 1 is well within the atomization regime. The wispy appearance of the drop-containing region near the edge of the flow, similar to a single-phase flow containing tracer particles, suggests that the drops near the exit are small. Clear areas of drop intermittency, also similar to single-phase turbulent shear layers, penetrate the drop-containing region. The extent of penetration is relatively small near the injector exit, suggesting the presence of an all-liquid core similar to the other breakup regimes illustrated in Fig. 3. The depth of penetration of the drop-free regions increases with increasing distance from the injector, but drop intermittency is not seen at the axis until $x/d \sim 150\text{-}200$.

The spray had a more opaque, milky appearance for slug flow than for fully-developed flow and atomization breakup, due to higher concentrations of smaller drops in the multiphase mixing layer. However, the rate of spread of the mixing layer (indicated by the extent of the region where drops scattered significant light on the photographs) was significantly smaller, and the appearance of drop intermittency along the axis was delayed

for slug flow. This implies a longer all-liquid core for slug flow than for fully-developed flow, for the same injector flow rate. This behavior is confirmed by the liquid volume fraction measurements to be considered next.

2.4.2 All-Liquid Core

Measurements of liquid volume fractions using gamma-ray absorption are largely relevant to the properties of the all-liquid core. Measured and predicted time-averaged mean liquid volume fractions along the axis of the fully-developed and slug-flow sprays are plotted as a function of x/d in Figs. 4 and 5. Fully-developed flows included 9.5 and 19.1 mm diameter injectors and all three breakup regimes. Slug flows were limited to the 9.5 mm diameter injector and the second wind-induced and atomization breakup regimes.

For fully-developed flow (Fig. 4), the near-injector region ($x/d < 10$) exhibits liquid volume fractions near unity. For $x/d > 10$, however, liquid volume fractions decrease rapidly in the second wind-induced and atomization breakup regimes, reaching values of 0.2-0.3 at $x/d = 150$. For $x/d < 40$, the measurements for both injectors in the second wind-induced and atomization regimes are similar, when the streamwise distance is normalized by the injector diameter. This behavior suggests a turbulent mixing-controlled process in the near-injector region, which might be amenable to analysis using the LHF approximation.

In contrast, mixing is much slower for the first wind-induced breakup regime than the other breakup regimes illustrated in Fig. 4 for fully-developed flow. In this case, liquid volume fractions remain near unity for $x/d < 50$, followed by a region of rapid reduction of mean liquid volume fractions along the axis. In the region where the mean liquid volume fraction declines, however, apparent mixing is only due to lateral deflection of the liquid column (the formation of kinks and lateral flapping of the column as a whole), rather than the more complete mixing caused by the formation of drops, see Fig. 3. However, flow properties for first wind-induced breakup are seen to also scale with injector diameter.

The results illustrated in Fig. 4 for fully-developed flows superficially suggest a relatively short all-liquid core near the injector exit, particularly for second wind-induced and atomization breakup. This is not actually the case. Due to the large water/air density ratio of the flow, liquid volume fraction is a very sensitive function of mixture fraction. This can be seen from the following table, giving α_f as a function of f , under the LHF approximation for the present density ratio (846.1).

f	1.0000	0.9999	0.9990	0.9900	0.9000
α_f	1.000	0.922	0.541	0.105	0.011

It can be seen that the mixture fraction decreases only 1 percent, while the liquid volume fraction decreases by a factor of ten, from 1 to 0.1. Thus, all the results illustrated in Fig. 4 represent mixture fractions greater than 0.99. (Note that with liquid velocities greater than gas velocities, the reduction of f would be even smaller if the LHF approximation was not valid.) Thus, as expected, mixing is much slower for the present liquid jets than for single-phase flows, where $f_c \sim 0.03$ at $x/d = 150$ (Shearer et al., 1979). Long liquid cores are present for all flows considered here, when viewed in terms of mixture fraction.

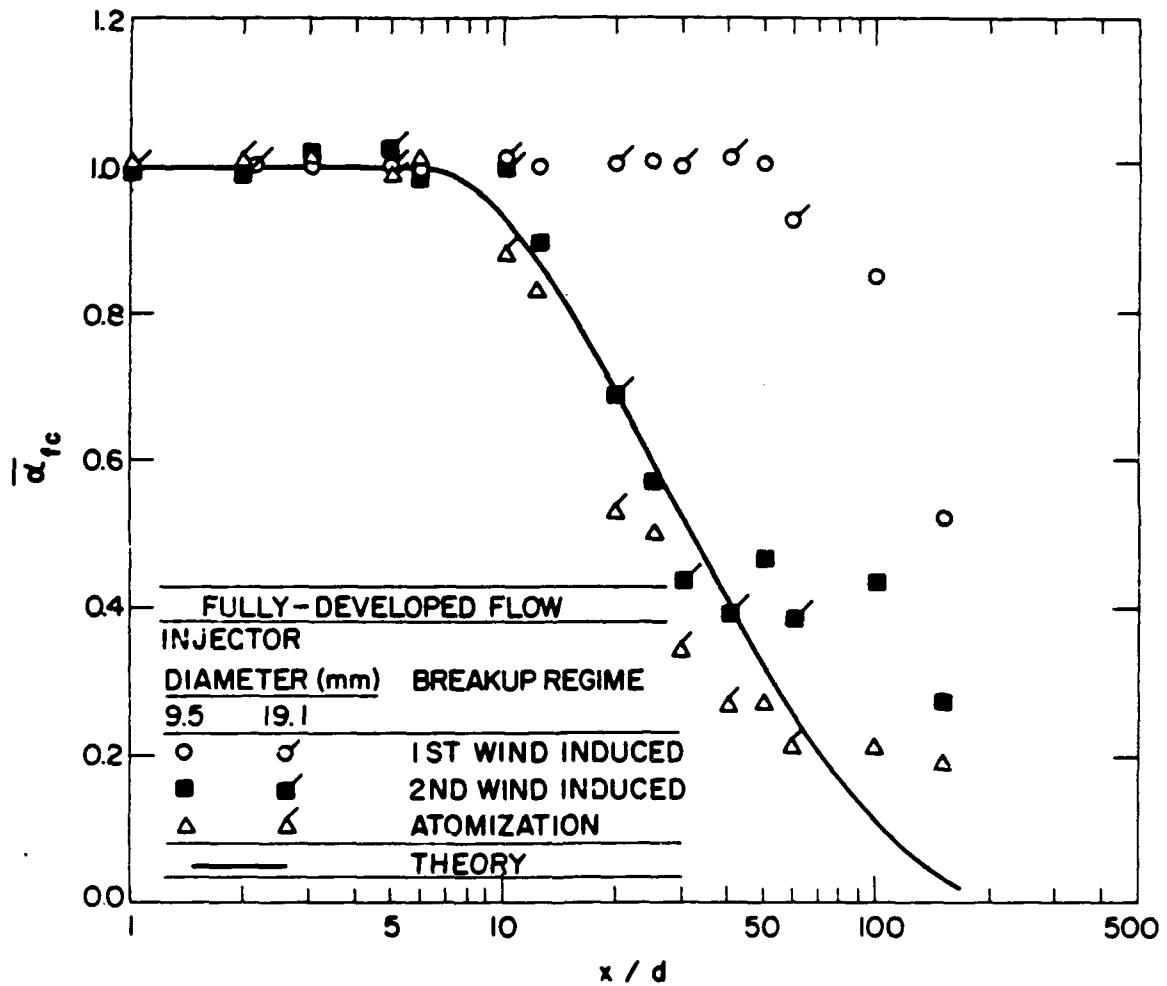


Figure 4 Time-averaged liquid volume fractions along axis for fully-developed flow.

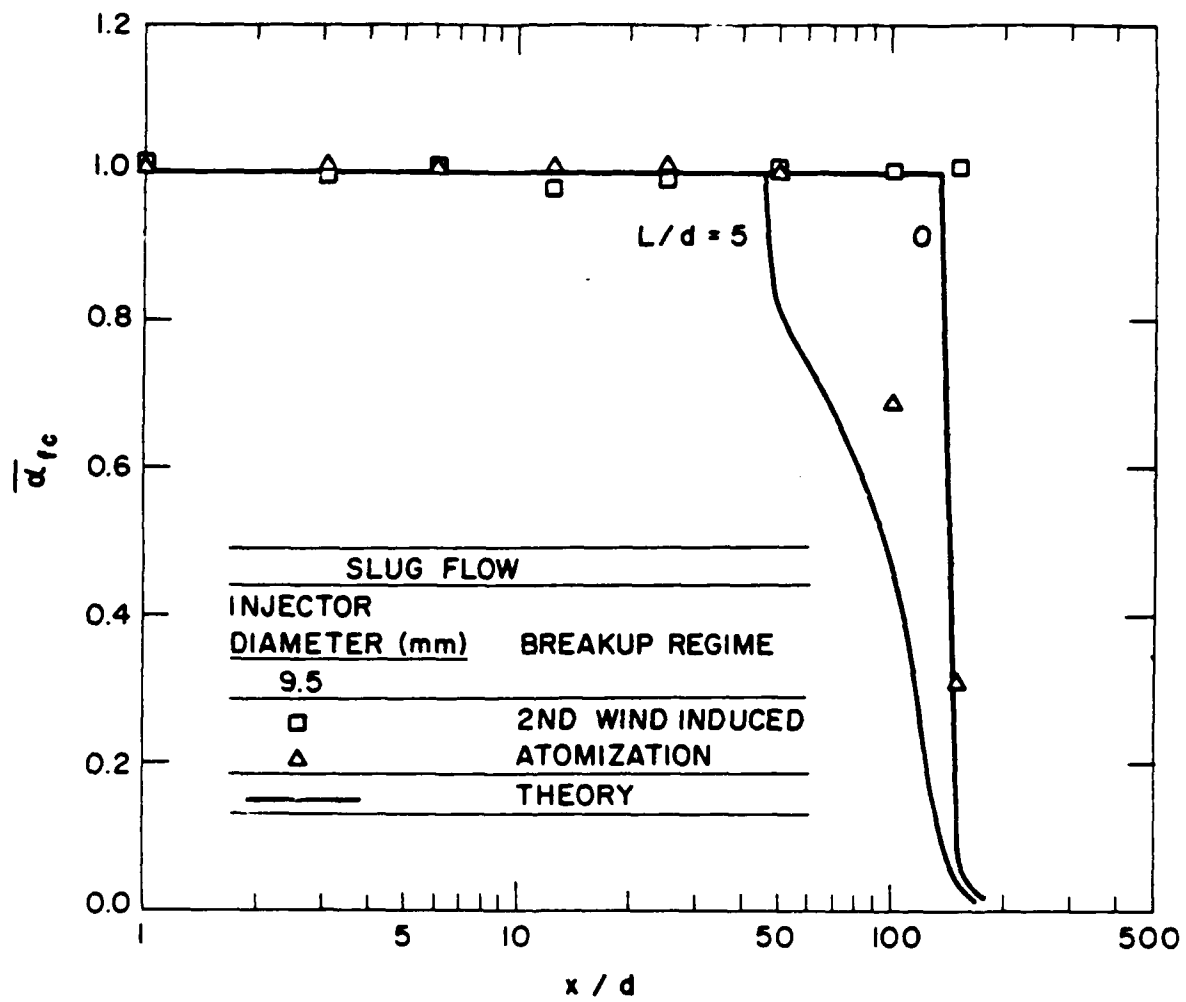


Figure 5 Time-averaged liquid volume fractions along axis for slug flow.

LHF predictions are essentially independent of Reynolds number at the present high Reynolds numbers. Therefore, the single prediction appearing in Fig. 4 represents all test conditions for fully-developed flow. Measurements for second wind-induced breakup are in good agreement with this prediction when $x/d < 40$, while similar agreement is observed for atomization breakup for $x/d < 100$. At greater distances, measured liquid volume fractions are greater than predictions, suggesting increased effects of relative velocities between the phases. It is plausible that results for second wind-induced breakup depart from predictions sooner than atomization breakup, since drop sizes are larger for second wind-induced breakup, providing greater potential for significant relative velocities between the phases. Failure of the LHF approximation also occurs slightly sooner (in terms of x/d) for the smaller injector, since smaller passage diameters yield higher flow deceleration rates (which scales as u_0/d), which cause higher relative velocities in the flow (Faeth 1983, 1987). Such higher relative velocities become significant in comparison to local flow velocities nearer to the injector for the smaller injector, reducing the region where the LHF approximation is adequate. These effects eventually become important for all the flows considered in Fig. 4, causing LHF predictions to fail far from the injector, as the dilute spray region is approached. This observation is consistent with deficiencies reported in the past for LHF analysis of dilute sprays (Faeth 1983, 1987).

Comparing results for atomization breakup for fully-developed and slug flow at the injector exit (cf. Figs. 4 and 5) shows that effects of flow development at the injector exit are nearly as dramatic as effects of the breakup regime. The physical reason for this behavior is that the liquid density is large in comparison to the gas. Therefore, fully-developed flow carries significant levels of turbulence energy into the flow, enhancing mixing in the region where mixture fractions are high. As noted earlier, this liquid-phase turbulence also creates instabilities in the liquid surface which would provide more rapid breakup of liquid into drops — enhancing mixing as well.

These effects cause slower initial rates of flow development for slug flow than for fully-developed flow, e.g., liquid volume fractions for slug flow remain near unity for $x/d < 50$, as opposed to $x/d < 10$ for fully-developed flow. However, later development of the flow is rapid, resulting in mean liquid volume fractions near 0.3 at $x/d = 150$. This implies a relatively long all-liquid core, particularly when viewed in terms of mixture fraction — as noted earlier.

Predictions illustrated in Fig. 5 are relatively independent of Reynolds number but are strongly influenced by the degree of flow development at the injector exit (which is represented by the passage L/d). It is encouraging that computations for $L/d = 0$ and 5, which are reasonable limits for the test injector, tend to bound the measurements for atomization breakup. Comparing results for atomization breakup in Figs. 4 and 5 shows that LHF predictions properly represent the strong effect of the degree of flow development at the injector exit on the subsequent mixing of the spray in the near-injector region. The effect of flow development is probably a contributing factor in controversies concerning the properties of the all-liquid core based on measurements from short L/d injectors (Chehroudi et al., 1985; Hiroyasu et al., 1982; Phinney, 1973).

Radial profiles of time-averaged liquid volume fractions for atomization breakup are illustrated in Figs. 6-8. Measurements and predictions are plotted as a function of radial distance, normalized by the injector diameter, at various distances from the injector exit. Results for fully-developed flow for the 19.1 and 9.5 mm diameter injectors are plotted in Figs. 6 and 7. Similar results for slug flow appear in Fig. 8.

The apparent flow widths seen in Figs. 6-8 are unusually narrow in comparison to single-phase jets. For example, flow widths are on the order of $2r/d = 4-6$ for $x/d = 100$.

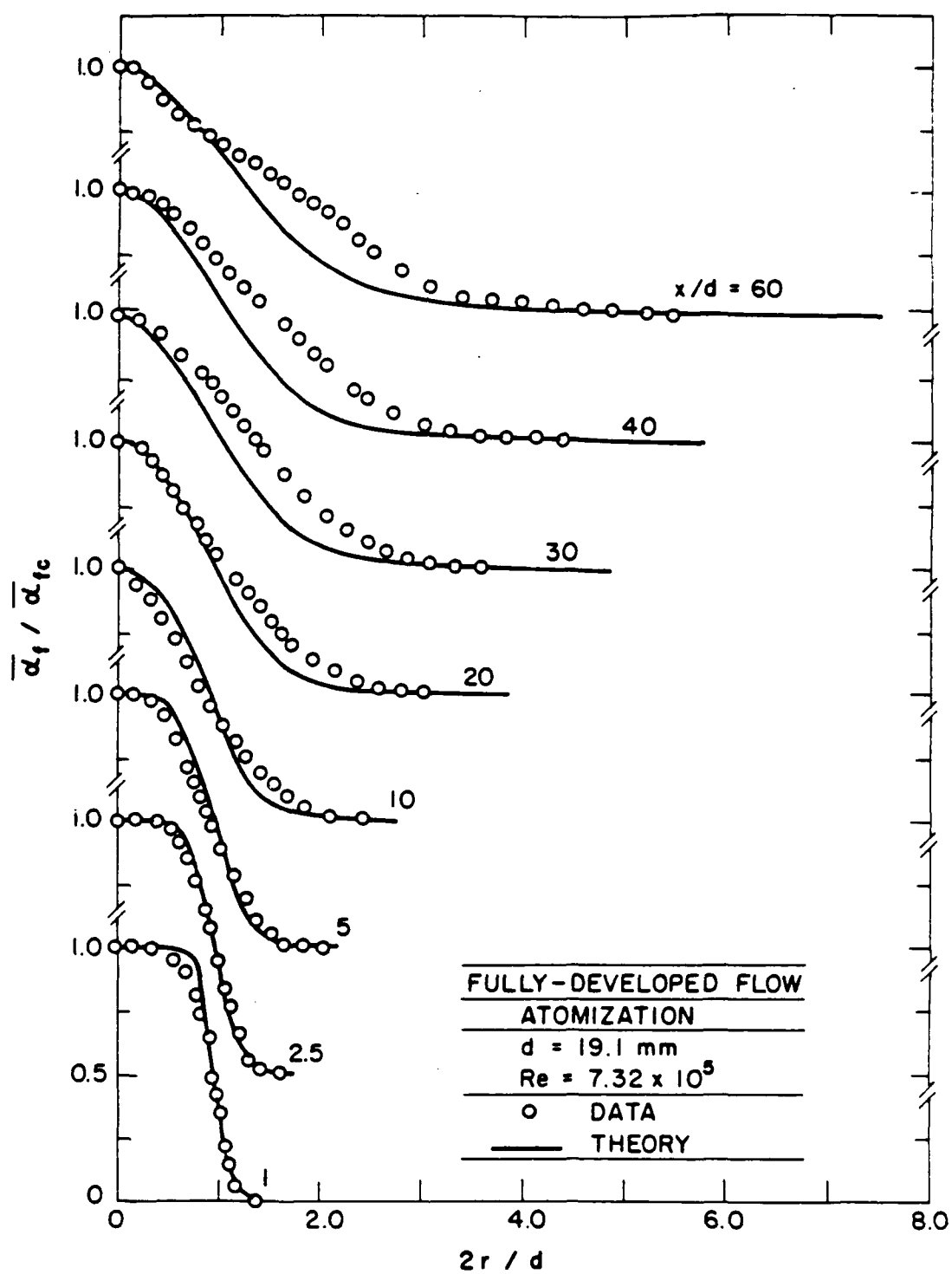


Figure 6 Radial profiles of time-averaged liquid volume fractions for fully-developed flow and atomization breakup (19.1 mm diameter injector).

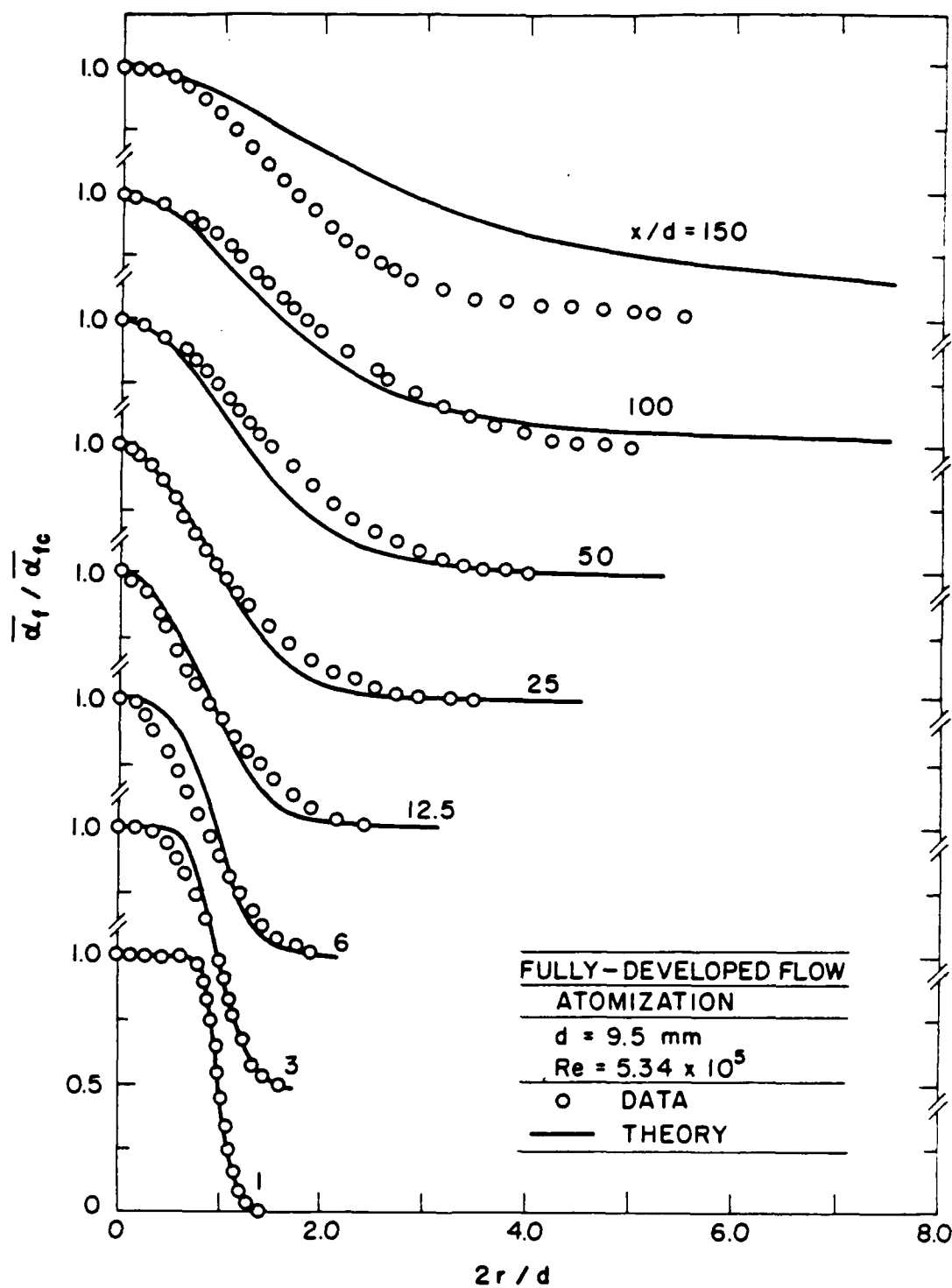


Figure 7 Radial profiles of time-averaged liquid volume fractions for fully-developed flow and atomization breakup (9.5 mm diameter injector).

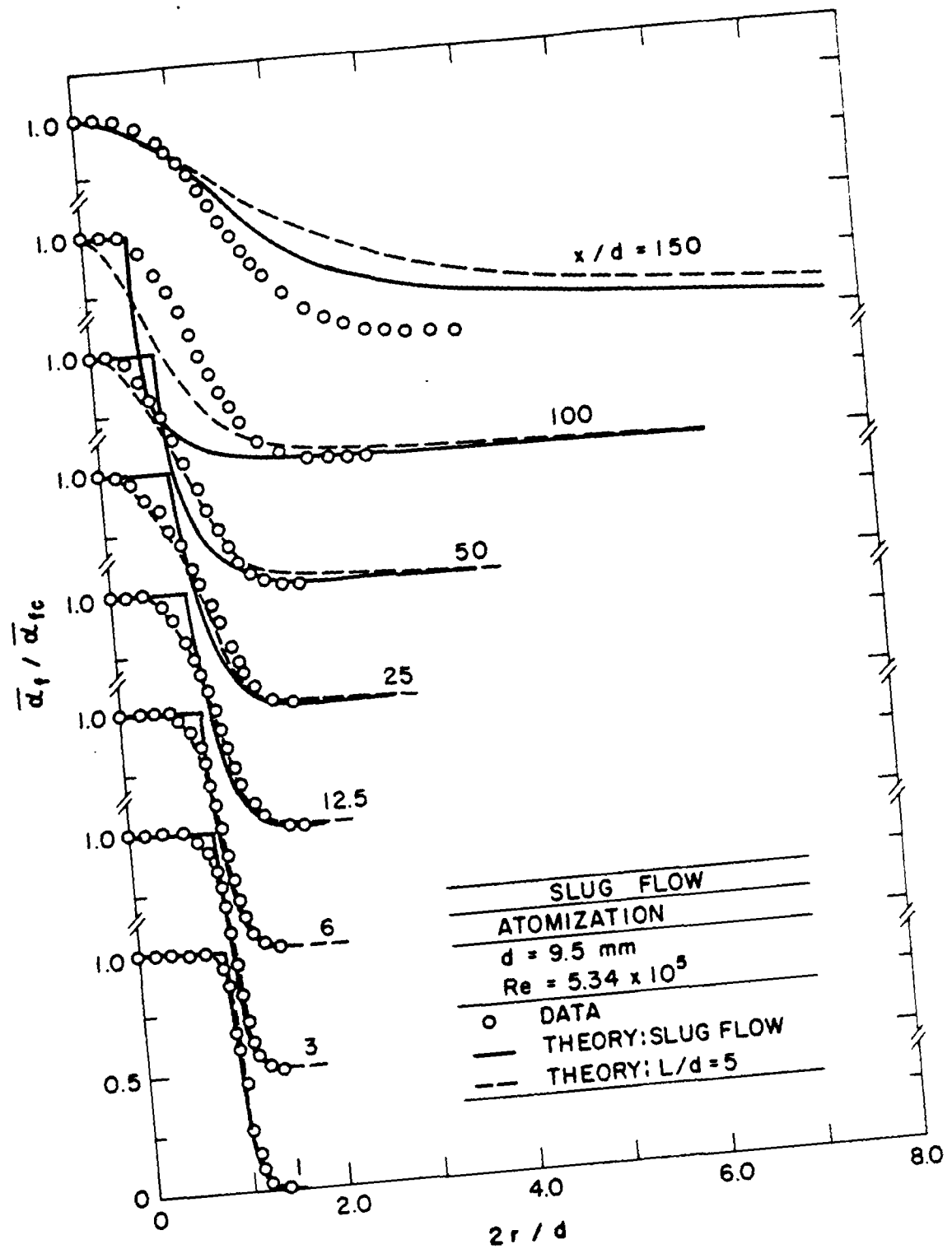


Figure 8 Radial profiles of time-averaged liquid volume fractions for slug flow and atomization breakup (9.5 mm diameter injector).

150, which corresponds to r/x on the order of 0.02. In comparison, widths of single-phase jets are nearly an order-of-magnitude larger, ca. $r/x = 0.15$ (Wyganski & Fiedler, 1969). The sensitivity of liquid volume fraction to mixture fraction, mentioned earlier, is the main cause of this behavior, e.g., profiles of mixture fraction are much wider than liquid volume fraction. The all-liquid core for present flows also contributes to this behavior, since liquid that has not become atomized cannot mix very effectively.

For fully-developed flow, the comparison between predicted and measured radial profiles of mean liquid volume fractions seen in Figs. 6 and 7 can be anticipated from the results along the axis illustrated in Fig. 4. Conditions where $\bar{\alpha}_{fc}$ is predicted well, e.g. $x/d < 100$, also results in reasonably good predictions of radial profiles. All predictions far from the injector, however, overestimate the width of the flow. This agrees with past evaluations of LHF analysis in the dilute portions of sprays, which showed that the method invariably overestimates measured rates of flow development (see Faeth (1987)). This occurs since relative velocities become significant whenever flow velocities are low, which roughly corresponds to the dilute-spray region for present test conditions.

Results for slug flow are illustrated in Fig. 8. In this case predictions are plotted for the limits of $L/d = 0$ and 5. Near the injector, there is a reasonably wide zone where liquid volume fractions are nearly unity. Predictions suggest a sharp transition between this region and the shear layer, while measurements show a more gradual transition between these regions. This discrepancy is partly due to gradient-broadening errors of the measurements, where the finite diameter of the paths of the absorption measurements cannot resolve rapid radial variations of mean liquid volume fractions. On the other hand, the discontinuity of the predictions is due to approximations made to match calculations in the mixing layer with the all-liquid core and is probably not observed in nature.

The discrepancies between predictions and measurements are largest at $x/d = 100$ for slug flow. Both predictions underestimate the flow width, rather than overestimating it, which is the expected behavior of the LHF approximation. This behavior is caused by the discrepancies between measured $\bar{\alpha}_{fc}$ and predictions for the limits of $L/d = 0$ and 5 near $x/d = 100$ (see Fig. 5). Thus, the poor agreement at $x/d = 100$ is due largely to the $\bar{\alpha}_f/\bar{\alpha}_{fc}$ normalization used in Fig. 8.

For slug flow and $x/d = 150$, corresponding to low values of $\bar{\alpha}_{fc}$, the predictions for $L/d = 0$ and 5 overestimate the development of the jet, similar to fully-developed flow. However, the slug flow predictions do not depart as much from the measurements as for the fully-developed flow at this position (see Fig. 7). Two reasons can be given for this behavior. First, slug flow develops more slowly than fully-developed flow, providing a more extended mixing layer region with lower rates of deceleration — tending to favor the LHF approximation. Secondly, as noted earlier, smaller drops are generated for slug flow than for fully-developed flow, which also favors the LHF approximation. Based on the Taylor (1940) breakup criterion, discussed by Reitz & Bracco (1982), the production of smaller drops for slug flow than fully-developed flow is expected because of the higher velocity gradients near the liquid surface. Direct measurements of drop size and velocity properties in the near-injector region, to be discussed next, confirms this expectation as well.

2.4.3 Multiphase Mixing Layer

Except for entrainment,2 measurements within the multiphase mixing layer were limited to atomization breakup with the 9.5 mm diameter injector for both fully-developed

and slug flow at the injector exit. Photographs of typical hologram reconstructions, taken from the video monitor of the image analysis system, are illustrated in Figs. 9-11. These results were obtained within the multiphase mixing layer at $x/d = 12.5$ for fully-developed flow. However, results at other axial stations and for slug flow are similar. Three radial positions are considered, corresponding to points near the outer edge (Fig. 9), middle (Fig. 10), and inner edge (Fig. 11) of the multiphase mixing layer. All three photographs are from single-pulse holograms and were obtained with the same magnification, yielding a field of view of $1725 \times 2250 \mu\text{m}$. Except near the liquid surface, usually only a few drops or liquid elements (or portions of them) are in focus for any one screen image of the video monitor. Thus, the photographs have a mottled appearance due to out-of-focus drops. Furthermore, the images on the monitor are much larger and easier to interpret than Figs. 9-11 — particularly since the focal plane can be moved to sharpen the focus on any one object.

Conditions near the outer edge of the multiphase mixing layer, Fig. 9, correspond to a dilute spray: the liquid elements consist of relatively small spherical drops separated by rather large distances. Therefore, the liquid volume fraction is quite small. Moving to the middle of the multiphase mixing layer, Fig. 10, the flow largely remains a dilute spray, although drop diameters and drop number densities are larger than near the edge of the flow. In this region, however, some of the larger liquid elements are no longer spherical, although the ellipticities of individual liquid elements are rarely greater than 2. Finally, as the edge of the all-liquid core is approached, Fig. 11, the liquid elements become quite large and are generally very irregular in shape, consisting of ligaments and long ellipsoids surrounded by only a few spherical drops. The lower right-hand corner of Fig. 11 actually corresponds to a section of the surface of the all-liquid core. This surface is quite irregular and involves long liquid elements protruding into the mixing layer, suggesting initial growth of ligaments before they break away from the surface. A surprising feature of the region near the liquid core, however, is that the gas-containing region is relatively dilute at each instant. Even high-magnification reconstructions of this region did not reveal large numbers of small drops. Thus the main difference between the dilute- and dense-spray regions of the multiphase mixing layer is that the dense-spray region contains large and irregular liquid elements, including protuberances from the all-liquid core. These large liquid objects, as well as lateral fluctuations of the all-liquid core itself, cause time-averaged liquid volume fractions to be large even though the gas-containing region surrounding the liquid elements is relatively dilute at each instant.

Measurements of liquid element sizes and velocities within the multiphase mixing layer for fully-developed flow at $x/d = 12.5, 25, 50$ and 100 are illustrated in Figs. 12-15. The volume-averaged ellipticity, the SMD and drop velocities for $d_p = 10, 30, 100$ and $300 \mu\text{m}$, are plotted as a function of r/x , which is the radial similarity variable for turbulent single-phase jets and plumes. This radial similarity variable has only been chosen for convenience: the region considered is analogous to the mixing-layer around the potential core of a single-phase jet due to the presence of the all-liquid core, and radial profiles for flow properties do not exhibit similarity in the r/x coordinate system. The range of positions where the edge of the all-liquid core was observed is also marked on the plots: the measurements extend from the liquid core to near the outer edge of the multiphase flow region, r/x of 0.150-0.175.

In Figs. 12-15, large values of volume-averaged ellipticity, which are associated with the presence of large and irregular liquid elements, are generally found in the region of the all-liquid core. This region extends across most of the multiphase mixing layer near the jet exit but becomes progressively confined to the region near the axis with increasing distance from the jet exit. Thus, the near-injector region of the spray can be divided into three regions: an all-liquid core, a dense-spray region characterized by nonunity ellipticities,

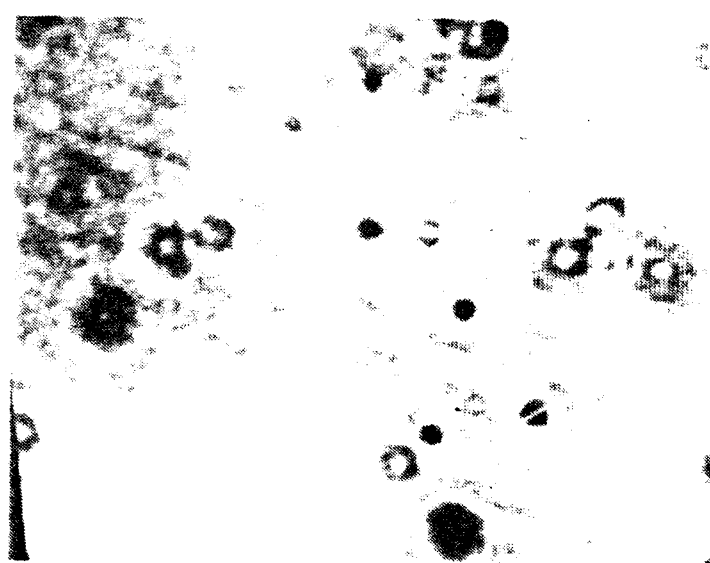


Figure 9 Hologram reconstruction near the outer edge of the multiphase mixing layer: fully-developed flow,
 $x/d = 12.5$, $r/x = 0.150$.

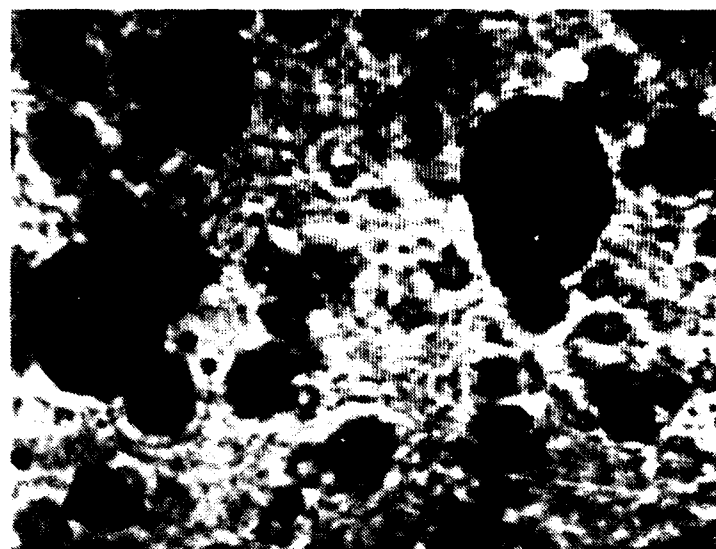


Figure 10 Hologram reconstruction near the middle of the multiphase mixing layer: fully-developed flow, $x/d = 12.5$, $r/x = 0.100$.



Figure 11 Hologram reconstruction near the inner edge of the multiphase mixing layer: fully-developed flow, $x/d = 1.25$, $r/x = 0.050$.

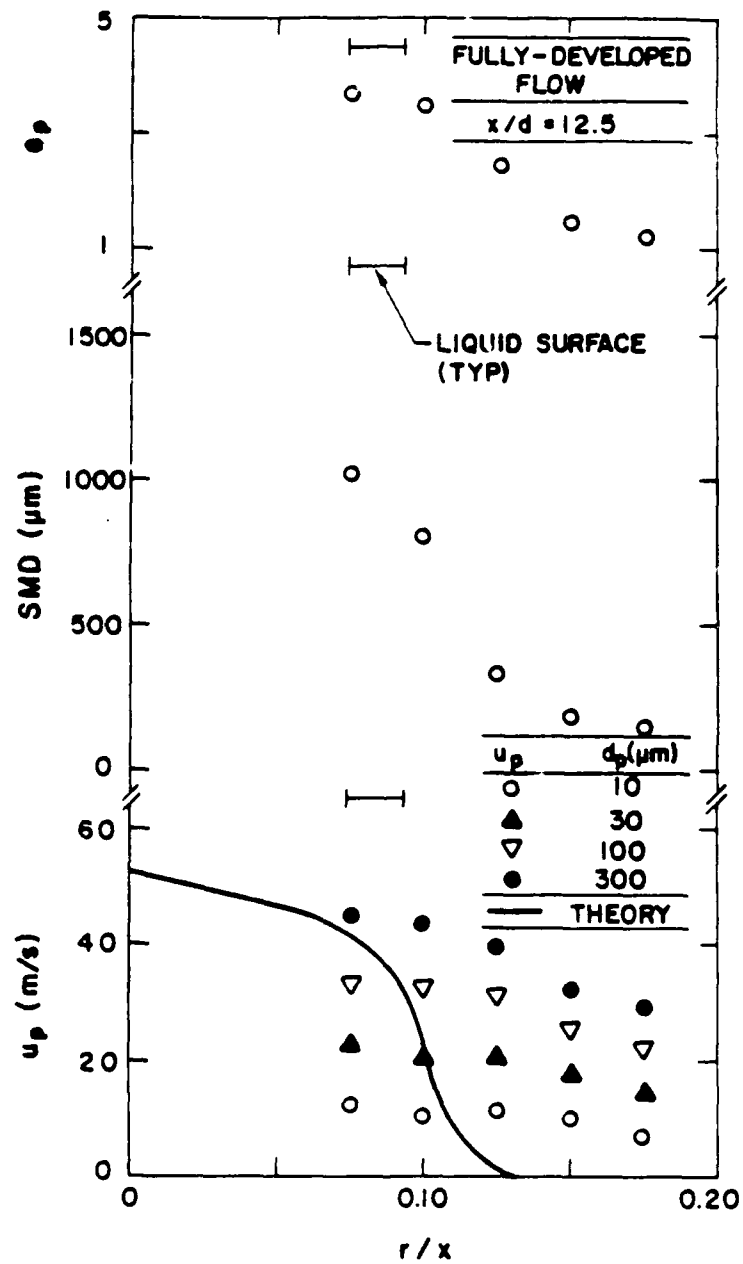


Figure 12 Dispersed-phase properties for fully-developed flow and atomization breakup at $x/d = 12.5$.

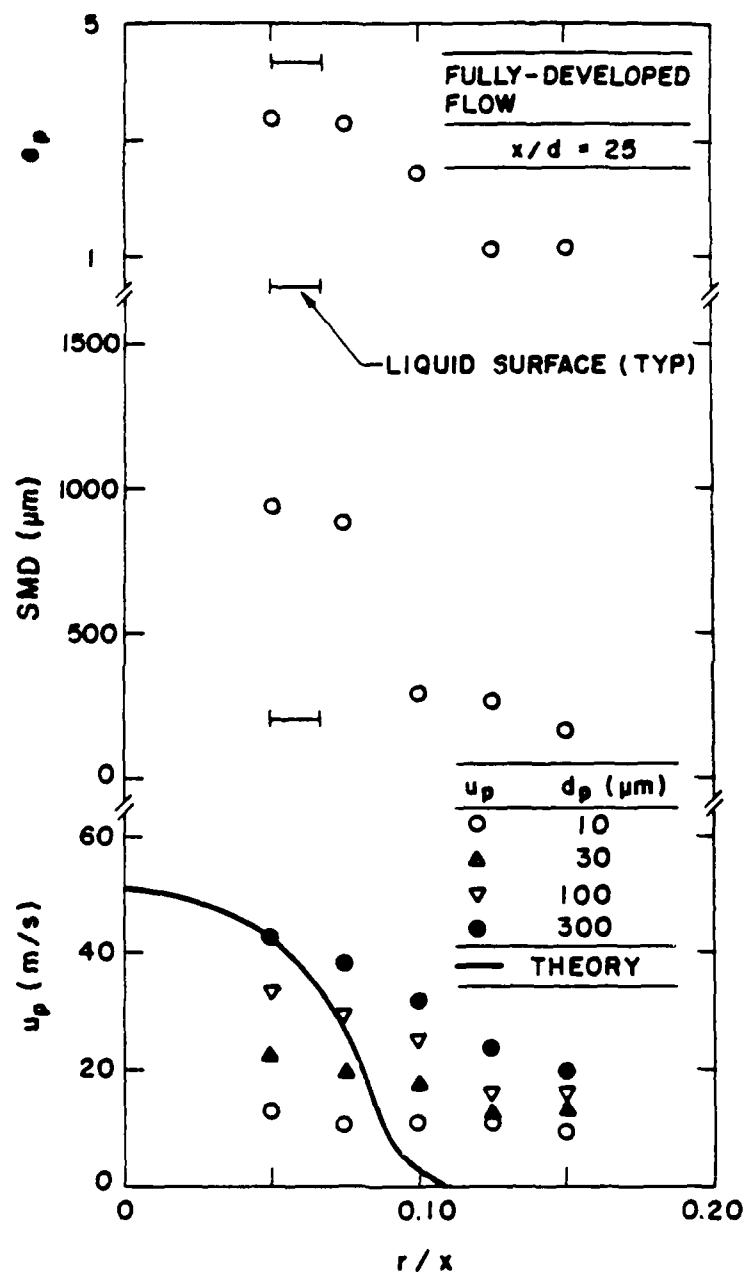


Figure 13 Dispersed-phase properties for fully-developed flow and atomization breakup at $x/d = 25$.

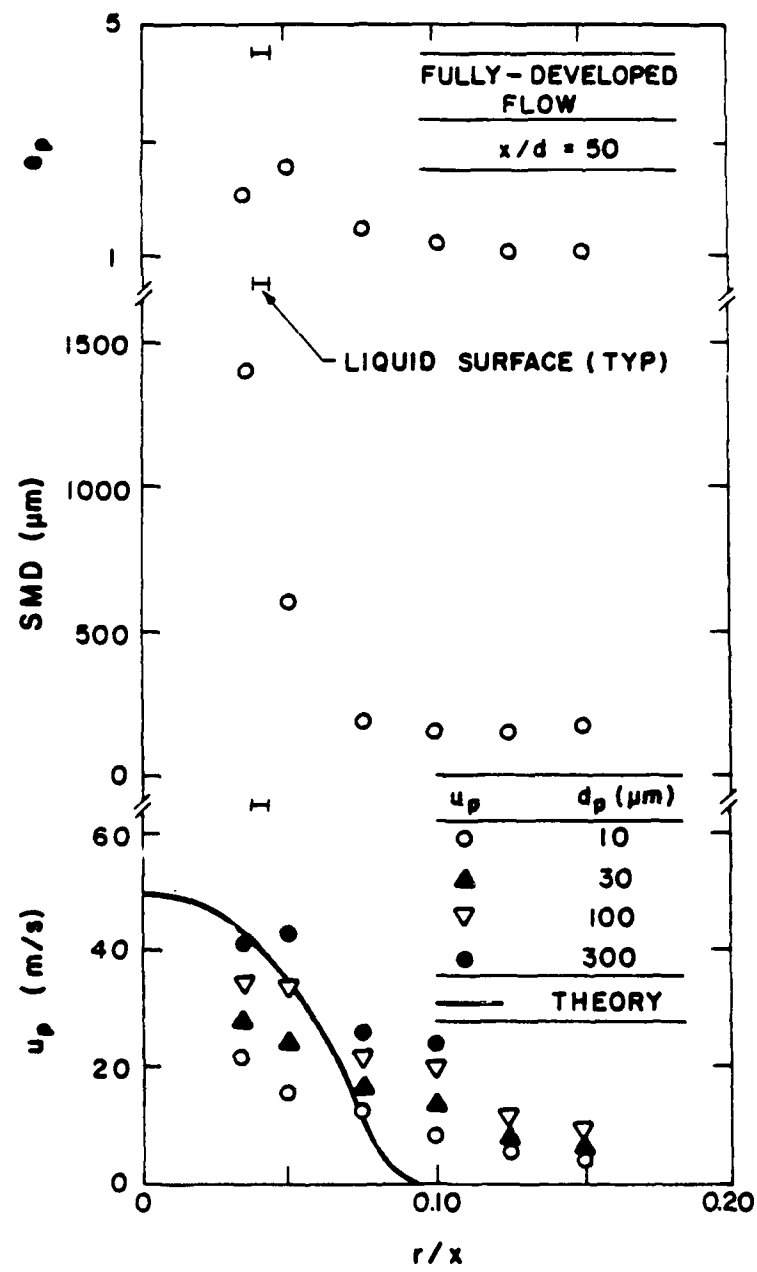


Figure 14 Dispersed-phase properties for fully-developed flow and atomization breakup at $x/d = 50$.

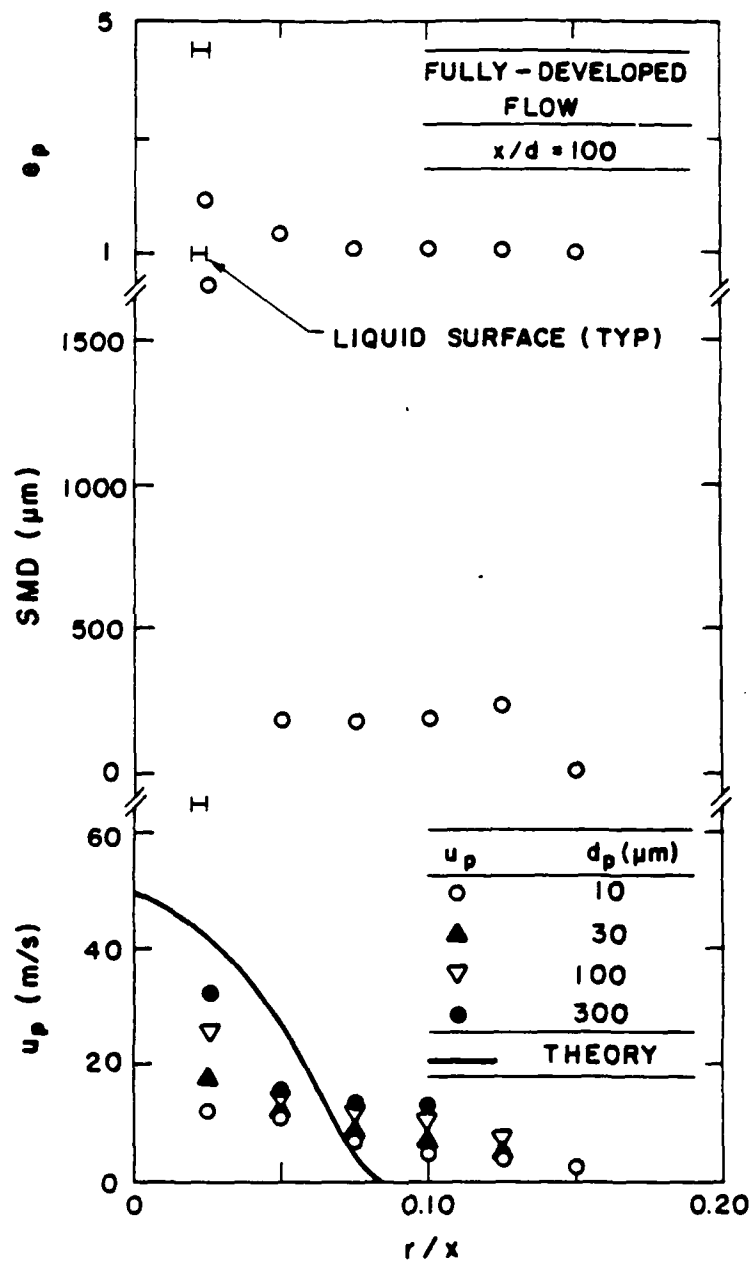


Figure 15 Dispersed-phase properties for fully-developed flow and atomization breakup at $x/d = 100$.

and an outer dilute-spray region where ellipticities are near unity. The outer region progressively grows with increasing distance from the injector, eventually reaching the axis somewhat downstream of the region where liquid stripping by the formation of ligaments and other large liquid elements has caused the all-liquid core to disappear.

Sauter mean diameters, illustrated in Figs. 12-15, progressively decrease with increasing radial distance, similar to the ellipticity. Values of the SMD near the all-liquid core are quite large, 600-1000 μm , due to the presence of large irregular liquid elements. Near the edge of the flow in the dilute-spray region, however, drop sizes are much smaller, generally in the range 100-200 μm , but dropping to even smaller values at the extreme outer edge of the multiphase mixing layer (see Fig. 15). Several phenomena are probably responsible for the progressive reduction of SMD with increasing radial distance, as follows: the tendency of large liquid elements to shatter as they encounter low velocity gas near the edge of the flow; the fact that breakup of ligaments and other large liquid elements requires a finite time allowing them to traverse the inner portions of the mixing layer; and increased turbulent dispersion of small drops which enhances their migration toward the edge of the flow.

Distributions of drop velocities in Figs. 12-15 include both measurements for various drop diameters and predictions based on the LHF approximation. In the region near the all-liquid core, the largest drops have velocities that are comparable to liquid injection velocities, ca. 56 m/s. This follows since velocities within the all-liquid core remain relatively close to jet exit velocities while the large drops have formed only recently and have not had sufficient time for drag from the gas phase to slow their motion. The velocities of drops of all sizes, however, tend to decrease with increasing radial distance. This is expected since gas velocities are lowest near the edge of the flow and drops in this region have had more time to accommodate to gas velocities. A surprising feature of the results of Figs. 12-15, however, is that small drops (which should have velocities relatively close to local gas velocities) have relatively low velocities that are nearly constant across much of the mixing layer — particularly at $x/d = 12.5$ and 25 (Figs. 12 and 13). This suggests that momentum exchange between the liquid and gas is not very efficient in the multiphase mixing layer, perhaps due to the presence of large liquid elements (having relatively low surface-to-volume ratios) in the dense spray region near the all-liquid core. This results in relatively large relative velocities between the phases near the all-liquid core which probably helps promote breakup.

The fact that the drop velocities plotted in Figs. 12-15 vary substantially with drop diameter at each point in the flow provides direct evidence that use of the LHF approximation is not appropriate for the present flow. In view of this, it is hardly surprising that the LHF predictions are not in good agreement with the measurements. The nature of the failure is typical of past evaluations of the LHF approximation for dilute sprays; namely, the rate of development of the flow is overestimated since the analysis does not properly account for the inertia of large drops that take significant time to exchange momentum with the gas phase.

Measurements of liquid element sizes and velocities within the multiphase mixing layer for slug flow are illustrated in Figs. 16-19. These figures are plotted in the same manner as Figs. 12-15 for fully-developed flow except that the scales for ellipticity and SMD have been expanded to improve readability. Many features of dispersed-phase properties are the same for slug and fully-developed flow: ellipticities are largest near the liquid surface, where ligaments and other large liquid elements are present, while the edge of the flow involves nearly round drops; drop sizes are largest near the liquid core, dropping to SMD in the range 100-200 μm near the edge of the flow; and drop velocities

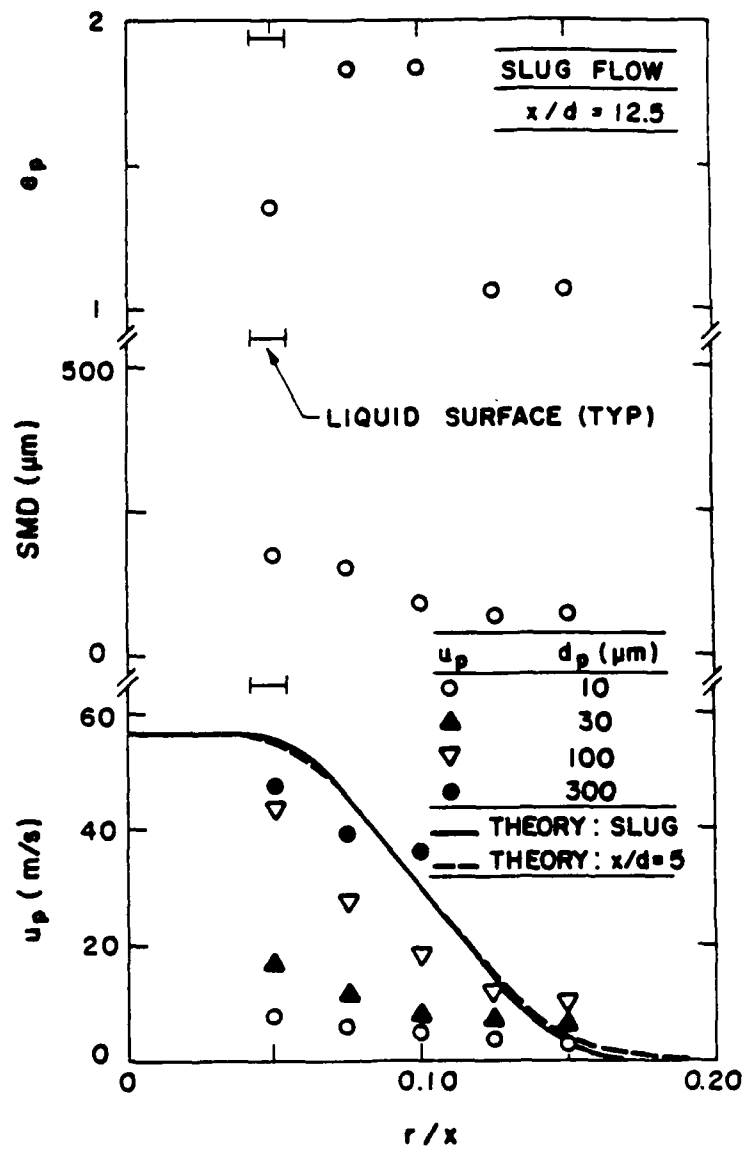


Figure 16 Dispersed-phase properties for slug flow and atomization breakup at $x/d = 12.5$.

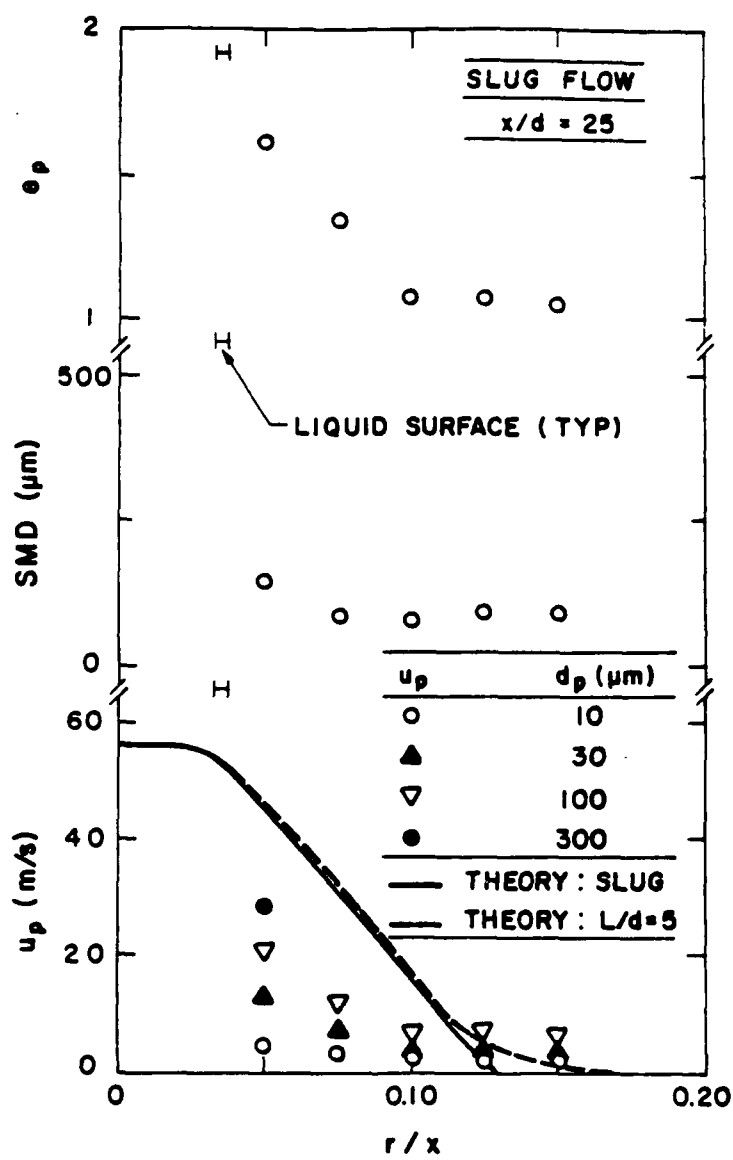


Figure 17 Dispersed-phase properties for slug flow and atomization breakup at $x/d = 25$.

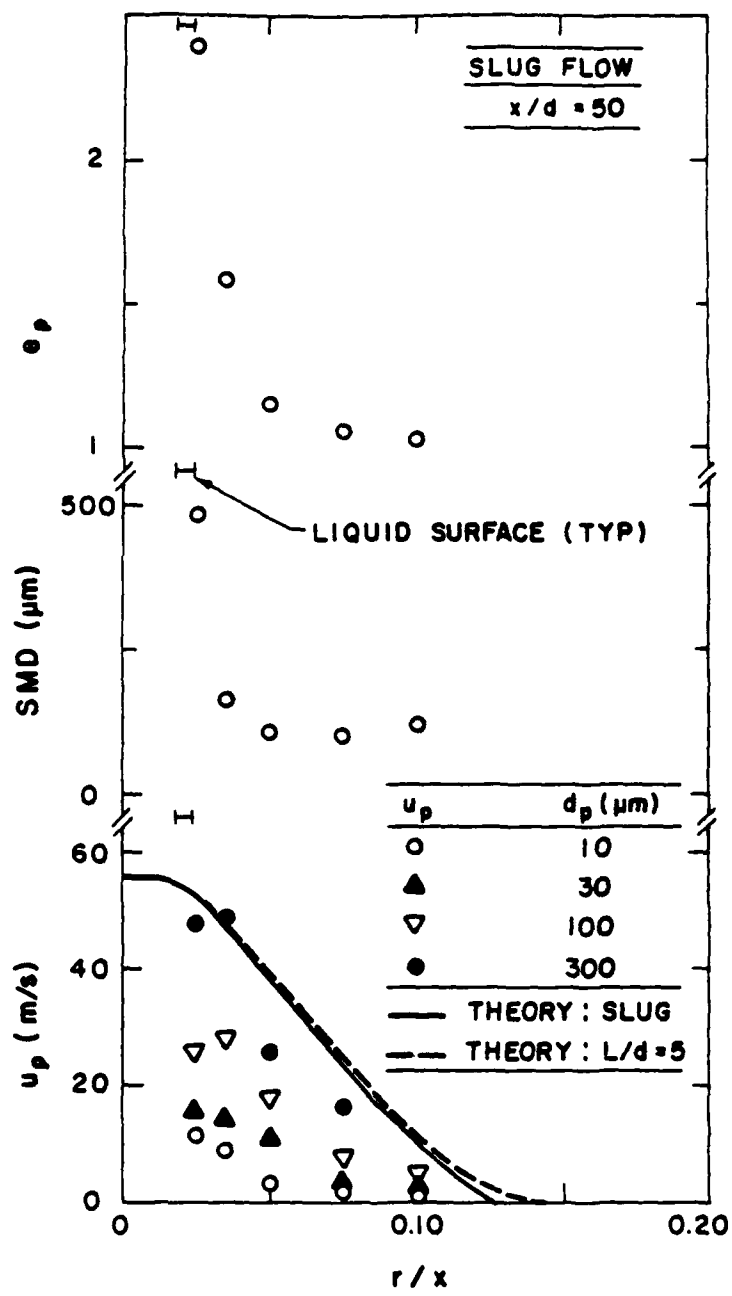


Figure 18 Dispersed-phase properties for slug flow and atomization breakup at $x/d = 50$.

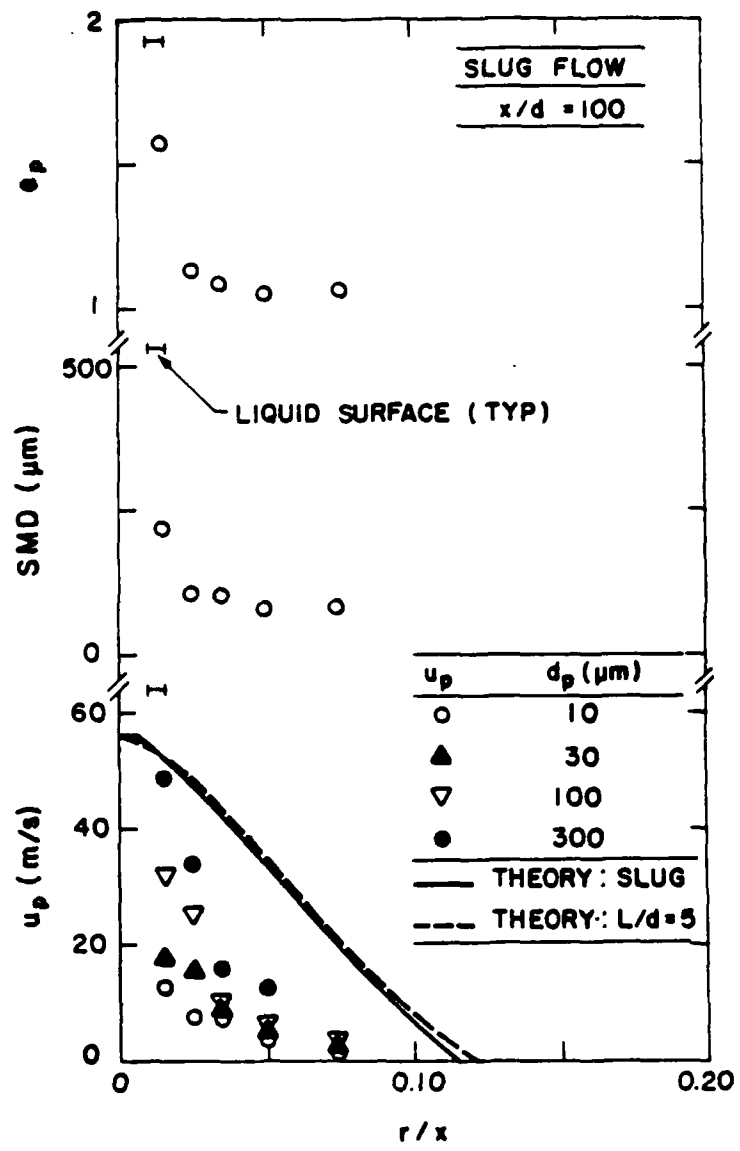


Figure 19 Dispersed-phase properties for slug flow and atomization breakup at $x/d = 100$.

vary substantially with drop size while small drops, and probably the gas as well, have relatively low velocities near the liquid surface.

The main differences between the fully-developed flow results of Figs. 12-15 and the slug flow results of Figs. 16-19 are that the ellipticities and SMD are smaller near the liquid core for slug flow. This suggests that breakup mechanisms at the liquid surface are modified by turbulence levels within the liquid core. Such behavior is quite reasonable based on flash photographs of the liquid surface (for wind-induced breakup where the surface can be readily seen) for fully-developed and slug flow reported by Ruff et al. (1987). In particular, the surface was very wrinkled by the underlying turbulence in the liquid for fully-developed flow while the surface was smoother for slug flow. Clearly, the wrinkling present for fully-developed flow would help promote the expulsion of large liquid elements into the gas phase, enhancing effects of liquid-jet instability that are present for both flows. Liquid-jet instability, working alone, cannot cause breakup to penetrate as far into the liquid phase, yielding the smaller drops observed during the present study, as well as slower rates of mixing of the flow. Even though the drops are initially smaller for slug flow, drop breakup processes in the gas phase are still important, as evidenced by reduced SMD near the edge of the multiphase mixing layer and at the position farthest from the injector.

Another difference between structure of the mixing layer for fully-developed and slug flow is that the layer is significantly wider for fully-developed flow. A mechanism for this behavior is lateral penetration of large liquid elements, which conserve outward radial velocity fluctuations present when they are expelled from the liquid due to their inertia, and then subsequently break up into smaller drops. In contrast, the smaller drops generated for slug flow conditions have lower initial radial velocities so that their lateral spread is limited to effects of turbulent dispersion based only on turbulence present in the gas phase.

Measured and predicted distributions of liquid volume fractions and fluxes for fully-developed and slug flow are illustrated in Fig. 20. Measurements of liquid volume fractions include results found from both holography and gamma-ray absorption. LHF predictions for slug flow are shown for reasonable limits of boundary-layer development along the injector passage, e.g. $L/d = 0$ and 5; however, the differences between the two predictions are not very significant. The position of the liquid surface is also marked on the plots for reference purposes.

In Fig. 20, the liquid volume fraction measurements by holography and gamma-ray absorption are only in fair agreement in the region where they overlap — particularly for fully-developed flow. The problem is that both sets of measurements encounter difficulties in this region: the gamma-ray absorption measurements are near the lower limit of resolution due to limitations of finite sampling times and signal-to-noise ratios; the holography measurements are also problematical due to difficulties of properly evaluating the volume of large and irregular liquid elements from their projected images — a problem that is more pronounced for fully-developed flow where more irregular liquid elements are present. Even after accounting for this difficulty, it is evident that the multiphase mixing layer is quite dilute, quantifying the general impression obtained from the holograms, i.e., excluding the largest liquid elements, maximum liquid volume fractions are roughly 0.01. For liquid volume fractions on this order, effects of collisions are not very significant (Faeth, 1987).

Both the liquid flux and liquid volume fraction results of Fig. 20 highlight the faster rate of radial mixing for fully-developed flow in comparison to slug flow. The main reason for this is the faster rate of breakup at the liquid surface for fully-developed flow, promoted by disturbances due to turbulence in the all-liquid core. The ability of large liquid elements

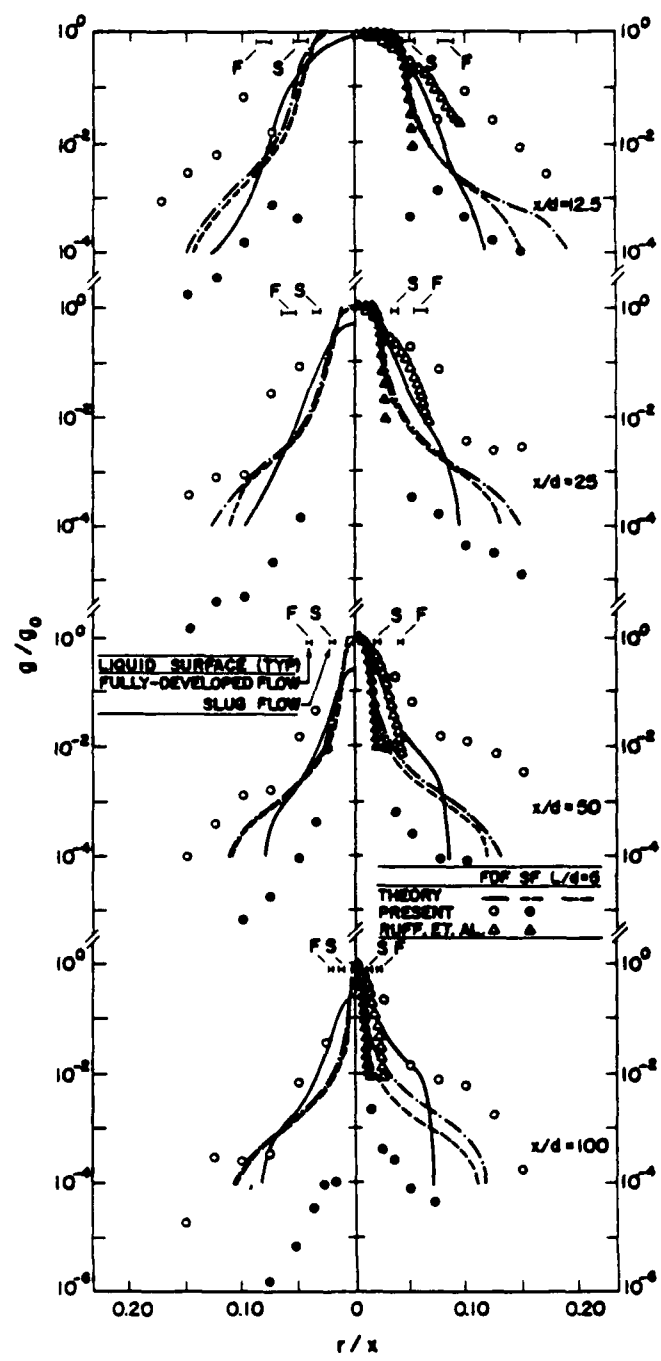


Figure 20 Liquid volume fractions and fluxes at various distances from the injector for atomization breakup and fully-developed and slug flow.

to penetrate across the mixing layer before subsequently breaking up also provides a mechanism for improved mixing, as noted earlier.

The LHF predictions of liquid volume fractions are reasonably good when liquid volume fractions are greater than 0.2, as pointed out earlier. Measurements in the multiphase mixing layer (where α_f is generally less than 0.2), however, are at best only qualitatively similar to the LHF predictions. In view of the velocity measurements illustrated in Figs. 12-19, which exhibit large differences in velocity for drops of different size, this is not surprising. The results also suggest that improved performance of the LHF approach for $\alpha_f > 0.2$ does not result from the LHF approximation being formally satisfied. A more likely explanation is that the dynamics of the flow are dominated by the large liquid elements so that even though the gas and small drops are moving at much lower velocities they do not have a significant effect. This follows since the mass fraction of gas and small drops is small due to the large density ratio of the flow (e.g., liquid volume fractions greater than 0.2 generally correspond to mixture fractions greater than 0.99) and the strong d_p^3 variation of drop mass with drop diameter.

The entrainment rate of a jet is proportional to the rate of increase of the jet mass flow rate with distance from the injector: it is a good measure of the turbulent mixing properties of the flow. Present measured and predicted entrainment rates are plotted as a function of distance from the injector in Fig. 21. Entrainment rates are normalized as suggested by a correlation for fully-developed ($x/d > 20$) variable-density turbulent gas jets due to Ricou & Spalding (1961): they find that the normalized entrainment rate is independent of the initial density ratio of the flow and distance from the injector, as shown on the plot. Present predictions did not vary significantly with Reynolds number; therefore, predictions illustrated in Fig. 21 are representative of the range of the experiments. Similarly, since the slug flow predictions for $L/d = 0$ and 5 yielded essentially the same results, this parameter is also not distinguished in Fig. 21.

Measured normalized entrainment rates, illustrated in Fig. 21, progressively increase in passing from the first wind-induced, to the second wind-induced, to the atomization breakup regime. This behavior is due to atomization quality. The larger drops formed in the wind-induced breakup regimes are less effective in transferring their momentum to the gas phase, which directly reduces the entrainment rate. Results for the first wind-induced breakup regime typify the limit of this behavior since the liquid column did not shatter into drops for the present test range: this provided little surface area to promote interphase momentum exchange and turbulent mixing.

Measured normalized entrainment rates in Fig. 21 increase with increasing distance from the injector for fully-developed flow and second wind-induced or atomization breakup. However, regions where normalized entrainment rates decrease with increasing distance from the injector are observed for the other flow conditions illustrated in the figure. This latter behavior was not anticipated based on predictions. Nevertheless, repeated checks confirmed the results illustrated in Fig. 21. This behavior could be due to the inability of large liquid elements to disperse very effectively in the lateral direction, tending to confine the momentum flux of the flow near the axis. Results for the first wind-induced breakup regime exemplify the limit of this type of behavior – where breakup into drops does not occur at all. Even when breakup occurs in the region of interest, there is a progressive deterioration of atomization quality with increasing distance from the injector, due to reduced shear rates at the liquid surface as the multiphase mixing layer grows. The resulting larger drops tend to have higher relative velocities even if they disperse to the edge of the flow, reducing entrainment rates, as discussed in connection with effects of breakup regime on entrainment. Based on these considerations it is plausible that decreasing normalized entrainment rates with increasing distance from the injector can be observed in

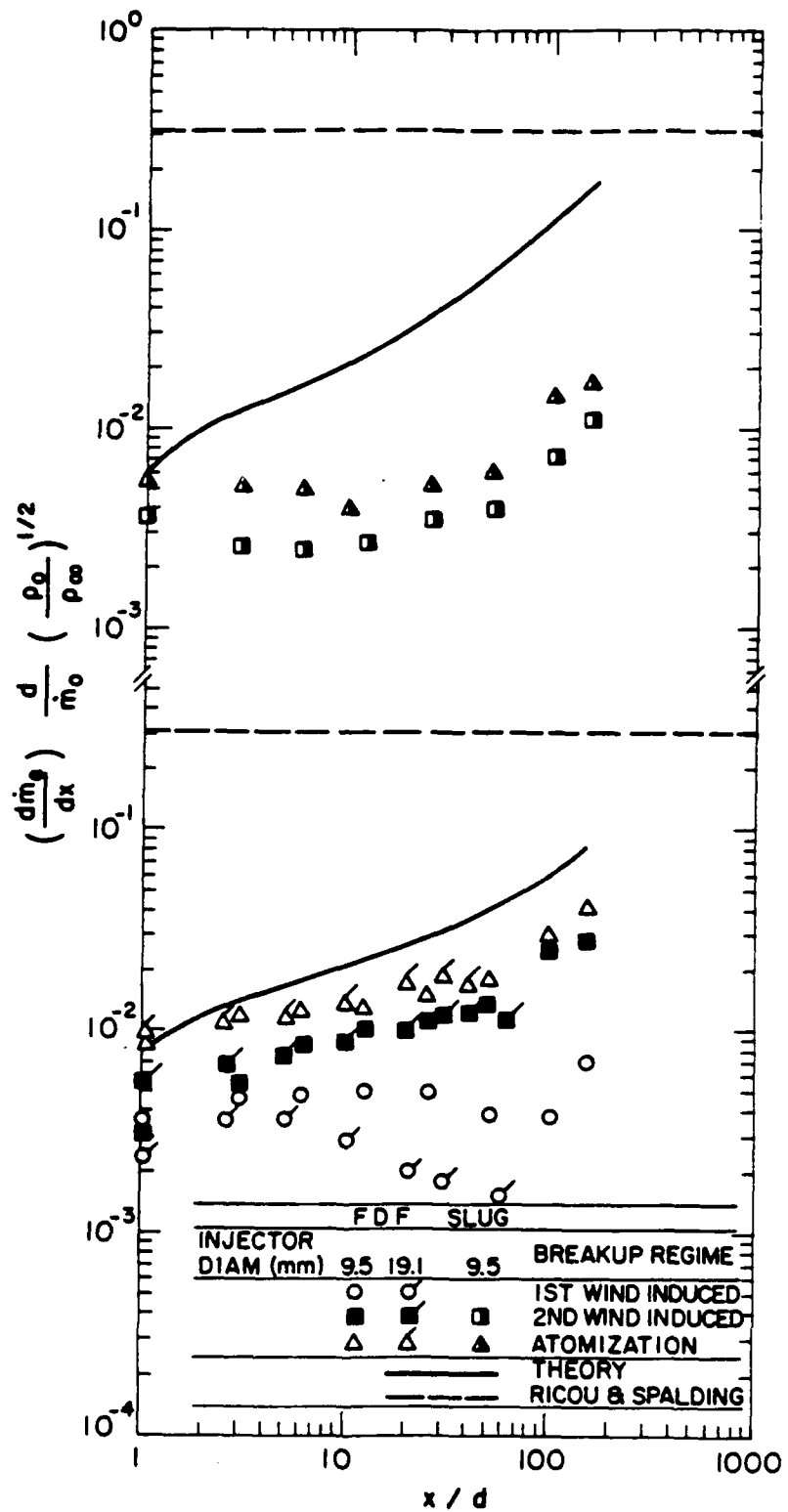


Figure 21 Entrainment rates as a function of distance from the injector for fully-developed and slug flow.

some instances. However, more study is needed to adequately understand the phenomenon.

In general, predictions substantially overestimate measurements for all the results illustrated in Fig. 21. Furthermore, the correlation of Ricou & Spalding (1961) yields much larger estimates of entrainment than present measurements and predictions. This is due to effects of both flow development and finite relative velocities. Differences between the correlation of Ricou & Spalding (1961) and present LHF predictions are a measure of effects of flow development. This is caused by differences between present velocity and density distributions in the developing flow near the injector and velocity profiles for fully-developed turbulent gas jets, which have rather modest density variations in the fully-developed region of the flow. In the terminology of integral theories, this is a shape-factor effect, resulting from dissimilar velocity and scalar property profiles. Similarity in this sense implies invariance of radial profiles when normalized by centerline quantities and plotted as a function of r/x : the results discussed earlier show that this requirement is not satisfied for the present flows – even for atomization breakup.

Present predictions allow for effects of flow development, but still significantly overestimate measured rates of entrainment. The discrepancies are smallest for fully-developed flow and atomization breakup, but even this prediction is not very satisfactory. This behavior follows since entrainment rates are strongly influenced by flow properties near the edge of the flow, where velocities are low and effects of relative velocities become important. Stated differently, the periphery of the flow, which directly affects entrainment properties, is a dilute-spray region where LHF analysis overestimates rates of flow development, which is represented by properties like the entrainment rate.

2.4.4 Discussion

Present measurements support the traditional view of spray structure, involving progressive breakup of larger to smaller liquid elements (Lefebvre, 1980); rather than recent hypotheses that small drops are either formed near the jet exit or are stripped from the surface of the all-liquid core and create larger drops within the multiphase mixing layer by collisions or coalescence (Bracco, 1983; Reitz & Bracco, 1984; Reitz & Diwakar, 1987). It appears that large liquid elements, like ligaments, are formed along the surface of the all-liquid core. These elements then break up into smaller liquid elements either due to the development of residual instabilities within the liquid elements that require additional time to complete their breakup action, or by the development of subsequent instabilities as the liquid elements pass through the relatively slow-moving gas. Smaller drops resulting from breakup adjust more rapidly to local gas velocities so that the resulting reduced relative velocities, combined with larger relative stabilizing effects of surface tension, finally end the breakup process. The smaller drops then spread across the mixing layer through the mechanism of turbulent dispersion. Furthermore, it appears that final requirements of drop stability to subsequent breakup have an important effect on drop size distributions produced in the present sprays. For example, drop sizes near the edge of the flow and at $x/d = 100$ (see Figs. 12-19), are remarkably similar for slug and fully-developed flow even though the nature of the dispersed phase near the liquid surface is very different.

Thus, present results show that dense sprays do not correspond to a flow containing closely-spaced spherical elements dominated by collision processes; instead, they correspond to a relatively dilute flow of irregularly-shaped liquid elements dominated by breakup processes. Current estimates of breakup times of drops suggest that they are comparable to mixing times in sprays (Faeth, 1987), which is consistent with present

observations. Thus, it is likely that analysis of breakup will have to be an integral part of analysis of dense sprays. Fortunately, the fact that the dense-spray region is optically accessible using high-resolution holography should be helpful for gaining a better understanding of the breakup processes relevant to this flow.

The present measurements and LHF calculations also highlight the limitations of the LHF approximation — at least for jet-to-ambient density ratios on the order of 10^3 . For processes relating to the all-liquid core ($\alpha_f > 0.2$) the use of the LHF approximation is helpful; e.g., the approach properly described the striking effect of the degree of flow development at the injector exit on flow properties, and yielded satisfactory predictions of the distributions of mean liquid volume fractions in the streamwise and radial directions for both fully-developed and slug flow at the injector exit. The reason for this success, however, is not that liquid and gas velocities are nearly the same; rather, for the present large density ratio of the jets, values of $\alpha_f > 0.2$ correspond to mixture fractions greater than 0.99 so that the momentum defect of the gas has only a small effect on mixing properties.

Within the multiphase mixing layer, the deficiencies of the LHF approach become more apparent — typical of past evaluations of the LHF approach for dilute sprays (Faeth, 1987). Throughout this layer, liquid velocities vary significantly with drop size, and results for small drops (which probably approximate gas velocities) suggest significant velocity differences between the large drops, which carry the bulk of the momentum, and the gas. Thus, the LHF approach substantially overestimates the rate of development of the flow — particularly as evidenced by the entrainment rates, which are a sensitive indicator of momentum exchange to the gas phase. This finding is reasonably definitive since the present flows have large injector diameters and lower rates of flow deceleration than conventional injectors, which would be less likely to satisfy the LHF approximation. The main factors that could change this conclusion would be higher liquid jet velocities (Reynolds numbers) and higher ambient pressures, both of which would improve atomization. Additional study will be required to determine whether there are interesting operating conditions of sprays where the LHF approximation is useful for low liquid volume fractions.

A final point should be mentioned with respect to the turbulence model. If the present flows formally satisfied the LHF approximation, they would represent a variable density jet with a density ratio of ca. 1000:1. This is roughly two orders of magnitude greater than the variable-density single-phase flows which were used to calibrate the present Favre-averaged turbulence model (Jeng & Faeth, 1984). Thus, whether these methods can accurately handle the present large density ratios if the LHF assumption was formally satisfied is unknown, and deficiencies here could have contributed to discrepancies between predictions and measurements. Based on present findings, however, limitations of the LHF approximation due to finite relative velocities in low mean-velocity regions of the flow (the dilute-spray region) appear to be a more obvious source of errors in the predictions.

2.5 Conclusions

Major conclusions of the study of the structure of dense sprays are as follows:

1. Pressure-atomized sprays are unusually sensitive to the degree of flow development and turbulence levels at the injector exit. Fully-developed turbulent flows cause much faster rates of flow development and

shorter all-liquid cores than slug flows having low initial turbulence intensities.

2. Locally-homogeneous flow analysis was reasonably successful for atomization breakup in the dense-spray, near-injector, region, where mean liquid volume fractions are relatively high ($\bar{\alpha}_f > 0.2$). In particular, present methods provided good estimates of the striking effects of flow development at the injector exit, in spite of the large density variations (ca. 1000:1) of the flows.
3. Use of the LHF approximation was not satisfactory for wind-induced breakup or in the dilute-spray region near the periphery of the flow and far downstream of the injector, the last observation agreeing with earlier findings (Faeth, 1987). These deficiencies are due to larger drop sizes for wind-induced than atomization breakup and lower flow velocities in the dilute than the dense regions of the test sprays. Both effects tend to increase the importance of relative velocities between the phases.
4. Properties of the all-liquid core near the injector exit are influenced by the breakup regime and the state of flow development at the injector exit. The last effect is probably a factor causing differences in all-liquid core lengths reported by various workers (Chehroudi et al., 1985; Hiroyasu et al., 1982; Phinney, 1973).
5. Drop velocities increase significantly with increasing drop size throughout the near-injector region, providing unequivocal evidence of the importance of separated-flow effects in dense sprays. Thus, the success of the LHF approximation at high liquid volume fractions is largely caused by the fact that the momentum of the gas and small drops does not have a strong influence on the dynamics of the flow, since their momentum is a small fraction of the total momentum due to the large density ratio of the flow, even though they have significantly different velocities from the bulk of the liquid.
6. The multiphase mixing layer around the all-liquid core primarily consists of large, irregularly-shaped liquid elements and drops near the core, with the proportion of drops increasing and drop sizes and mean liquid volume fractions decreasing with increasing radial distance. Even near the all-liquid core, however, the gas-containing region is relatively dilute at each instant. This structure implies that breakup and turbulent dispersion of drops are the dominant processes in the multiphase mixing layer — not drop collisions, as has been suggested in the past.
7. The degree of flow development and turbulence levels at the injector exit influences drop size distributions near the liquid surface of the all-liquid core due to distortion and wrinkling of the surface by the liquid-phase turbulence — enhancing normal liquid-jet breakup mechanisms. Drop size distributions near the edge of the flow and toward the downstream end of the dense-spray region, however, are not very different for slug or fully-developed flow at the jet exit. This suggests that local stability of liquid elements to breakup has a strong influence on the eventual outcome of the atomization process.

8. High-resolution double-pulse holography is capable of penetrating the multiphase mixing layer to the surface of the all-liquid core as long as the object beam is not directed through the all-liquid core itself. This instrument provides a valuable approach for studying the properties of dense sprays, since it can deal with irregularly-shaped liquid elements that are problematical for other measurement techniques used in multiphase flows.

Present conclusions are based on large-scale sprays (9.5 and 19.1 mm injector diameters) which have much lower flow deceleration rates than practical injectors — favoring use of the LHF approximation. Present results were also limited to water injected into air at room temperature and pressure. Other liquids and ambient gases will modify drop-size distributions and probably the effectiveness of the LHF approximation as well. Additional study of this important and fundamental multiphase flow is clearly needed.

3. TURBULENCE MODULATION

3.1 Introduction

The objective of this portion of the investigation was to gain a better understanding of turbulence modulation, i.e., the direct modification of continuous-phase turbulence properties by transport from the dispersed phase. Turbulence modulation is most important in dense sprays. However, the process is difficult to study in these circumstances due to the complexity of the flow and limitations of instrumentation. To circumvent these problems a much simpler flow was considered: namely, a homogeneous, dilute, monodisperse particle-laden flow. This provides the multiphase counterpart of homogeneous turbulent flows that have proven to be very helpful for gaining a better understanding of single-phase turbulence. Present flows also exhibited effects of turbulent dispersion. Therefore, this phenomenon was studied as well.

Results illustrating the effect of turbulence modulation, drawn from earlier work in this laboratory (Parthasarathy & Faeth, 1987), appear in Fig. 22. This involves measurements of turbulence kinetic energies in particle-laden water jets in still water for various particle loadings. Near the injector exit, $x/d = 16$, the relative velocity between the particles and liquid is small in comparison to the bulk flow velocity. Therefore, turbulence properties are dominated by conventional processes in the liquid phase and there is little effect of particle loading on the distribution of turbulence kinetic energy. Farther from the jet exit, at $x/d = 40$, however, relative and bulk liquid velocities are comparable, and the turbulence kinetic energy increases significantly with particle loading, particularly near the axis where conventional production of turbulence becomes small. This is a manifestation of turbulence modulation, involving direct contributions to the turbulent energy budget by the wakes of moving particles. Other observations of this phenomena in multiphase dispersed jets and sprays have been reported by Faeth (1983, 1987), Shuen et al. (1985), Solomon et al. (1985, 1985a), Sun & Faeth (1986, 1986a) and Sun et al. (1986), although none of this work involved direct study of turbulence modulation phenomena.

Early work treating turbulence modulation is reviewed by Batchelor (1972) and Hinze (1972). Batchelor's (1972) study was actually more narrowly focussed, being concerned with sedimentation of a dispersion of spheres having sufficiently low Reynolds numbers to be in the Stokes regime. It was shown that the fundamental randomness of

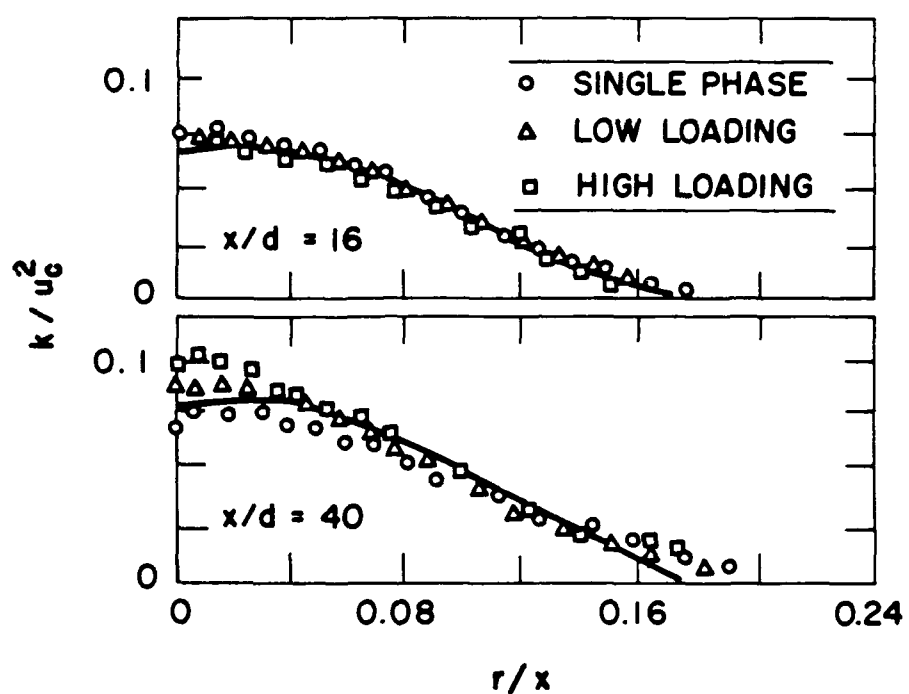


Figure 22 Turbulence modulation in a particle-laden jet.

particle-laden flows yields properties different from those considering fixed arrays. Thus, realistic consideration of turbulence modulation must allow for randomness at the outset. Hinze (1972) reviews early work relating to turbulence modulation in some detail. He also describes several modulation mechanisms: turbulence generation by particles, where the turbulent wakes of particles supplement turbulence generation by conventional single-phase mechanisms like turbulence production by shear forces; turbulence modification, where the instantaneous velocity fields of particle wakes influence local turbulence production; and turbulence dissipation by particles, where acceleration of particles by turbulent fluctuations extracts turbulence energy from the flow. Subsequently, Al Tawee & Landau (1977) considered the turbulence dissipation mechanism for two-phase jets — coining the terminology "turbulence modulation" for processes of this type. Their theoretical attempt to describe turbulence dissipation by particles was not very successful, however, largely due to difficulties with the data base that they used to develop their approach (Faeth, 1977; 1983). Subsequently, there were numerous attempts to treat turbulence dissipation phenomena with models based on higher-order turbulence closures, see Faeth (1987) for a review of this work.

One of the most complete studies of turbulence modulation phenomena has been reported by Lance & Bataille (1982) and Lance et al. (1980, 1985). This involved bubbly air/water flows in a vertical duct downstream of a turbulence generating grid. Similar to the results of Fig. 22, high void fractions and low mean velocities, comparable to the relative velocities of the bubbles, caused substantial increases in turbulence intensities. Other properties of the turbulence were modified as well, e.g., temporal power spectral densities and correlations, skewness and flatness factors of the probability density functions of velocity fluctuations, dissipation rates, and length scales. Some success was also achieved in modifying a second-order closure to treat effects of turbulence modulation on the streamwise variation of the Reynolds stress tensor for a bubbly shear flow (Lance et al., 1985).

Initial work on turbulent dispersion of particles concentrated on the small particle limit, where relative velocities between the phases are small and particle mixing can be approximated by single-phase scalar mixing through the LHF approximation — see Faeth (1977, 1983, 1987) for a review of this approach. The LHF approximation is of limited value, however, since most practical multiphase flows involve significant relative velocities between the phases, and dispersed phases do not remain associated with particular fluid elements. This phenomenon, recognized by Yudine (1959) and Csanady (1963), is called the "crossing-trajectories" effect, i.e., dispersed-phase elements and turbulent eddies follow different trajectories and only interact for a time. Katz (1966) and Meek & Jones (1973) report early applications of these ideas to the study of dispersion of heavy particles in the atmosphere. Other work, at the Stokes limit for particle motion with various approximations for the continuous phase of simple turbulent flows, includes Reeks (1977, 1980), Pisman & Nir (1978), Nir & Pisman (1979), Gouesbet et al. (1984) and Desjonquieres et al. (1986). All these studies find significant effects of finite relative velocities between the phases and other separated-flow phenomena.

Snyder & Lumley (1971) reported an early experiment that emphasized effects of turbulent dispersion that has served as a source of data for development of models of the process. They studied the dispersion of particles that were injected isokinetically (in the mean) into a uniform turbulent flow downstream of a grid. Wells & Stock (1983) studied turbulent particle dispersion in a similar arrangement, using charged particles in an electric field, so that effects of relative velocities (crossing trajectories) could be separated from particle inertia. They found that inertia influenced fluctuating particle velocities but concluded that particle dispersion was primarily influenced by crossing trajectories for their test conditions. Ferguson & Stock (1986) also studied particle dispersion in grid-generated

turbulence, further highlighting effects of crossing trajectories. Taken together, these results demonstrate the importance of both particle and continuous-phase properties on turbulent particle dispersion. Therefore, the process does not lend itself to empirical correlation and must be understood at a fundamental level before reliable estimates of turbulent dispersion can be achieved.

In spite of progress in the past, it is clear that further theoretical and experimental study is needed to provide a better fundamental understanding of turbulence modulation and turbulent dispersion. Important effects of turbulence modulation have been observed, but the effects vary, depending upon experimental conditions. The physical nature of phenomena is unknown, and reliable predictive methods have not been developed. Turbulent dispersion has received more attention, and stochastic methods for predicting this phenomena appear to be promising. However, existing measurements for well-defined fundamental turbulent flows are limited, which has inhibited the development of rational predictive methods.

The objective of the present investigation was to provide new theoretical and experimental results concerning turbulence modulation and turbulent dispersion in homogeneous particle-laden turbulent flows. In a general sense, the present study is an extension of the investigation of homogeneous bubbly turbulent flows of Lance & Bataille (1982) and Lance et al. (1985). Rather than contend with the complications of grid-generated turbulence in a flowing continuous phase, however, the present study was limited to a uniform flux of particles moving through a nearly stagnant (in the mean) liquid. This provides a fully homogeneous, turbulent, particle-laden flow, where all turbulence properties are due to the relative motion of the particles, i.e., the entire flow field is the result of turbulence modulation phenomena. The particular configuration considered during the present study involved nearly monodisperse spherical glass beads falling under the action of gravity in a nearly stagnant (in the mean) water bath. Measurements were made of phase velocities and temporal and spatial correlations of the continuous phase velocities, using a two-point phase-discriminating laser velocimeter (LV); and of particle fluxes, using Mie scattering. Additionally, particle motion properties were assessed using motion-picture shadowgraphs. Analysis was also undertaken using stochastic methods to describe processes in both the dispersed and continuous phases.

In the following, experimental and theoretical methods are described first. Results are then considered, treating the properties of the continuous and dispersed phases in turn.

3.2 Experimental Methods

3.2.1 Apparatus

Figure 23 is a sketch of the homogeneous particle-flow apparatus. The test configuration involved nearly monodisperse round glass particles (nominal diameters of 0.5, 1.0 and 2.0 mm) settling with a uniform flux in a nearly stagnant water bath. Measurements included phase velocities, using a phase-discriminating LV; and particle number fluxes, using Mie scattering.

The particle flow was initiated by a particle feeder (AccuRate, Model 310, with a 19 mm diameter helix with center rod for 1 and 2 mm particles and with a 25 mm diameter helix with center rod for 0.5 mm particles). The particles were dispersed by falling through an array of 9 screens (stainless steel wire mesh cloth: 0.58 mm diameter wire spaced 2.1 mm apart, 52.4 percent open area for 0.5 and 1.0 mm diameter particles; 0.89 mm diameter wire spaced 4.2 mm apart, 62.4 percent open area for 2.0 mm diameter particles), with a

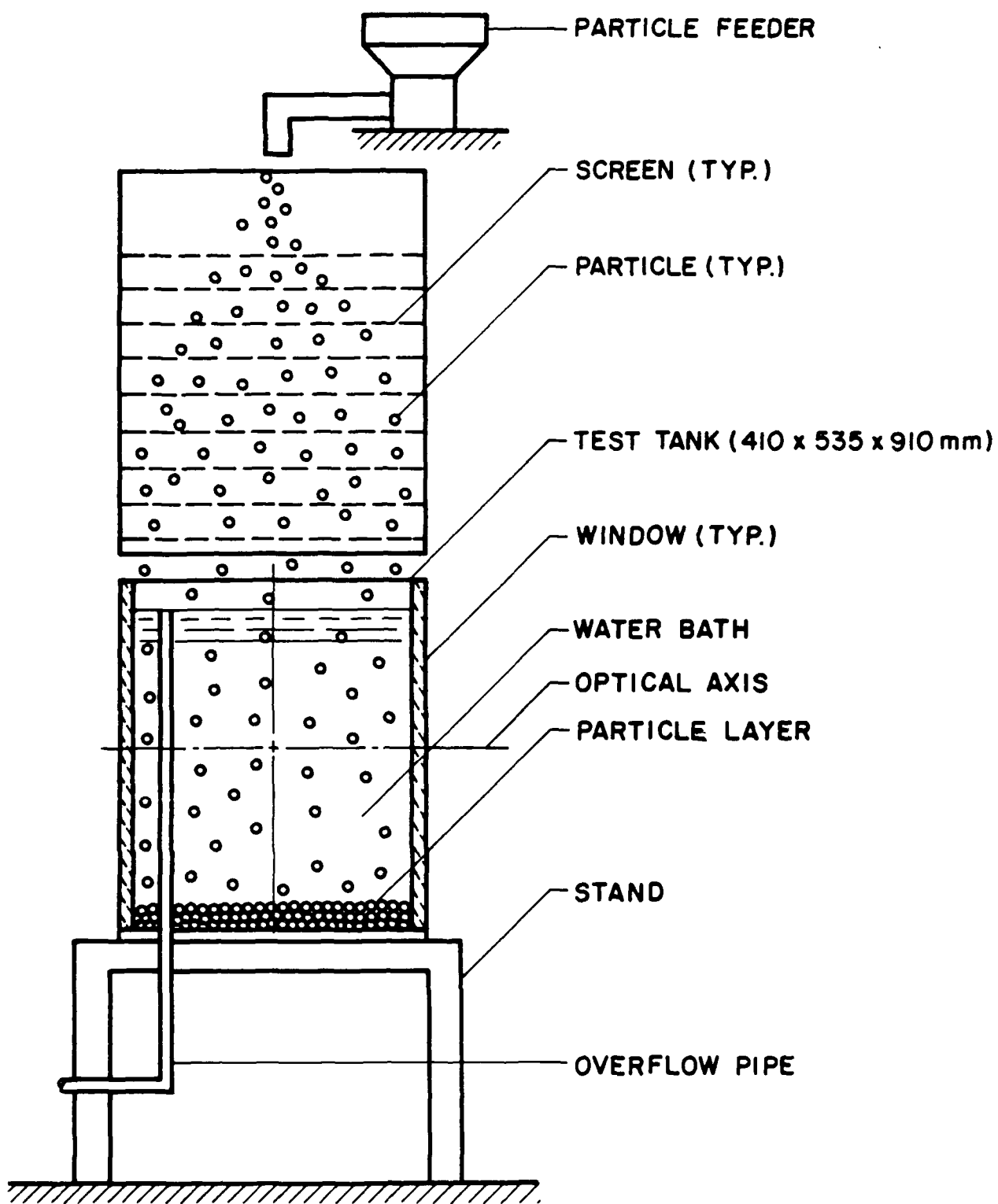


Figure 23 Sketch of homogeneous particle-flow apparatus.

190 mm spacing between the screens. The particles then fell into a windowed tank (410 × 535 × 910 mm high), which was filled with water to a depth of 800 mm. After a deceleration distance of 100-200 mm, the particles reached a steady (in the mean) terminal velocity. Although the particles entered the dry bath, little difficulty was encountered with particles becoming trapped in bubbles (less than 1 percent). Observations were made near the center of the tank (roughly at a depth of 400 mm). The particles then collected naturally at the bottom of the tank, with little rebound upon impact, and were removed from time-to-time using a suction system.

The test arrangement is conceptually simple and yields a homogeneous dilute dispersed flow, where all turbulence in the system is produced directly by the particles. The particle feed system was evaluated for dry operation, showing essentially uniform particle fluxes across the exit, within experimental uncertainties. Results to be discussed later show that uniform particle fluxes were preserved in the liquid phase and that flow properties were relatively insensitive to disturbances of the uniformity of particle fluxes and changes in the volume of the windowed tank.

Three sources of mean motion in the bath were present: water displacement by particles, thermal disturbances, and nonuniformity of particle fluxes near the walls of the test chamber. Effects of water displacement by particles were negligibly small, not exceeding 0.014 mm/s in comparison to liquid velocity fluctuations of 1-10 mm/s. Some mean liquid motion was observed when particles were not entering the bath caused by effects of buoyancy forces due to thermal nonuniformities. Buoyancy intruded, since the liquid bath had an appreciable thermal capacity, while the laboratory had relatively poor temperature control. As a result, the bath was invariably either heating up or cooling down, yielding mean velocity levels on the order of 1 to 2 mm/s. However, once the flow of particles was initiated, the thermal motions were nearly destroyed, and particle effects dominated the flow in the bath. Mean velocities were still observed when particles were flowing, however, due to reduced particle fluxes very near the walls, which set up a recirculating flow in the tank. This effect was handled during data reduction, as discussed later.

3.2.2 Instrumentation

Liquid-Phase Laser Velocimetry. Phase-discriminating LV was used to measure mean and fluctuating phase velocities and one- and two-point liquid velocity correlations. The LV for liquid velocity measurements involved one fixed channel and one channel that could be traversed in both the streamwise and cross-stream directions. The two channels were based on the green (514.5 nm) and blue (488 nm) lines of a 2W argon-ion laser operating in the multiline mode. The green and blue lines of the laser were separated using a dichroic green mirror. The blue line was transmitted to the sending optics of the traversable channel using a fiber-optic cable. Both channels operated in the dual-beam forward-scatter mode. Directional bias and ambiguity were eliminated using a 40 MHz Bragg-cell frequency shifter with the output signals downshifted to convenient frequency ranges (0.05-0.1 MHz) for filtering and signal processing. Streamwise and cross-stream velocities were measured by rotating the LV optics appropriately.

Titanium dioxide particles in rutile form (nominal size 2.8 μm) were used as LV seeding particles for liquid velocity measurements. One-half gram of the seeding particles was mixed with 500 ml of water and then added to the bath. It took about fifteen minutes for the seeding particles to be distributed throughout the bath and 12 hours for them to settle to the bottom. Since the longest test time extended roughly three hours, the settling

of seeding particles did not alter data rates significantly. This seeding level provided data rates between 2-4 kHz over the present test range.

Light scattered by the seeding particles yielded lower amplitude signals than light scattered by the glass beads; therefore, simple amplitude discrimination could be used to distinguish between the liquid-phase and particle velocity signals. As Modarress et al. (1984) point out, however, particles grazing the LV measuring volume also yield low amplitude signals, which could be interpreted as liquid-phase signals, thus biasing the liquid-phase velocity measurements. This can be a serious problem for the present particle-laden flows, where the relative velocities between the phases were large in comparison to liquid velocity fluctuations. Thus, a phase-discrimination system was used on both channels to avoid biasing from particles making grazing collisions with the LV measuring volume. This arrangement involved a third beam from a 5 mW HeNe laser (at an angle of 18° from the LV axis), which enveloped each LV measuring volume, and collection optics set off-axis (at an angle of 32° from the LV axis). The region viewed by the discriminator system (0.6 mm diameter and 1.3 mm long) surrounded the LV measuring volume (0.1 mm diameter and 1.2 mm long). Thus particles that grazed the measuring volume yielded a scattering signal that was picked up by the detector in the discriminator system. The signal from the discriminator was recorded simultaneously with the LV signal. The data processing system was programmed to eliminate all liquid-phase velocity records where a pulse on the discriminator signal indicated the presence of a particle near the measuring volume.

The time between valid liquid velocity measurements was very small in comparison to integral time scales of the flow (ca. 0.02-1 ms in comparison to 4-7 s). Therefore, the velocity signals were time-averaged, ignoring periods when particles were present, to obtain unbiased time-averaged liquid velocities. The results from direct time-averaging without correction for signals from particles and the results from averaging with the phase-discriminator operating differed by less than two percent. This is understandable, since the present flows were dilute (the volume fractions of particles were less than 0.01 percent). Nevertheless, the phase-discrimination system was used during all liquid-phase measurements in order to minimize experimental uncertainties.

The analog velocity signal was filtered using an Ithaco low-pass filter before the signal was digitized and transferred to the microcomputer. It was found that averaging signals for twenty minutes provided repeatable results for mean and fluctuating velocities and probability density functions. The one-point temporal spectra were obtained through about seven orders in frequencies. These spectra were obtained by collecting data at three sampling frequencies: 2500 Hz, 50 Hz and 7.5 Hz with low pass-filter settings at 1000 Hz, 25 Hz and 4 Hz, respectively. A total of 65,000 data points were collected for each run and stored on floppy disks. The spectra were obtained from 4096 points at each sampling frequency, averaging over 80-90 such groups to obtain final results. The spectra at different sampling frequencies overlapped and were matched at the common frequencies. The total area under the combined spectrum was then normalized to unity.

Two-point velocity correlations were measured by traversing one channel with respect to the other. The LV on the traversing channel was based on the blue line of the argon-ion laser (488 nm). The blue line was split from the laser beam using a dichroic (green) mirror, and was coupled to the traversing channel using a fiber-optic cable. The transmitting efficiency of the fiber optic cable varied in the range 7-14%. Due to deterioration of the cable it was necessary to replace the cable once during the period of testing in order to maintain this usable range of transmission efficiencies. The output power of the blue line was 25 mW. The input coupler had to be adjusted before every run to maximize the transmitting efficiency. The phase-discriminator system on this channel

was similar to the fixed channel. The output power on the green line was 100 mW for these measurements, since this setting was found to give the maximum signal-to-noise ratio on both channels. The LV measuring volume on the blue channel was 1.2 mm long and 0.1 mm in diameter, and the fringe spacing was 2.4 microns. Data rates on this channel were 1-3 kHz.

Parthasarathy (1989) describes evaluation of bias errors and experimental uncertainties of the LV measurements. Bias errors were small, less than one percent. Analysis indicated the following experimental uncertainties (95% confidence): mean streamwise velocities, less than 10%; mean cross-stream velocities, less than 40%; fluctuating streamwise velocities, less than 14%; fluctuating cross-stream velocities, less than 21%; temporal spectra of streamwise velocity fluctuations, less than 35% for frequencies below 10^{-2} Hz and less than 16% for all other frequencies; temporal spectra of cross-stream velocity fluctuations, less than 42% for frequencies below 10^{-2} Hz and less than 21% for all other frequencies; two-point spatial correlations in the lateral direction, less than 29%; two-point spatial correlations in the streamwise direction, less than 36%; Reynolds stresses, less than 55%. All the uncertainties were dominated by finite sampling times.

Particle-Phase Laser Velocimetry. The particle velocities were measured using the fixed LV channel. A beam spacer was added to provide a 9 mm beam spacing while the receiving optics were shifted off-axis to 45° from the forward scatter direction. In this case, the fringe spacing was $14.3 \mu\text{m}$ and the measuring volume was $300 \mu\text{m}$ in diameter and $300 \mu\text{m}$ long. Frequency shifting and the use of different beam orientations to obtain various velocity measurements were the same as the liquid-phase measurements.

Signals from natural seeding particles within the liquid were eliminated by operating the detector at a low gain which only responded to large-amplitude signals from particles. In this case, the discriminator system was used to validate the presence of a particle when the signal was recorded. Particle arrival rates were low (10-80 per hour). Number averages of velocities were taken over 200-500 particles.

For these measurements, Parthasarathy (1989) finds the following experimental uncertainties (95% confidence): mean streamwise particle velocities, less than 6%; mean cross-stream particle velocities, less than 41%; fluctuating streamwise particle velocities, less than 11%; fluctuating cross-stream particle velocities, less than 16%. These uncertainties were largely dominated by finite sampling times.

Particle Number Fluxes. Particle number fluxes were measured with a Mie scattering system similar to Sun et al. (1986). A small light sheet having nearly uniform intensity was produced at the measuring volume by passing the beam from a 5 mW HeNe laser through an aperture. The measuring volume was observed in the horizontal plane, normal to the laser beam. Particles passing through the measuring volume generated pulses in the detector output. The pulses were shaped and recorded by a pulse counter which had an adjustable threshold to control spurious background signals. Grazing collisions of particles with the optical measuring volume were recorded; therefore, the radius of the region observed was roughly the sum of the optical radius and the particle radius. The actual area of observation, however, was calibrated by collecting particles for timed intervals. In general, more than 500 particles were counted in order to find the mean particle number flux.

Experimental uncertainties for the particle number flux measurements were due to variable particle diameters, which influenced the area actually observed, and finite sampling

times. The latter dominated the measurements, yielding uncertainties (95% confidence) of less than 10%.

Particle fluxes were also checked for uniformity by placing trays (75 mm × 60 mm) in the bottom of the test tank and weighing the particles (after drying) collected for timed intervals. Experimental uncertainties of these measurements were largely governed by limitations of finite sampling times yielding uncertainties (95% confidence) less than 15%. These measurements confirmed the Mie scattering measurements within the experimental uncertainties of each.

3.2.3 Particle Properties

Glass particles having nominal diameters of 0.5, 1.0 and 2.0 mm and a density of 2450 kg/m³ were used during the tests. The particles were not truly monodisperse but had Gaussian diameter distributions with standard deviations of roughly 10% of the particle nominal diameter. Furthermore, the particles were all not truly spherical: 20% of the 0.5 mm particles were ellipsoids with a mean ellipticity (ratio of the major diameter to the minor diameter) of 1.05; 40% of the 1.0 mm particles were ellipsoids with a mean ellipticity of 1.15; and 65% of the 2.0 mm particles were ellipsoids with a mean ellipticity of 1.25.

It was found that particles dropped individually in a still bath did not fall straight. Instead, they exhibited some lateral motion, with the degree of lateral motion increasing with increasing particle size. This effect was measured by dropping individual particles into a still bath and recording their trajectory as a motion-picture shadowgraph. See Parthasarathy (1989) for details. The resulting particle tracks were then differentiated to yield velocities using a central-difference scheme. Mean and fluctuating velocities were calculated for each particle path and then averaged over 50 particles. Uncertainties (95% confidence) were governed by sampling limitations and were less than 15% for mean streamwise velocities and less than 30% for velocity fluctuations.

The mean streamwise velocities and the streamwise and crosstream velocity fluctuations of the particles due to self-induced motion are summarized in Table 3. The mean particle velocities agree with values found using LV, to be taken up later, within experimental uncertainties. The streamwise velocity fluctuations due to self-induced particle motion are small in comparison with apparent fluctuations due to size variations, i.e., due to differences of particle terminal velocities within the range of particle diameters for each nominal particle size. The lateral velocity fluctuations, however, are significant and increase rapidly with increasing particle diameter. This is due to increased eddy-shedding behind the particle at higher terminal Reynolds numbers (Nakamura, 1976), as well as increased ellipticity with increasing particle size. Because of the large value of the self-induced lateral velocity fluctuations, comparable to liquid velocity fluctuations, the 1.0 and 2.0 mm particles do not serve as good indicators of turbulent dispersion during the present study. However, results for the 1.0 and 2.0 mm diameter particles concerning liquid-phase properties are still relevant to the study of turbulence modulation.

Measurements were also undertaken to find whether or not the dispersing screen arrangement induced any lateral motion of the particles. This was a concern, since impact of the particles on the screens could cause them to spin, with resulting Magnus forces deflecting them in a lateral direction. This effect was studied by dropping particles individually through the dispersing screen arrangement into the bath and measuring particle velocities using shadowgraph movies. Results of these experiments for the 2.0 mm particles are also summarized in Table 3. The measurements of mean and fluctuating velocities of the particles passing through the screen arrangement were not significantly

Table 3 Summary of Self-Induced Particle Motion Properties

Property	d _p (mm)			
	0.5 ^a	1.0 ^a	2.0 ^a	2.0 ^b
\tilde{u}_p (mm/s)	71	157	270	274
$(\tilde{u}_p^2)^{1/2}$ (mm/s)	2.0	1.5	0.5	0.5
$(\tilde{v}_p^2)^{1/2}$ (mm/s)	1.1	5.6	13.5	13.1

^aMeasurements from individual particles dropped near the water surface.^bMeasurements from individual particles dropped through the dispersing-screen arrangement.

different from the measurements of velocities of particles dropped directly in the bath. Thus, it is concluded that the dispersing screen arrangement did not modify particle properties appreciably.

Particle drag properties were also calibrated by releasing particles singly within the still water bath and measuring their terminal velocities with the LV system. In this case, a larger number of particles were used, and uncertainties (95% confidence) were less than 9% (Parthasarathy, 1989). Measured PDF's of particle velocities were then compared with predicted PDF's, based on the measured size distribution and the standard drag curve for spheres (Putnam, 1961), as follows:

$$C_D = 24 (1 + Re^{2/3} / 6) / Re, \quad (3.1)$$

where the particle Reynolds number is defined as follows:

$$Re = U_\infty d_p / v. \quad (3.2)$$

Equation (3.1) is limited to $Re < 1000$, which is satisfactory for present test conditions. Predictions were corrected to match the measured mean terminal velocities by multiplying the standard drag correlation of equation (3.1) by a fixed constant for each particle size, as follows: 1.14, 1.00 and 1.14 for the 0.5, 1.0 and 2.0 mm diameter particles, respectively. In view of the ellipticity variations of the particles and anticipated uncertainties in the standard drag correlation, these corrections are surprisingly small.

The comparison between predicted and measured probability density functions of particle velocities was quite good (Parthasarathy, 1989). This indicates that particle size variations were responsible for most of the variance of the terminal velocities of the particles. Since the corrections to the standard drag correlation were small and particle velocity PDF's were reasonably good, based on the corrected drag expression, this expression was used for all subsequent calculations of particle drag.

3.2.4 Test Conditions

A range of particle fluxes were studied for each particle size: Table 4 is a representative summary of test conditions at low and high particle fluxes for each particle size. Particle terminal velocities in a still bath agreed with measurements made during evaluation of self-induced motion, within experimental uncertainties, as noted earlier. Particle Reynolds numbers were in the range 38-545, which is appropriate for the drag correlation of equation (3.1). Particle volume fractions were computed from the following expression:

$$\alpha_p = \pi \dot{n}^n d_p^3 / (6 \tilde{u}_p), \quad (3.3)$$

noting that \tilde{u}_p was very close to the terminal velocity of a freely-falling particle in an infinite environment for present conditions. Particle volume fractions were less than 0.01%. Therefore, the test flows were very dilute. Mean particle spacings were calculated assuming that the particles were falling randomly with a uniform mean particle number flux, yielding:

$$\ell_p = (\tilde{u}_p / \dot{n})^{1/3}. \quad (3.4)$$

Table 4 Representative Homogeneous Particle-Flow Test Conditions^a

Particle Diameter, d_p (mm)	0.5 (0.045)	1.0 (0.085)	2.0 (0.15)			
Particle Loading	Low	High	Low	High	Low	High
<u>Particle Properties:</u>						
Terminal Velocity (mm/s) ^b	65 (6.5)	147 (14.1)	262 (16.0)			
Reynolds Number (-)	38	156	545			
Number Flux (k part/m ² s)	55.4	110.8	3.7	20.9	1.1	3.3
Volume Fraction (% × 10 ³)	5.0	10.0	1.5	8.5	1.8	5.1
Mean Spacing, ϱ_p (mm)	10.5	8.2	32.7	18.3	61.8	43.2
ϱ_p / d_p	21.0	16.4	32.7	18.3	30.9	21.6
\tilde{u}_p (mm/s)	66.8	71.5	144.2	139.0	265.0	265.0
\tilde{u}_p'' (mm/s)	11.0	12.1	17.0	21.9	19.0	20.5
\tilde{v}_p'' (mm/s)	2.7	4.4	2.5	7.4	7.8	9.8
<u>Liquid Properties:</u>						
Rate of Dissipation (mm ² /s ³)	53.2	106.3	27.3	155.8	61.7	193.5
Displacement Velocity (μ m/s)	4	7	2	11	5	14
$\epsilon_{pl} / \epsilon_{pm}$ (%) ^c	1.8	4.5	0.3	1.8	0.4	0.9
\bar{u} (mm/s)	1.6	3.9	1.0	3.8	3.0	6.0
\bar{v} (mm/s)	0.7	0.6	1.1	1.6	1.0	0.9
\bar{u}' (mm/s)	3.3	4.7	2.4	5.1	3.7	6.1
\bar{v}' (mm/s)	1.6	2.7	1.2	2.3	1.7	3.1

^aRound glass beads, density of 2450 kgm/m³, falling in a stagnant water bath at 298 ± 2K. Numbers in parentheses denote standard deviations.

^bMean value from entire distribution falling in a stagnant bath.

^cEstimated upper bound of direct dissipation by particles.

The resulting spacings were in the range 8-62 mm or 16-33 particle diameters. Therefore, effects of direct particle-to-particle interactions were small.

Surprisingly, present test conditions for glass particles falling in water bear some resemblance to the properties of rainstorms. For example, Humphreys (1964) defines the following categories of rainstorms: "light rain" ($d_p = 0.5$ mm, $\ell_p/d_p = 120$), "moderate rain" ($d_p = 1.0$ mm, and $\ell_p/d_p = 120$), and "excessive rain" ($d_p = 2.0$ mm, $\ell_p/d_p = 70$). Furthermore, the Reynolds numbers of the present particles at their terminal velocities are nearly the same as water drops of the same size at their terminal velocities in air. Thus, except for a somewhat smaller particle spacing, present tests for particle diameters of 0.5, 1.0 and 2.0 mm correspond to light, medium and excessive rain, as defined by Humphreys (1964).

Within the region where measurements were made, the mean velocities of particles were constant and were much greater than their velocity fluctuations. Then the rate of dissipation of turbulence kinetic energy can be equated to the rate of production of turbulence by particles, assuming that effects of fluctuations of particle velocities were small. When this is true, the rate of production of turbulence is equal to the rate of loss of the potential energy of the particles as they fall in the bath, yielding the following expression for the rate of dissipation of turbulence kinetic energy:

$$\epsilon = \pi n a d_p^3 (\rho_p - \rho) / 6\rho. \quad (3.5)$$

The values of dissipation for the different tests are tabulated in Table 4. In the following, dissipation will be used to characterize the measurements, since it provides a basis to compare results for different particle sizes and number fluxes using a single parameter.

In a particle-laden flow, the dissipation of turbulence consists of two components: conventional dissipation by the continuous phase, and direct dissipation by interactions between the particles and the continuous phase--the last being the turbulence modulation contribution usually considered in higher-order turbulence models of the process (Faeth, 1987). The degree of direct dissipation by the particles can be found by noting that the instantaneous rate of dissipation per particle is equal to the product of the drag force and the relative velocity, as follows:

$$\epsilon_p = 3\pi v d_p (1 + Re^{2/3}/6)(u_i - u_{pi})^2 \quad (3.6)$$

where the drag coefficient has been obtained from equation (3.1). The time-averaged dissipation per particle then becomes

$$\bar{\epsilon}_p = 3\pi v d_p [(1 + Re^{2/3}/6)(\bar{u}_i - \bar{u}_{pi})^2 + (1 + 10Re^{2/3}/27)(\bar{u}'_i - \bar{u}'_{pi})^2] \quad (3.7)$$

The first term on the RHS of equation (3.7) represents dissipation due to the mean drag and relative velocity. It is the component of dissipation that is analogous to the production of turbulence considered in equation (3.5). The second term on the RHS of equation (3.7) represents the direct contribution of the particle to the dissipation of turbulence. It is the part that was ignored when deriving equation (3.5). Denoting the direct contribution of the particles to dissipation to be ϵ_{pt} and dissipation due to mean drag of particles to be ϵ_{pm} and dissipation due to mean drag of particles to be ϵ_{pm} , the ratio of these quantities becomes

$$\frac{\epsilon_{pt}}{\epsilon_{pm}} = \frac{(1+10Re^{2/3}/27)(\bar{u}_i' - u_{pi}')^2}{(1 + Re^{2/3}/6)(\bar{u}_{pi}^2 - \bar{u}_i^2)} \quad (3.8)$$

It helps to define present experimental conditions to determine $\epsilon_{pt}/\epsilon_{pm}$. Estimates can be made, since most of the terms on the RHS of equation (3.8) were measured. First of all, the terminal velocity in the streamwise direction is much greater than the other components of the particle velocity, so that $u_p^2 \approx u_{pi}'^2$, and \bar{u}_p was measured. Next, the measurements revealed that $\bar{u}_p \gg \bar{u}_i$ so that the latter can be ignored while the Reynolds number can be found using u_p in equation (3.2). The remaining term in the numerator of equation (2.8) can be written as follows

$$(\bar{u}_i' - u_{pi}')^2 = \bar{u}_i'^2 + \bar{u}_{pi}'^2 - 2 \bar{u}_i' \bar{u}_{pi}' . \quad (3.9)$$

The streamwise and crosstream velocity fluctuations of the liquid were measured and, noting that velocity fluctuations in the crosstream direction are isotropic, we have $\bar{u}_i'^2 = \bar{u}'^2 + 2 \bar{v}'^2$. It will be seen later that particle velocity fluctuations in the streamwise direction are dominated by effects of particle size variations which cause variations of terminal velocities. This does not represent a proper measure of particle velocity fluctuations for the estimation of dissipation. A more realistic measure is the cross-stream particle velocity fluctuations, which will be shown to be relatively insensitive to particle size variations. Thus, we make the following approximation, $\bar{u}_{pi}'^2 = 3 \bar{v}_p'^2$, assuming that the velocity fluctuations of particles are isotropic. Proceeding in the same manner for $u_i' u_{pi}'$, equation (3.9) becomes

$$(\bar{u}_i' - u_{pi}')^2 \approx \bar{u}'^2 + 2\bar{v}'^2 + 3\bar{v}_p'^2 - 2\bar{u}'\bar{v}_p' - 4\bar{v}'\bar{v}_p' . \quad (3.10)$$

Now $\bar{u}'\bar{v}_p'$ and $\bar{v}'\bar{v}_p'$ were not measured, but from Schwarz' inequality $|\bar{u}'\bar{v}_p'| < (\bar{u}'^2 \bar{v}_p'^2)^{1/2}$ and $|\bar{v}'\bar{v}_p'| < (\bar{v}'^2 \bar{v}_p'^2)^{1/2}$. Therefore,

$$\frac{\epsilon_{pt}}{\epsilon_{pm}} < \frac{(1+10Re^{2/3}/27)(\bar{u}'^2 + 2\bar{v}'^2 + 3\bar{v}_p'^2 + 2(\bar{u}'^2\bar{v}_p'^2)^{1/2} + 4(\bar{v}'^2\bar{v}_p'^2)^{1/2})}{(1 + Re^{2/3}/6)\bar{u}_p^2} . \quad (3.11)$$

The present measurements of \bar{u}'^2 , \bar{v}'^2 and $\bar{v}_p'^2$ are summarized in Table 4. Substituting these results into equation (3.11) yields the estimates of the upper bound of $\epsilon_{pt}/\epsilon_{pm}$ summarized in Table 4. In general, the ratio is largest at highest particle loadings, where the velocity fluctuations are highest, since more particles are present. The ratio also increases as particle size decreases, since \bar{u}_p^2 becomes smaller and there is less generation of turbulence in the bath per particle. In general, however, $\epsilon_{pt}/\epsilon_{pm}$ is less than 5% for present test conditions, which reflects the fact that the flows are dilute. Thus, generation of turbulence by the particles, coupled with conventional dissipation of turbulence in the continuous phase (perhaps associated with processes in particle wakes), are the dominant features of the present flows. Direct dissipation of turbulence by the particles, which is often the only aspect of turbulence modulation considered in some models of dispersed turbulent flow (Faeth, 1987), is a secondary effect for present test conditions. Finally, estimates of dissipation from equation (3.5), where the direct dissipation by particles is

ignored, are reasonably accurate for present results. The properties of mean and fluctuating liquid velocities, summarized in Table 4, will be taken up later.

3.3 Theoretical Methods

3.3.1 Continuous Phase

General Description. The continuous phase of the present flows involves an infinitely-large range of length and time scales extending from the small scales associated with the flow near a particle to the infinitely-large scales eventually associated with particle wakes. Thus, exact numerical simulation of these flows will never be possible, and some degree of modeling must be accepted at the outset. The objective of the present work was to develop an approximate analysis of the process in a mechanistic way in order to provide some guidance for interpretation of the measurements rather than adopt an approach involving a higher-order turbulence model.

In deciding the approach to the problem two limiting types of analysis were considered, as follows: (1) methods used to treat homogeneous turbulent flows employing time-averaged governing equations for turbulence quantities, analogous to the methods reviewed by Hinze (1975) for isotropic turbulence; and (2) methods that explicitly consider the properties of the flow field associated with individual particles as they move through the flow field in a random way, analogous to the method used by Batchelor (1972) for sedimentation processes. Methods used for isotropic turbulence are normally applied to grid-generated turbulence, where the grid is somewhat analogous to the particles in the present flows. However, this type of analysis is only applied at some distance downstream of the grid, where the properties of individual wakes behind grid elements have been lost, so that the flow is a nonstationary decaying isotropic turbulent flow. This is a serious limitation for the present problem, since the flow is stationary, and wake sources are present throughout the flow field, i.e., the spacing between present particles is not large in comparison to distances where identifiable wake properties are likely to be present. In this circumstance, a method that explicitly considers the existence of a flow field associated with an individual particle, analogous to the approach used by Batchelor (1972) to study particle sedimentation, seems preferable and was pursued.

Ideally, the flow to be considered is caused by monodisperse spherical particles moving with finite relative velocities with respect to a liquid that is stagnant in the mean (or has a constant mean translational velocity that can be removed from consideration by a Galilean transformation). As noted earlier, however, the present flows do not completely satisfy an assumption of monodisperse particles (and neither will most practical flows). Therefore, the analysis eventually will consider a population of particles described by a probability density function of size but will be formulated first for a particular size.

In the present case, particle motion is maintained by the force of gravity, which causes the particles to settle. However, the analysis is also pertinent to any flow where particles are moving relative to the fluid. This may be caused either by their inertia or by some type of force field. The flow is assumed to be statistically stationary, i.e., time-averaged quantities are constant. The time-averaged particle flux across a plane normal to the streamwise direction is assumed to be uniform, while the physical properties of the fluid are constant; therefore, the flow is homogeneous. Batchelor's (1972) study demonstrates that it is impossible to treat the essential randomness of flows of this type rather than prescribe some sort of fixed array, and this suggestion will be followed. Particle arrival times at a point are assumed to be random and independent, i.e., the probability that a particle will arrive at an increment of area within a particular increment of

time is independent of earlier or subsequent particle arrivals. In this circumstance, particle arrival times satisfy Poisson statistics (Rice, 1954). Finally, the flow will be considered to be infinite in extent, since test results to be described later showed little effect of the volume of the bath on the properties of the flow.

Similar to present experimental conditions, the properties of the continuous phase will be found assuming a dilute particle-laden flow. This may seem restrictive with respect to eventual applications involving dense sprays. However, results considered earlier concerning the structure of dense pressure-atomized sprays show that drop-containing regions in these flows are actually quite dilute at each instant—even when the time-averaged liquid volume fraction is large. For dilute dispersed flows, the volume fraction of the dispersed phase is small, and the probability of a particular test point being within a particle is negligibly small, so that such conditions will be ignored.

Similar to the near-field region of a turbulence-generating grid, we assume that flow properties are controlled by the flow field around the particles, including their wakes. Unlike a turbulence-generating grid, however, the particles are widely-spaced in comparison to their dimensions, so that strong interactions between adjacent wakes do not immediately occur, i.e., individual particle wakes remain identifiable for some distance before eventually losing their character through interactions with other nearby wakes. Thus, the flow field associated with each particle is approximated as follows: the near-field flow around a particle is taken to be the potential flow around a sphere, since the probability of a point of observation (a test point) being in the strongly viscous region near the surface of a particle is small in dilute flows; in addition to the potential flow field, the particle wake is considered using asymptotic wake properties. For the potential and asymptotic wake flows, the equations of motion are linear. Therefore, we can also assume that the flow properties are the result of a linear superposition of the properties of the wakes and the potential flow around the particles that have passed through a plane normal to the streamwise direction containing the point of observation.

Formulation. Under present assumptions, the method of summing flow properties involves extension of methods used to analyze random noise in cases where effects of noise can be added linearly (Rice, 1954). Let the point of observation be the origin of a cylindrical coordinate system with x denoting the streamwise direction (positive in the direction of mean particle motion), and r and ϕ denoting the radial and azimuthal coordinates in a plane normal to the main direction of particle motion. Suppose that the arrival of a particle at $x=0$, r_j , ϕ_j and $t=0$ produces an effect $g(r_j, \phi_j, t)$ at the point of observation. Then if the effect of each particle can be added linearly, the total effect at time t at the point of observation, due to all particles is

$$G(t) = \sum_{j=0}^{\infty} \sum_{k=-\infty}^{\infty} g(r_j, \phi_j, t - t_{jk}), \quad (3.12)$$

where the position vectors (r_j, ϕ_j) are chosen to collect all particles; the k^{th} particle at position r_j, ϕ_j arrives at $x=0$ at t_{jk} ; and the series is assumed to converge.

Following Rice (1954), Campbell's theorem can be extended to treat random arrivals of particles over a plane to yield the time-averaged value of $g(t)$ as follows:

$$\bar{G} = \bar{n}'' \int_{-\infty}^{\infty} dt \int_0^{2\pi} d\phi \int_0^{\infty} g(r, \phi, t) r dr, \quad (3.13)$$

while the mean square fluctuation about the average becomes:

$$\bar{G}'^2 = \dot{n}'' \int_{-\infty}^{\infty} dt \int_0^{2\pi} d\phi \int_0^{\infty} g^2(r, \phi, t) r dr \quad (3.14)$$

where \dot{n}'' is the average number of particles arriving at $x=0$ per unit area and time. Rice (1954) also shows that the probability density function of G approaches a normal distribution as $\dot{n}'' \rightarrow \infty$. For finite \dot{n}'' , the error in approximating the probability density function by the normal distribution is on the order of $\bar{G}^3/(\bar{G}'^2)^2 \sim \dot{n}''^{-1}$, which is small for present test conditions.

Temporal correlations and spectra and spatial correlations are also of interest, since these properties influence the turbulent dispersion of particles. Proceeding according to Rice (1954), the temporal correlation of G' is given by

$$\overline{G'(t) G'(t+\tau)} = \dot{n}'' \int_{-\infty}^{\infty} dt \int_0^{2\pi} d\phi \int_0^{\infty} g(r, \phi, t) g(r, \phi, t+\tau) r dr \quad (3.15)$$

The temporal spectrum is obtained from the Fourier transform of equation (3.15) as follows:

$$E_G(f) = 4 \int_0^{\infty} \overline{G'(t) G'(t+\tau)} \cos(2\pi f \tau) d\tau \quad (3.16)$$

Similarly, the spatial correlation of G' in the cross-stream (y) direction is

$$\overline{G'(Y) G'(Y+y)} = \dot{n}'' \int_{-\infty}^{\infty} dt \int_{-\infty}^{\infty} dZ \int_{-\infty}^{\infty} g(Y, Z, t) g(Y+y, Z, t) dY \quad (3.17)$$

Since the particles are moving at their terminal velocities in the region under consideration, the spatial correlation of G' in the streamwise direction is the same as the temporal correlation of G' with the delay time τ converted into separation distance x using $x = U_\infty \tau$. This involves the assumption that the particle wake is aligned with the x direction and not deflected significantly by the turbulence field. Discussion of this approximation will be taken up later.

The above expressions are valid if the effect $g(r, \phi, t)$ can be described in a deterministic way, i.e., they only result from mean velocities in the flow associated with a particle. However, wake Reynolds numbers for present conditions exceed unity, and effects of turbulence can be important (Tennekes & Lumley, 1972). When fluctuations, $g'(r, \phi, t)$, are superimposed on the deterministic effect in a random fashion, e.g., velocity fluctuations in a turbulent particle wake, then equations (3.13)-(3.17) are modified as follows:

$$\bar{G} = \dot{n}'' \int_{-\infty}^{\infty} dt \int_0^{2\pi} d\phi \int_0^{\infty} g(r, \phi, t) r dr \quad (3.18)$$

$$\overline{G'^2} = \dot{n}'' \int_{-\infty}^{\infty} dt \int_0^{2\pi} d\phi \int_0^{\infty} [g^2(r, \phi, t) + g'^2(r, \phi, t)] r dr \quad (3.19)$$

$$\overline{G'(t)G'(t+\tau)} = \dot{n}'' \int_{-\infty}^{\infty} dt \int_0^{2\pi} d\phi \int_0^{\infty} [g(r, \phi, t)g(r, \phi, t+\tau) + g'(r, \phi, t)g'(r, \phi, t+\tau)] r dr \quad (3.20)$$

$$E_G(f) = 4 \int_0^{\infty} \overline{G'(t)G'(t+\tau)} \cos(2\pi ft) dt \quad (3.21)$$

and

$$\begin{aligned} \overline{G'(Y)G'(Y+y)} &= \dot{n}'' \int_{-\infty}^{\infty} dt \int_{-\infty}^{\infty} dZ \int_{-\infty}^{\infty} [g(Y, Z, t)g(Y+y, Z, t) \\ &\quad + g'(Y, Z, t)g'(Y+y, Z, t)] dY \end{aligned} \quad (3.22)$$

$$\overline{G'(X)G'(X+x)} = \overline{G'(U_{\infty}t)G'(U_{\infty}(t+\tau))} \quad (3.23)$$

Several properties of the flow can be inferred immediately from equations (3.18)-(3.23) before specifying specific wake properties and completing the integrations. In particular, since $\varepsilon \sim n''$ from equation (3.5), effects of dissipation can be summarized as follows: velocity fluctuations are proportional to $\varepsilon^{1/2}$; correlations and temporal spectra are proportional to ε ; and correlation coefficients, normalized temporal spectra and ratios of velocity fluctuations are independent of ε . Finally, as noted earlier, the probability density functions of velocity fluctuations should be Gaussian functions for present test conditions.

The preceding equations are limited to a monodisperse flow of particles. However, extension to polydisperse distributions of particles is straightforward. If $\phi(d_p)$ is a generic property for a particular particle diameter (like a variance of a velocity fluctuation, correlation, 'c.), then the property averaged over different particle diameters, for conditions where linear superposition holds, simply involves a summation of the properties of each size, as follows:

$$\phi_{av} = \int_0^{\infty} \phi(d_p) P(d_p) dd_p, \quad (3.24)$$

where $P(d_p)$ is the probability density function of d_p , i.e., the measured size distribution of the particles.

Particle Flow Field. In order to calculate the properties of the continuous phase using equations (3.18)-(3.24), the velocity field associated with an individual particle must be specified. This involves the potential flow field around the particle, as well as the particle wake. As noted earlier, particle Reynolds numbers are greater than unity, so that effects of turbulent particle wakes must be considered. Parthasarathy (1989) presents the formulation for laminar wakes.

The general configuration of the particle flow field is illustrated in Fig. 24. It consists of two separate regions: the potential flow field and the wake. Furthermore, from equations (3.18)-(3.22), it is evident that the mean and turbulent contributions of the wake can simply be summed. Thus, there are three components of each property that can be evaluated separately: (1) the potential flow, (2) the mean properties of the wake, and (3) the turbulent properties of the wake. Thus, for example, equation (3.19) becomes:

$$\bar{G}'^2 = \bar{G}_{pc}'^2 + \bar{G}_{mw}'^2 + \bar{G}_{tw}'^2 \quad (3.25)$$

Evaluation of these components for various properties of the continuous phase is discussed in the following.

Potential flow properties were evaluated assuming that effects of velocity fluctuations in the flow experienced by the sphere could be ignored. This is reasonable, since the particles are small in comparison to measured integral length scales of the flow. For a sphere moving in stagnant fluid, the potential flow velocities are given by the following expressions (Batchelor, 1973):

$$u = (U_\infty d_p^3 / 16 r_0^3)(1 + x^2/r_0^2) \quad (3.26)$$

$$v = (U_\infty d_p^3 x / 16 r_0^4)(1 - x^2/r_0^2)^{1/2}. \quad (3.27)$$

The center of the sphere is taken as the instantaneous origin, r_0 is the distance of the point of observation from the center of the sphere, and x is the streamwise distance from the center of the sphere. To convert the above expressions for a coordinate system whose origin is fixed at a point of observation, we use the following transformations:

$$x = U_\infty t \quad (3.28)$$

$$\text{and} \quad r_0^2 = U_\infty^2 t^2 + r^2. \quad (3.29)$$

Various properties of interest are then calculated for the potential flow region using equations (3.26) - (3.29) in equations (3.18)-(3.23). It was found from equations (3.26) and (3.27) that the velocities decay rapidly with increasing distance from the sphere and are practically zero at $r_0 = 2d_p$. Therefore, the potential flow calculations were terminated at $r_0 = 2d_p$, and wake properties were used beyond this point. Expressions for the mean-square velocity fluctuations of the potential flow region found in this manner are as follows:

$$\bar{u}_{pc}'^2 = 0.019 \epsilon d_p^3 / (U_\infty \theta^2) \quad (3.30)$$

$$\bar{v}_{pc}'^2 = 0.003 \epsilon d_p^3 / (U_\infty \theta^2), \quad (3.31)$$

where

$$\theta = (C_D d_p^2 / 8)^{1/2}. \quad (3.32)$$

The value of C_D can be found from the corrected standard drag coefficient correlation of equation (3.1).

The contributions of the potential flow region to velocity fluctuations, given by equations (3.30)-(3.31), were significantly lower (less than 10%) than the contributions from the wakes. The reason for this is that the effect of the potential flow region involves a

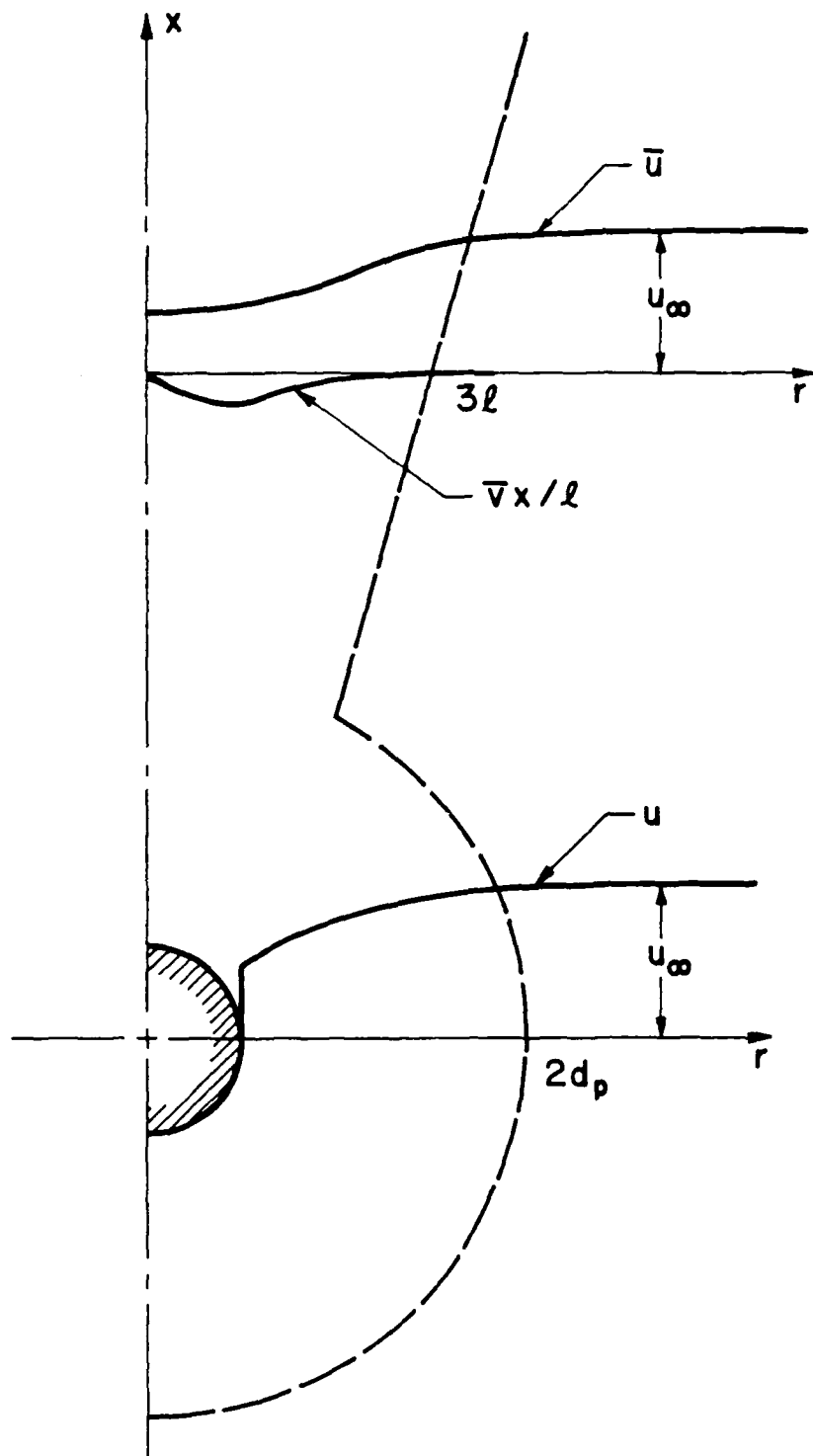


Figure 24 Individual particle flow field.

much smaller volume than the wake, i.e., the probability of a test point being within the potential core is relatively small, since the flows are dilute. The contribution of the potential flow region to velocity fluctuations were considered using equations (3.30) and (3.31). However, since these contributions were small, they were ignored when computing other properties of the continuous phase.

Specifying a representative wake is complicated by turbulent dispersion and self-induced motion of the particles, as well as the turbulence of the flow field itself, since these effects deflect and distort particle wakes from known properties found with rigidly-mounted spheres in non-turbulent environments. To address these features would require very intensive numerical calculations, analogous to exact numerical simulation of the flow. As noted earlier, this is not feasible at present. Therefore, the present analysis was limited to a description of wake properties in the absence of self-induced particle motion for particle volume fractions approaching zero. For these conditions, turbulent dispersion is negligible, and the continuous-phase turbulence field is weak. Therefore, the particles and their wakes remain aligned along a straight vertical path, and wake properties are the same as for results found using rigidly-mounted spheres in a non-turbulent ambient flow. At this limit, the mean downflow velocity due to particle motion is negligible so that velocities in the flow outside the wake are negligibly small as well.

The Reynolds numbers of axisymmetric wakes are initially comparable to particle Reynolds numbers but progressively decrease with increasing distance from the particle. In addition, wakes become laminar for wake Reynolds numbers on the order of unity (Tennekes & Lumley, 1972). All particle Reynolds numbers for present tests are greater than unity. Therefore, the properties of both laminar and turbulent wakes are needed to specify $g(r,\phi,t)$ in equations (3.19) - (3.23). Consideration of laminar wakes can be found in Parthasarathy (1989). The following will focus on the mean properties of turbulent wakes.

Mean velocity distributions in a turbulent wake were derived from results appearing in Tennekes & Lumley (1972) as follows:

$$\bar{u}/U_\infty = 2.23(U_\infty t/\theta)^{-2/3} \exp\{-r^2/2\varrho^2\} \quad (3.33)$$

and

$$\bar{v}/U_\infty = 0.74 \theta^{2/3} r (U_\infty t)^{-5/3} \exp\{-r^2/2\varrho^2\}, \quad (3.34)$$

where θ is the initial momentum diameter of the flow, defined in equation (3.32) and

$$\varrho = 0.47(U_\infty t \theta^2)^{1/3} \quad (3.35)$$

is the characteristic diameter of the wake at downstream positions. The streamwise displacement of the particle relative to the virtual origin of the wake is given by equation (3.28). Finally, the local wake Reynolds number at time t is:

$$Re_\varrho = u_c \varrho / v = (U_\infty \theta / v) (U_\infty t / \theta)^{-1/3}. \quad (3.36)$$

Equation (3.36) shows the progressive reduction of wake Reynolds number with increasing time after passage of the particle, eventually reaching laminar wake conditions.

Equations (3.33)-(3.36) are based on crude concepts of a constant eddy viscosity. Nevertheless, the results provide a reasonable correlation of existing measurements in a convenient analytical form (Uberoi & Freymuth, 1970). The values of \bar{u} and \bar{v} given by equations (3.33) and (3.34) become unbounded at small t , since the equations only represent asymptotic wake properties. As a practical matter, however, computations for wake properties only involved $t > T_0$, where

$$T_0 = 2 d_p / U_\infty \quad (3.37)$$

represents the end of the potential flow region, as illustrated in Fig. 24, and $\bar{u}_c (T_0) < U_\infty$.

Inserting the mean wake properties of equations (3.33)-(3.36) into equations (3.19)-(3.23) indicated that the integrals did not converge as $t \rightarrow \infty$. A similar problem is encountered for laminar wake properties. Therefore, transition to a laminar wake does not resolve the difficulty of diverging integrals at large time. This problem appears to be analogous to limit problems encountered for Stokes flow around particles, using similar methods, for analysis of sedimentation (Batchelor, 1972). Resolving the limit problem for sedimentation proved to be a substantial task that benefitted from accurate knowledge of the flow field for Stokes flow. This is not the case for turbulent wakes, where equations (3.33)-(3.35) were developed from empirical information over relatively narrow ranges of test conditions. Furthermore, the relevance of far-field wake properties in the present application is questionable, due to effects of dispersion of the wake by the existing turbulence field, as noted earlier. Thus, for the present, results are derived for a finite upper limit of integration, T_∞ , which was specified later in order to fit predicted and measured velocity fluctuations in the flow.

Completing integration of equations (3.19)-(3.23) yields the following properties of the continuous phase, based on the mean properties of the turbulent wake:

$$\overline{u_{mw}^2} = 3.34 \epsilon (\theta^2 T_\infty / U_\infty^2)^{1/3} \quad (3.38)$$

$$\overline{v_{mw}^2} = 0.014 \epsilon \theta^2 (T_\infty - T_0) / (T_0 T_\infty U_\infty^2) \quad (3.39)$$

$$\overline{u'v'}_{mw} = 0 \quad (3.40)$$

$$\overline{u'(t)u'(t+\tau)}_{mw} = 2.23 \epsilon (\theta / U_\infty)^{2/3} \int_{T_0}^{T_\infty} (t^{2/3} + (t+\tau)^{2/3})^{-1} dt \quad (3.41)$$

$$\overline{v'(t)v'(t+\tau)}_{mw} = 0.056 \epsilon (\theta / U_\infty)^2 \int_{T_0}^{T_\infty} (t(t+\tau)^{-1/3}(t^{2/3} + (t+\tau)^{2/3})^{-2} dt \quad (3.42)$$

$$\overline{u'(Y)u'(Y+y)}_{mw} = 1.11 \epsilon (\theta / U_\infty)^2 \int_{T_0}^{T_\infty} t^{-2/3} \exp\{-1.11 y^2 (U_\infty t \theta^2)^{-2/3}\} dt, \quad (3.43)$$

where the integrals remaining in equations (3.41)-(3.43) must be found numerically once T_∞ is selected.

Turbulence intensities of turbulent wakes are large even near the axis of the wake. Therefore, it is necessary to consider the contribution of wake turbulence. The wake turbulence properties used during the present calculations were obtained from the study of Uberoi & Freymuth (1970). They measured velocities and spectra in the wake of a sphere for Reynolds numbers between 4000 and 150,000. The present Reynolds numbers varied between 50 and 500. Due to the absence of turbulence measurements in wakes of spheres at present Reynolds numbers, however, the results of Uberoi & Freymuth (1970) were still used for lack of an alternative. Thus, the theoretical results can be thought of as an upper bound for the wake turbulence effects on various properties.

Based on numerical integration of the measurements of Uberoi & Freymuth (1970), we immediately get the following relationships between mean and fluctuating velocities in the wakes:

$$\int_0^{\infty} \bar{u}'^2 r dr = 1.50 \int_0^{\infty} \bar{u}^2 r dr \quad (3.44)$$

and

$$\int_0^{\infty} \bar{v}'^2 r dr = 1.15 \int_0^{\infty} \bar{v}^2 r dr. \quad (3.45)$$

Equations (3.44) and (3.45) indicate that the contribution of velocity fluctuations in the wakes to liquid-phase velocity fluctuations is actually larger than the contribution of the mean streamwise velocity of the wakes. This comes about due to the high turbulence intensities of turbulent wakes even near the centerline, as well as significant contributions of fluctuations away from the centerline. The uncertainties of the measurements are unknown. However, the results were used, since no other complete set of measurements of turbulence properties in axisymmetric wakes has been reported. Based on equations (3.44) and (3.45), the turbulent wake contribution to velocity fluctuations in the continuous phase is as follows:

$$\overline{u'_{tw}^2} = 5.05 \epsilon (\theta^2 T_{\infty} / U_{\infty}^2)^{1/3} \quad (3.46)$$

and

$$\overline{v'_{tw}^2} = 3.81 \epsilon (\theta^2 T_{\infty} / U_{\infty}^2)^{1/3}. \quad (3.47)$$

Furthermore,

$$\overline{u'v'_{tw}} = 0. \quad (3.48)$$

Uberoi & Freymuth (1970) found that the spectra at various points in the wake are identical at low frequencies when normalized by characteristic integral scales and are identical at high frequencies when normalized by the Kolmogorov scales. These spectra were integrated in terms of normalized variables and then matched at the intermediate frequencies, where the low and high frequency estimates intersect one another. This gives the following distribution of the temporal spectrum:

$$\begin{aligned} E_{u_{tw}} / \bar{u'^2}_{tw} (\text{Hz}) &= 0.0036 & 0 < f < 230 \\ &= 1.04 \times 10^6 f^{-3.59}, & 230 < f < 2000 \end{aligned} \quad (3.49)$$

with f in Hz. The same form was used for the temporal spectrum of v' , since its spectra were virtually identical to v' . The temporal spectra for wake turbulence were calculated in the following manner. First, the temporal correlations and spectra based on mean properties were calculated using equations (3.41) and (3.42). The turbulent contributions from equation (3.49) were then added to the temporal spectra to give the total spectra, and these were Fourier transformed to get temporal correlations.

Calculation of the spatial correlation $\bar{u'(Y)u'(Y+y)}$ requires lateral spatial correlation measurements in a turbulent axisymmetric wake. No such measurements have been reported in literature. Hence, these correlations were calculated only based on mean properties. The spatial correlation, $\bar{u'(x)u'(X+x)}$, is the same as the temporal correlation $\bar{u'(t)u'(t+\tau)}$, with $\tau = x/U_\infty$. Thus, this can be obtained from the temporal correlation calculation, considering wake turbulence as described above.

3.3.2 Dispersed Phase

Particle Motion. The properties of the particle phase involve computations of particle motion in the innately random velocity field of the continuous phase and are analogous to random-walk computations. Computations were completed for a sufficient number of particle trajectories, or a sufficiently long trajectory of a single particle, in order to obtain statistically-significant results.

Consistent with the continuous-phase analysis, particle volume fractions are assumed to be infinitely small. Therefore, particle collisions and effects of adjacent particles on particle transport properties are negligible. Particles are also assumed to be small in comparison to the smallest scales of the turbulence field. This is not true, since Kolmogorov length scales are on the order of 250 μm , while particle diameters are 500-2000 μm . Measurements of continuous-phase velocity spectra, however, suggest that the flow does not contain much energy at these small scales, although potential for the smallest scales to modify particle drag properties should be examined in the future. The particles are assumed to be monodisperse and spherical, which are generally conditions of the experiments. Finally, Magnus and Saffman lift forces and static pressure gradients can be ignored with little error (Faeth 1977, 1983, 1988).

Under these assumptions, particle motion can be found using the formulation of Odar & Hamilton (1964), reviewed by Clift et al. (1978), as follows:

$$d x_{pi} / dt = u_{pi} \quad (3.50)$$

$$(\rho_p / \rho + \Delta_A / 2) d u_{ri} / dt = a(\rho_p / \rho - 1) \delta_{li} - 3C_D |u_r| u_{ri} / (4d_p)$$

$$- \Delta_H (81 v / \pi d_p^2)^{1/2} \int_{t_0}^t (t-\xi)^{-1/2} (d u_{ri} / d\xi) d\xi, \quad (3.51)$$

where a Cartesian reference frame has been used with $i=1$ denoting the vertical direction. The terms of the left-hand side of equation (3.51) represent acceleration due to particle and

virtual mass, while the terms on the right-hand side represent buoyancy, drag and Basset-history forces.

The parameters Δ_A and Δ_H account for effects of particle acceleration on the virtual mass and Basset-history forces. They were empirically correlated by Odar & Hamilton (1964), as follows:

$$\Delta_A = 2.1 - 0.123 M_A^2 / (1 + 0.12 M_A^2) \quad (3.52)$$

$$\Delta_H = 0.48 + 0.52 M_A^3 / (1 + M_A)^3 \quad (3.53)$$

where M_A is the particle acceleration modulus

$$M_A = (d u_r / dt) d_p / u_r^2. \quad (3.54)$$

The values of Δ_A and Δ_H vary in the ranges 1.0-2.1 and 1.00-0.48, the former values being the correct limit for the Basset-Boussinesq-Oseen (B-B-O) formulation of equation (3.51) (Clift et al. 1978). Particle Reynolds numbers based on the relative velocity of the particle and fluid did not reach the supercritical flow regime. Therefore, the standard drag coefficient for solid spheres was approximated as earlier, see equation (3.1). For present test conditions, liquid velocity fluctuations are small in comparison to the relative velocity of the particles. Therefore, the high relative turbulence intensity drag expressions used by Parthasarathy & Faeth (1987) are not needed. The actual terminal velocities were measured, and the above drag expression was modified to match the measurements, as discussed earlier. The sensitivity of the calculations to C_D , Δ_A and Δ_H was also evaluated.

Statistical Simulation. Statistical simulation of particle trajectories was based on methods used to predict turbulence/radiation interactions developed by Kounalakis et al. (1988) according to formal statistical time series simulation techniques adapted from Box & Jenkins (1976). The statistical simulation of the velocity field of the continuous phase can be carried out to satisfy any number of the statistical properties of the continuous phase: mean velocities, velocity fluctuations, Lagrangian time correlations, instantaneous conservation of mass, higher-order correlations, etc. However, computational requirements increase as the number of properties of the flow to be simulated increase, and priorities must be set. Based on findings using earlier methods of statistical simulation (Faeth 1983, 1987), mean and fluctuating velocities and Lagrangian time correlations appear to be sufficient to treat turbulent particle dispersion. Therefore, present simulations are designed to reproduce these properties.

The present flows are homogeneous, and mean velocities and cross-correlations like $\bar{u}'\bar{v}'$ are small. Therefore, only velocity fluctuations must be simulated, and velocity components can be assumed to be statistically independent. However, velocity fluctuations are not isotropic (see Table 4). Streamwise velocity fluctuations are larger than cross-stream velocity fluctuations (naturally, both components of the latter are equal). Finally, measurements have shown that the velocity fluctuations have Gaussian probability density functions, in agreement with results of the analysis of the liquid phase.

To illustrate the approach used to satisfy correlations, consider a simulation using equal time steps that has proceeded $i-1 > p > 0$ time steps. The value of any component of the continuous phase velocity fluctuations at the location of the particle at the end of the next time step, say u_i' (where u can be any velocity component and i denotes the time step) is found from the following autoregressive process (Box & Jenkins, 1976):

$$u_i' = \sum_{j=p}^{i-1} A_{ij} u_j' + a_i; \quad 1 \leq p \leq i-1, \quad (3.55)$$

where the A_{ij} are weighting factors so that correlations between various points can be satisfied; a_i is an uncorrelated random variable chosen to satisfy the probability density function of u_i' ; and p is selected to eliminate points having small correlation coefficients with respect to the point i . The A_{ij} are related to the correlations through the Yule-Walker equations, as follows (Box & Jenkins, 1976):

$$\overline{u_i' u_k'} = \sum_{j=p}^{i-1} A_{ij} \overline{u_j' u_k'}; \quad k=p, \dots, i-1. \quad (3.56)$$

The first moment of a_i is zero, while the second moment is found from the following expression:

$$\overline{a_i^2} = \overline{u_i'^2} - \sum_{j=p}^{i-1} A_{ij} \overline{u_j' u_i'}. \quad (3.57)$$

Given the correlations, equations (3.56) form a positive-definite linear system of equations that can be efficiently solved using Cholesky factorization. The $\overline{a_i^2}$ can then be found from equation (3.57), since all quantities of the RHS of this equation are known.

The simulation is particularly simple when the correlations are exponential. Box & Jenkins (1976) have shown that equation (3.55) can be reduced so that only a single previous time step must be considered to generate u_i' for the next time step as follows:

$$u_i' = A_{i-1} u_{i-1}' + a_i, \quad (3.58)$$

where A_{i-1} is the correlation between u_i' and u_{i-1}' . a_i is obtained from a Gaussian distribution with a zero mean value and a variance as follows:

$$\overline{a_i^2} = (1 - A_{i-1}) \overline{u_i'^2}. \quad (3.59)$$

Thus, only the values of velocity at the previous time-step are needed to find velocities at the next time step, substantially simplifying the calculations.

The analysis begins with a proper random selection of the components of the velocity fluctuations, u_0' , allowing for the variances and anisotropy. $\overline{a_i^2}$ is then found from equation (3.59). A random selection for a_i is then made from its PDF, so that u_i' can be computed from equation (3.58). After repeating this process to find all three velocity components, the motion of the particle in this velocity field is then computed to find conditions at Δt . This entire process is completed for n particles, where n is large enough to provide statistically-significant results. For the present calculations, $n = 5000$ was satisfactory, with the sizes of the 5000 particles distributed according to the measured particle size variations.

The key to simulating particle trajectories is knowledge of the Lagrangian correlations, A_{i-1} . Fortunately, although Taylor's hypothesis is not appropriate to relate temporal and spatial variations of turbulence properties at a fixed point, since the mean liquid velocity is small, relative velocities of particles are large in comparison to velocity

fluctuations. Therefore, Taylor's hypothesis can be applied to obtain correlations along a particle path. Thus knowledge of spatial and temporal correlations in the streamwise direction allows the A_{ij-1} to be estimated. Since spatial correlations of the cross-stream velocities in the streamwise direction were not measured, they were assumed to vary in the same manner as the spatial correlations of streamwise velocities. The output of the stochastic simulation consists of particle properties like \bar{u}_p , \bar{v}_p , $\bar{u}_p''^2$, $\bar{v}_p''^2$ — the latter being direct measures of particle dispersion.

3.4 Results and Discussion

3.4.1 Apparatus Evaluation

Initial experiments dealt with the operation of the test apparatus. This involved consideration of the uniformity of particle number fluxes, homogeneity of liquid flow properties, effects of wave action at the liquid surface, effects of particle flux disturbances, effects of bath size, and approach to steady-state conditions. Each of these topics is discussed in the following.

The uniformity of particle number fluxes across the bath was a primary consideration, since it determined the homogeneity of the flow. Measurements of particle number fluxes as a function of position for the 1.0 mm diameter particles at three loadings are illustrated in Fig. 25. The low, medium, and high loadings correspond to flows having dissipation rates of 27.3, 68.2, and 155.8 mm^2/s^3 , respectively. These measurements extend to the near-wall region only on one side due to limitations of traversing the Mie-scattering measuring volume. However, it is evident that particle number fluxes are uniform within experimental uncertainties (within $\pm 10\%$) over the middle 300 mm of the bath cross-section. Reduced particle number fluxes in the near-wall region are attributed to the fact that the duct for the particle feed system was 30 mm smaller (in each direction) than the dimensions of the liquid bath. Collection of particles at the bottom of the bath revealed that particle fluxes were uniform in the other direction as well, except within 50 mm of the walls.

The variation of liquid streamwise velocity fluctuations across the bath for the three loadings with the 1.0 mm diameter particles is illustrated in Fig. 26. Open and shaded symbols represent measurements 100 mm above and below the optical plane of the fixed LDA channel. Similar to particle number fluxes, streamwise velocity fluctuations were uniform within experimental uncertainties across the central 300 mm cross-section of the bath. Repeatability of these results was within 10%. The velocity fluctuations measured at different points in the central region of the bath during the spatial correlation measurements at various loadings with the 0.5 and 2.0 mm particles also revealed variations within experimental uncertainties. Thus, the liquid flow properties were homogeneous for all test conditions within experimental uncertainties.

Effects of waves on the liquid surface were investigated by installing a honeycomb at the surface. No change of flow properties was observed when the honeycomb was installed, so that it was removed for operational convenience during subsequent tests. Disturbances of the particle fluxes were examined by blocking portions of the particle flow with strips across the top of the test tank. The effect of such disturbances was also small. Finally, effects of bath size were examined by installing partitions within the test tank and varying the liquid level. The effect of reducing the bath volume by a factor of 32 was on

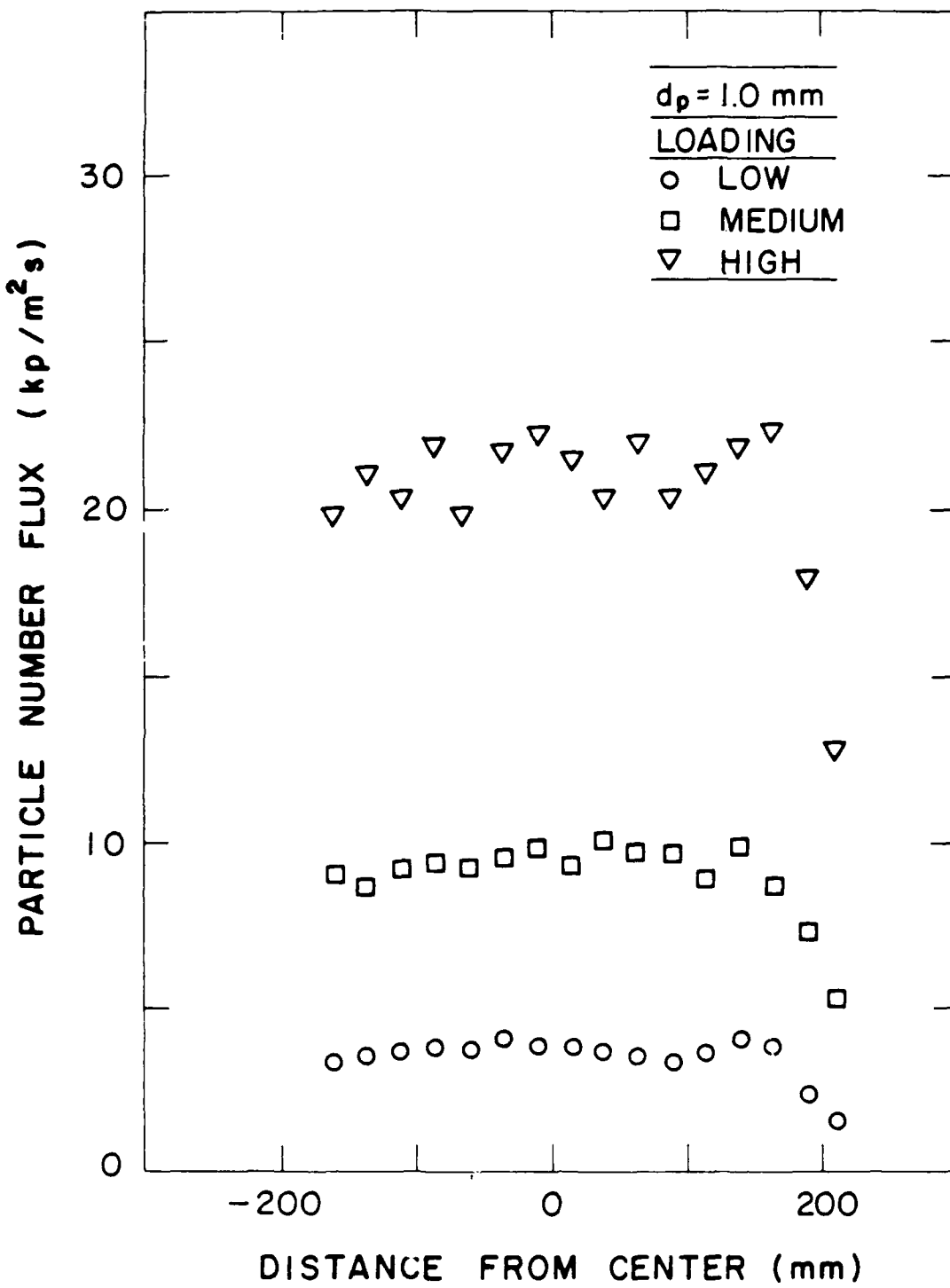


Figure 25. Particle number flux distribution ($d_p = 1.0 \text{ mm}$). The symbol kp denotes 1000 particles.

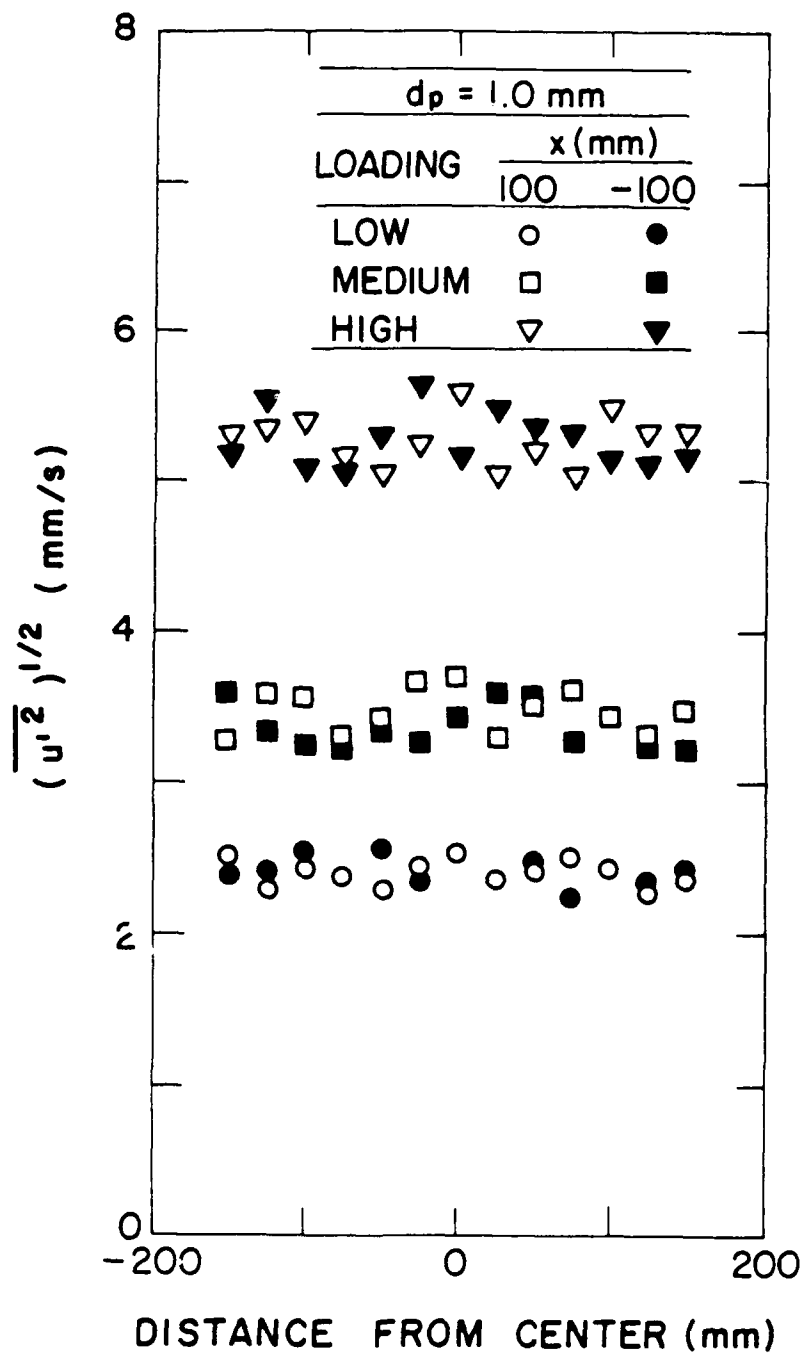


Figure 26 Liquid streamwise velocity fluctuation distribution ($d_p = 1.0$ mm).

the order of 15% for velocity fluctuations, so that the effect of the bath walls is also felt to be small.

The time required for the bath to reach steady-state conditions, after initiation of the particle flow, was also evaluated. It was found that liquid velocity fluctuations reached stationary values within five minutes after the start of the particle feeder with subsequent variations with time within 10% — which is within experimental uncertainties (Parthasarathy, 1989).

3.4.2 Continuous-Phase Properties

Mean Velocities. The lower particle number fluxes near the wall induced a large-scale circulation within the bath, as noted earlier. Thus, results summarized in Table 4 indicate that \bar{u}/\bar{u}' was ca. 0.5 for the lowest loadings of the 0.5 and 1.0 mm diameter particles, while this ratio varied between 0.7 and 1.0 for other test conditions. Mean crossstream liquid velocities were smaller, e.g., \bar{v}/\bar{u}' was less than 0.5 for all test conditions.

Mean liquid velocities in the bath are very small in comparison to particle terminal velocities, and their presence does not affect particle dynamics appreciably. Since the flow is homogeneous and stationary, the mean motion also does not influence velocity fluctuations, cross-correlations at a point, as well as spatial correlations where velocities are measured at two points simultaneously. The presence of a mean velocity, however, does cause a change in temporal spectra measured at a point. Therefore, a correction was applied to these measurements which will be taken up later.

Reynolds stresses. Reynolds stresses, $(\bar{u}'\bar{v}')$, are ideally zero for a homogeneous turbulent flow. This property was measured for the 0.5 mm diameter particles at several loadings, finding that $(\bar{u}'\bar{v}')/(\bar{u}')^2 < 6\%$. Experimental uncertainties were large, ca. 55%, for Reynolds stress measurements due to their small magnitude. Therefore, these values are essentially zero within experimental uncertainties.

Velocity Fluctuations. Measured liquid velocity fluctuations in the streamwise and cross-stream directions are plotted as a function of dissipation in Fig. 27. Results are illustrated for all three particle sizes. While most measurements were limited to the particle number flux conditions summarized in Table 4, a broader range of conditions was considered for the results illustrated in Fig. 27 so that the trends of the measurements with respect to variations of dissipation could be seen more clearly.

The measurements for each component of velocity fluctuation illustrated in Fig. 27 correlate solely as a function of dissipation within experimental uncertainties. Thus, effects of particle number flux variations are represented by the dissipation through equation (3.5), while particle size is a secondary factor with respect to the properties of the liquid phase over the present test range. A possible exception to this trend involves the cross-stream velocity fluctuations for the two highest loadings with the 0.5 mm diameter particles. However, these conditions represent the highest particle number densities that were considered, and the measurements are felt to be less reliable than the other results due to poorer signal-to-noise ratios. Both streamwise and cross-stream velocity fluctuations are proportional to $\epsilon^{1/2}$, which is in accord with the general expectations of the theory as discussed earlier. The streamwise velocity fluctuations are roughly twice as large as the cross-stream velocity fluctuations, which is understandable, since liquid motion is primarily caused by particles moving in the streamwise direction. This high level of

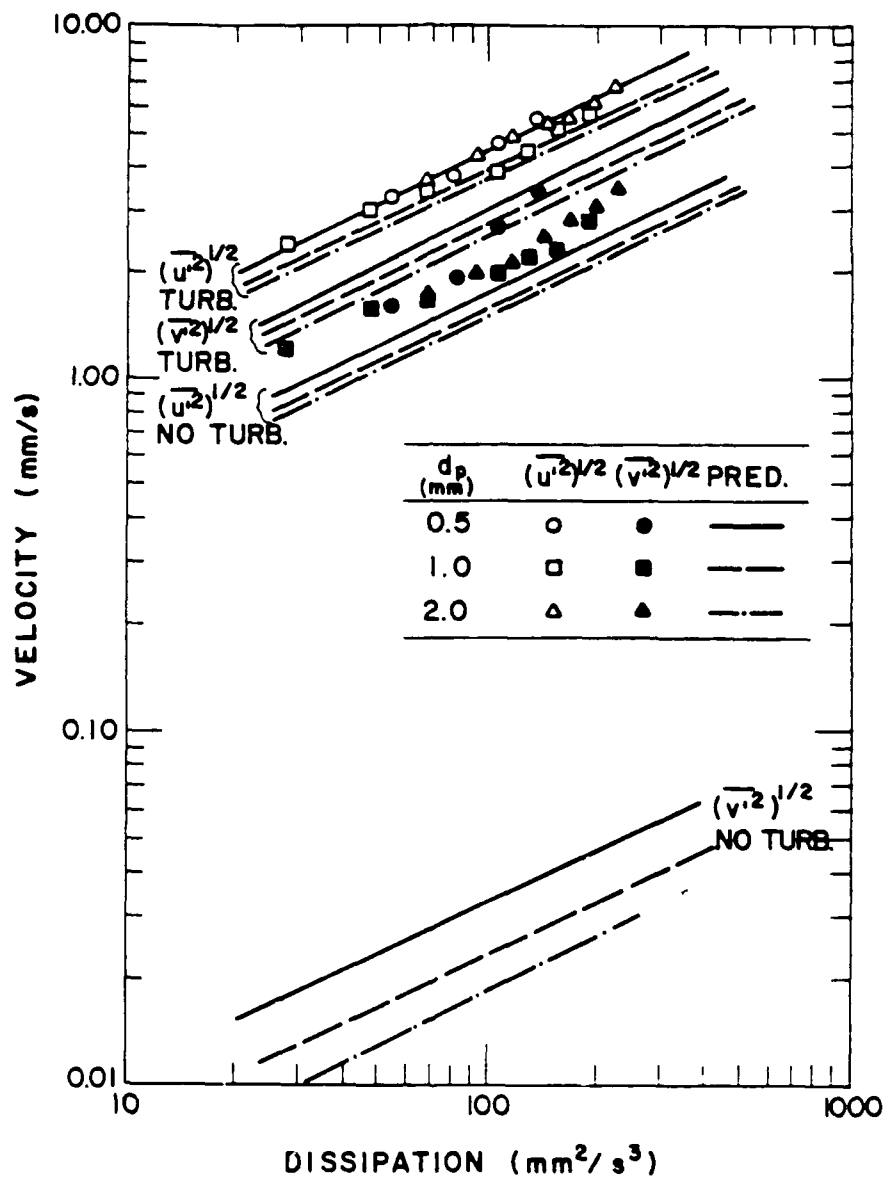


Figure 27 Liquid velocity fluctuations.

anisotropy suggests relatively strong effects of particle wakes. Otherwise, the flow would be more isotropic, analogous to conditions downstream of a turbulence-generating grid.

Two sets of predictions are also illustrated in Fig. 27 for each component of the velocity fluctuations — one set considering only mean properties in turbulent wakes, the other set considering both mean and turbulent properties in the turbulent wakes. These predictions were found by roughly matching predicted streamwise velocity fluctuations, allowing for both mean and turbulent wake properties, with the measurements. This involved terminating the integration of wake properties at $x/d_p = U_\infty T_\infty / d_p = 175$. This choice also seems reasonable on a physical basis. The mean velocity defect of the wake is on the order of 1% of the terminal velocity of the particle at this location, so that it is likely that the coherence of wake properties would be lost in the background turbulence field at larger distances. Thus, in a sense, this location is analogous to the location where the flow becomes nearly isotropic downstream of a turbulence-generating grid.

Basing predictions on $U_\infty T_\infty / d_p = 175$, yields predicted velocity fluctuations (including both mean and fluctuating wake properties) as follows:

$$\overline{u'^2} U_\infty / (\epsilon d_p) = 46.72 (\theta / d_p)^{2/3} \quad (3.60)$$

$$\overline{v'^2} U_\infty / (\epsilon d_p) = 21.49 (\theta / d_p)^{2/3}. \quad (3.61)$$

The form of equations (3.60) and (3.61) suggests a dominant effect of particle diameter, while the actual effect of particle diameter was relatively small over the present test range (see Fig. 27). An equivalent formulation, which is informative, can be obtained by introducing expressions for U_∞ and θ . Present measurements of terminal velocities in the bath, to be discussed later, show that they are essentially the same as terminal velocities in a still environment. Thus, considering the latter condition yields

$$U_\infty = ((4a d_p / 3 C_D)(\rho_p / \rho - 1))^{1/2} \quad (3.62)$$

Substituting equation (3.62) for U_∞ and equation (3.32) for θ into equations (3.60) and (3.61) then yields the following:

$$(\overline{u'^2} / \epsilon) [\frac{a}{d_p} (\frac{\rho_p}{\rho} - 1)]^{1/2} = 20.24 C_D^{5/6} \quad (3.63)$$

and

$$(\overline{v'^2} / \epsilon) [\frac{a}{d_p} (\frac{\rho_p}{\rho} - 1)]^{1/2} = 9.31 C_D^{5/6}. \quad (3.64)$$

Assuming that C_D is a constant, equations (3.63) and (3.64) indicate that velocity fluctuations only vary as $d_p^{1/4}$. For present test conditions, however, the effect of reduced C_D with increasing particle size dominates the $d_p^{1/4}$ term, and the velocity fluctuation estimates of equations (3.63) and (3.64) actually decrease somewhat with increasing particle size — all other factors in the equations being the same.

The correlations of equations (3.63) - (3.64), along with their counterparts where effects of turbulence in the wakes have been ignored, are plotted in Fig. 27. Predictions with and without wake turbulence contributions were considered, since the Reynolds numbers of the present particle wakes were relatively low — much smaller than the wake Reynolds numbers considered by Uberoi & Freymuth (1970) — so that wake turbulence might be poorly developed for present test conditions. The predictions illustrated in Fig. 27 suggest that this is not the case. In particular, predictions of the cross-stream velocity fluctuations are much smaller than the streamwise velocity fluctuations, when the contributions of wake turbulence is ignored. This follows since cross-stream mean velocities are much smaller than streamwise mean velocities in wakes, yielding much higher levels of anisotropy than measured. On the other hand, the ratio of streamwise to cross-stream velocity fluctuations from equations (3.60) and (3.61) is 1.47, which is somewhat less than the ratio of roughly 2 of the measurements. This might be explained by turbulence levels in the particle wakes being somewhat lower than the levels observed by Uberoi & Freymuth (1970), which would not be surprising in view of the much lower Reynolds numbers of the present particle wakes. All things considered, it seems probable that both mean and turbulent properties of the particle wakes contribute to the turbulence field of the continuous phase.

The estimates of velocity fluctuations from equations (3.60) - (3.64) exhibit a slight dependence on particle size over the present test range. However, this variation is not much larger than experimental uncertainties, and a similar trend is not seen in the measurements illustrated in Fig. 27. The degree of development of turbulence in the wake may also be a factor in the reduced sensitivity of measurements to particle size. In particular, predictions suggest lower levels of turbulent fluctuations with increasing particle size, while the larger particles have higher wake Reynolds numbers which should tend to increase wake turbulence levels. Therefore, these two effects tend to compensate one another. Additional measurements of turbulent wake properties are needed for a wider range of test conditions in order to determine whether or not this is the case.

Probability Density Functions. The probability density functions of streamwise and cross-stream velocity fluctuations are plotted as a function of normalized variables in Figs. 28 and 29. Measurements for the different particle sizes and loadings generally fall along a single curve, within experimental uncertainties. Theoretical lines are also illustrated on each plot, based on a Gaussian distribution function, which is expected from the theory. This distribution is in excellent agreement with the measurements. However, this is not a very strong test of theory, since velocity fluctuations of homogeneous turbulent flows exhibit Gaussian distributions more often than not.

Temporal Spectra. The measured temporal power spectral densities of the streamwise and cross-stream velocity fluctuations are plotted as a function of frequency in Figs. 30 and 31. Both the power spectral densities and the frequencies have been normalized by the integral time scales appropriate to the bath conditions of the measurements. Discussion of the integral time scales themselves will be taken up later. The measurements are limited to the lowest loadings with all three particle sizes considered for the streamwise spectra but just the smallest particle size for the cross-stream spectra. This limitation was necessary in order to select conditions that were not unduly influenced by the effect of mean streamwise velocities mentioned earlier.

Before discussing the results of temporal spectral measurements, it is necessary to consider two experimental problems: the effect of mean streamwise velocity and the effect of step noise. When there is a mean streamwise velocity, \bar{u} , for present test conditions, the streamwise temporal correlation measured at a fixed point is $\overline{u'(x-\bar{u}t)u'(x-\bar{u}(t+\tau),y,z,t+\tau)}$.

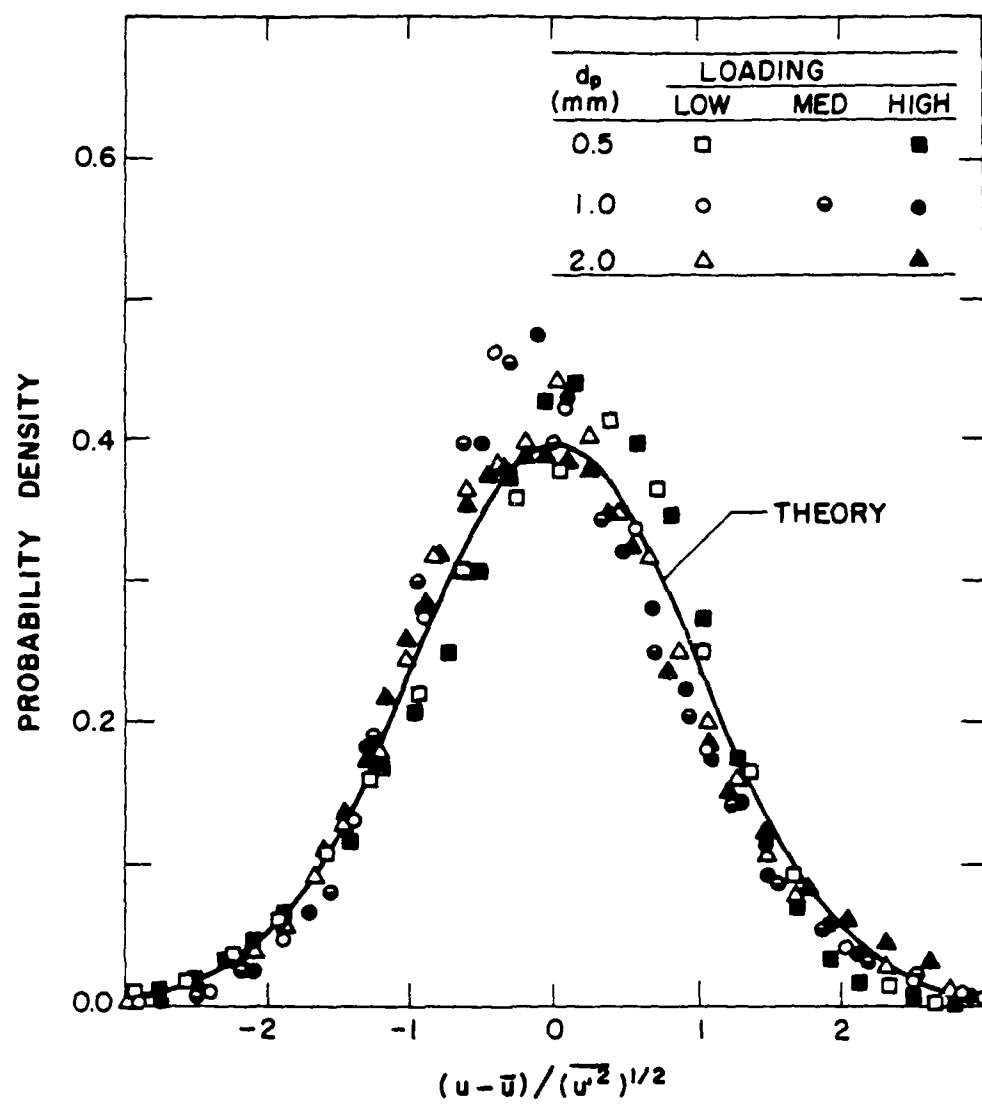


Figure 28 Probability density function of liquid streamwise velocity fluctuations.

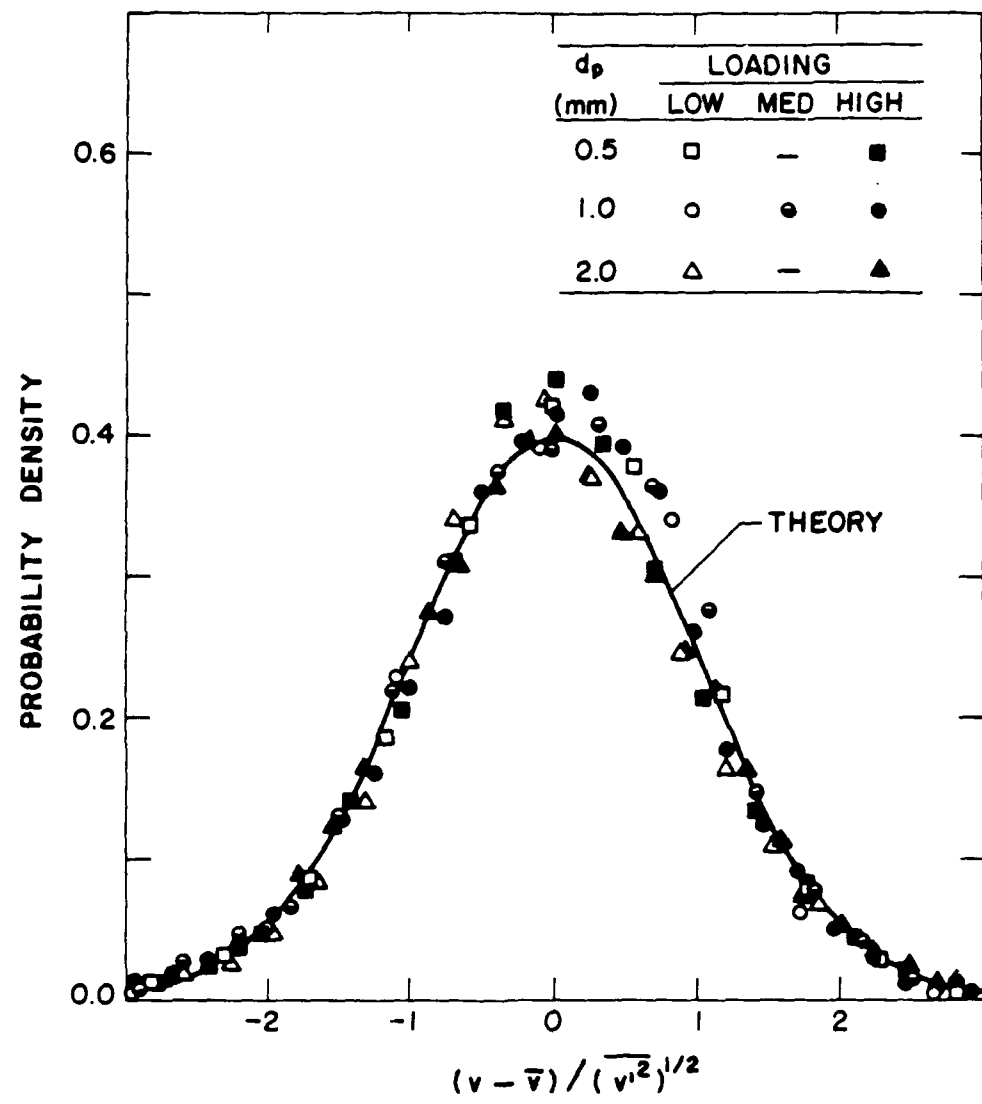


Figure 29 Probability density function of liquid crosstream velocity fluctuations.

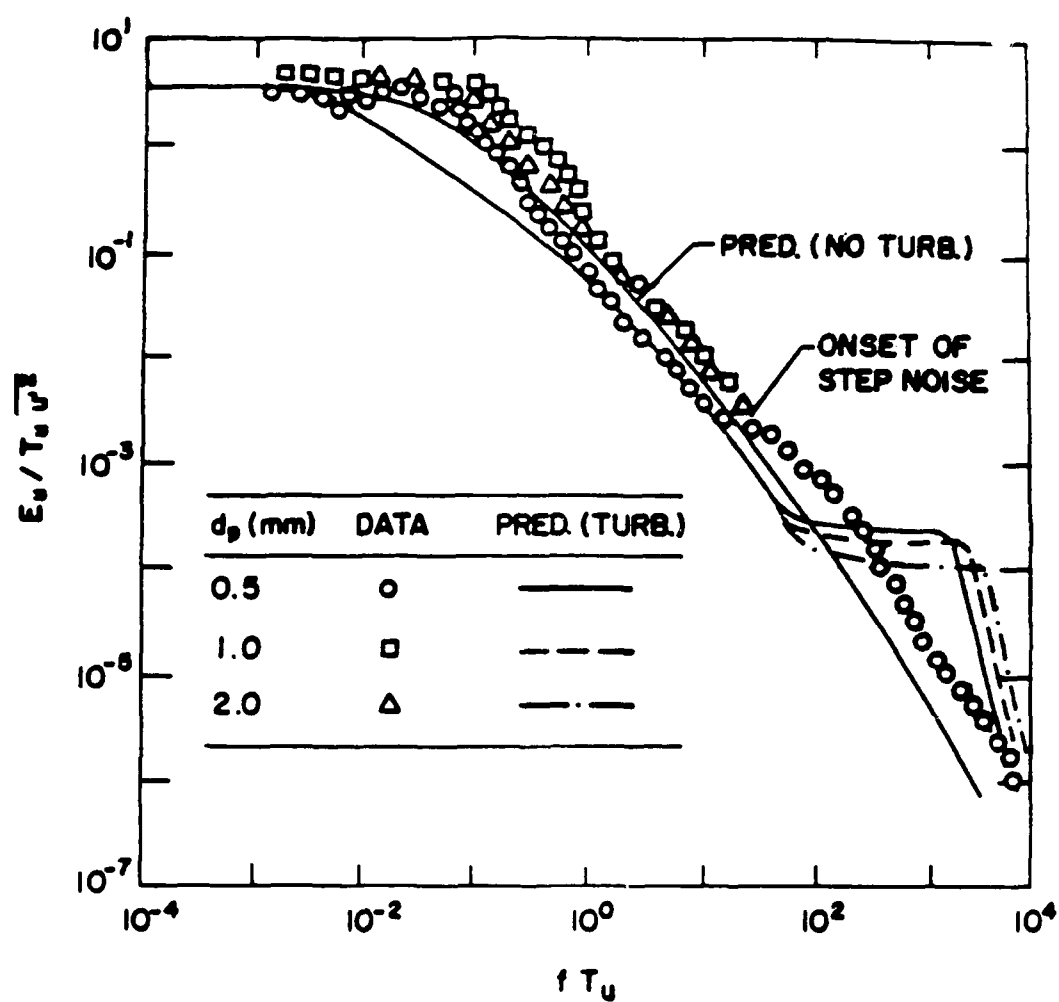


Figure 30 Temporal spectral density of liquid streamwise velocity fluctuations.

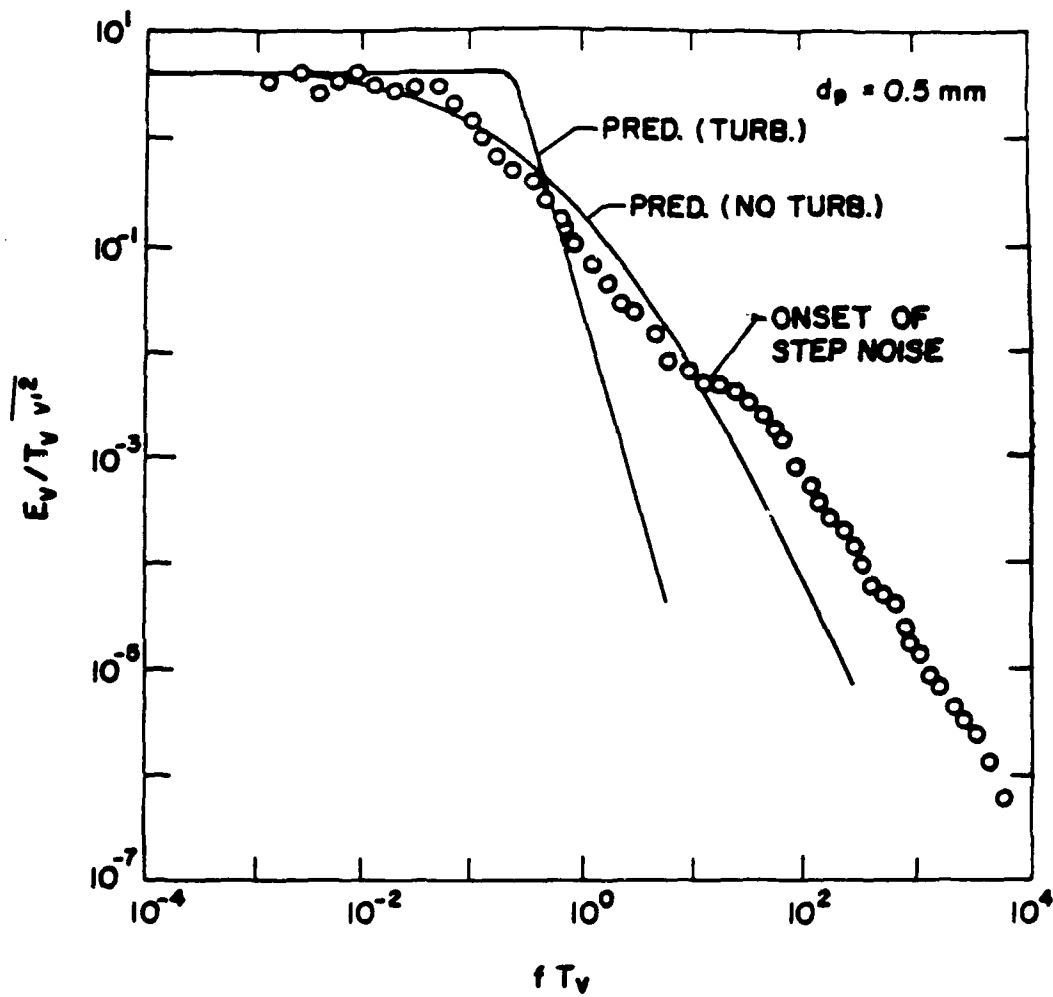


Figure 31 Temporal spectral density of liquid crosstream velocity fluctuations.

which is actually a two-point two-time correlation or a combined spatial and temporal correlation (Hinze, 1975). In contrast, the temporal correlation that is actually being sought is $\overline{u'(x,y,z,t)u'(x,y,z,t+\tau)}$. In order to correct for the effect of the mean velocity it was assumed that the combined correlation could be split into a product of temporal and spatial correlations as follows:

$$\begin{aligned} \overline{u'(x-\bar{u}t,y,z,t)u'(x-\bar{u}(t+\tau),y,z,t+\tau)} &= \overline{u'(x-\bar{u}t,y,z,t)u'(x-\bar{u}(t+\tau),y,z,t)} \\ &\times \overline{u'(x,y,z,t)u'(x,y,z,t+\tau) / u'^2} \end{aligned} \quad (3.65)$$

Equation (3.65) is not rigorously accurate. However, it is a reasonable approximation for a homogeneous turbulent field. Since the measured spatial correlations in the streamwise direction were unaffected by the mean velocity, the spatial correlation $\overline{u'(x-\bar{u}t,y,z,t)u'(x-\bar{u}(t+\tau),y,z,t+\tau)}$ is known from the measurements. Then the desired temporal correlation $\overline{u'(x,y,z,t)u'(x,y,z,t+\tau)}$ could be calculated from equation (3.65). The correction for mean velocities was negligible for the lowest loading of the 0.5 mm diameter particles and was relatively small for the lowest loadings of the other two particle sizes. Therefore, only measurements for these two conditions are plotted in Fig. 30.

In order to apply a similar correction for the presence of mean velocities to the temporal correlation of cross-stream velocity fluctuations, the spatial correlation $\overline{v'(x-\bar{u}t,y,z,t)v'(x-\bar{u}(t+\tau),y,z,t)}$ must be known. Unfortunately, this spatial correlation was not measured. However, since the mean velocity correction was small for the temporal correlation of streamwise velocity fluctuations for the lowest loading with the 0.5 mm diameter particles, it was assumed that the correction would also be small for the temporal correlation of the cross-stream velocity fluctuations at this condition as well — which are the only measurements plotted in Fig. 31.

The second problem is that Fourier transformation of the analog signal of the LDA burst processor introduced "step-noise" caused by the sample-and-hold signals of the processor. Adrian & Yao (1987) have shown that effects of step-noise are observed at frequencies roughly one-tenth of the frequency corresponding to the mean data rate. The characteristics of step-noise are the appearance of noise band having a constant spectral amplitude followed by a second-order low pass filter effect at a slightly higher frequency, i.e., a subsequent decay of the spectra according to f^{-2} . This results in a slight flat spot in the spectra, followed by a region where the spectra decrease according to f^{-2} , which is noted in Figs. 30 and 31 for the measurements with the 0.5 mm diameter particles.

The onset of step-noise for present measurements with the 0.5 mm diameter particles corresponds quite nicely with the estimates of Adrian & Yao (1987). For example, the streamwise spectrum in Fig. 30 exhibits a change in slope (denoted step-noise) at $f\Gamma_u \sim 10$. This frequency roughly corresponds to one-tenth of the mean data rate (2000 Hz). The onset of step-noise appears at a slightly lower frequency for the cross-stream spectrum in Fig. 31. This is consistent with the slightly lower data rate for these measurements. Naturally, the portions of the spectra beyond the onset of step-noise are not representative of flow properties and should be ignored. The region is only illustrated in Figs. 30 and 31 in order to establish that this portion is an artifact of step-noise and not some property of the flow, since original measurements extended into this frequency range.

A correction for step-noise was made at the same time as the mean velocity corrections for the measurements with the 1.0 and 2.0 mm diameter particles. Therefore, the step-noise region is not illustrated for these measurements in Fig. 30. The corrections involved subtracting the step-noise from the spectrum, taking the Fourier transform of the result to obtain the combined temporal and spatial correlation, applying the mean velocity correction to this correlation, and finally taking the Fourier transform of this correlation to obtain the results illustrated in Fig. 30.

The differences between the measurements of the temporal spectra of streamwise velocity fluctuations for the three particle sizes, illustrated in Fig. 30, are within experimental uncertainties. This agrees with the results concerning streamwise velocity fluctuations in Fig. 27 where effects of particle diameter are not very important. In addition to differences of particle sizes, the rate of dissipation also differs for the three conditions illustrated in Fig. 30; however, it was a general conclusion of the theory that temporal correlations should be independent of the rate of dissipation. Based on these findings, the small effect of particle size seen in the spectra of Fig. 30 is quite reasonable.

Perhaps the most surprising feature of the results illustrated in Fig. 30 is the large range of frequencies in the spectrum and the significant levels of signal energy at very low frequencies, even though wake Reynolds numbers are relatively low and the flow field is produced by small particles having relatively small interparticle spacings. In fact, based on theoretical estimates, the measured spectra would have extended over a much larger frequency range if the limitations of step-noise could have been avoided. The reason for the large range of frequencies, as well as the presence of appreciable signal energy at low frequencies, is that the flow field includes contributions from both the mean and turbulent velocity fields of the particle wakes, with the mean velocities enhancing signal energies at low frequencies. Such behavior is not normally observed in turbulent flows generated by other mechanisms. However, the contribution of the mean velocities cannot be separated from the turbulent contributions of the particle wakes in the present flows, since arrival of particles is random.

Since predicted normalized temporal spectra were not sensitive to the selection of T_∞ , a large value was chosen, $x/d_p = U_\infty T_\infty / d_p = 25,000$, to cover the complete normalized frequency range of the figures. The effect of this selection on predictions of integral scales will be taken up later. Predictions of streamwise temporal spectra, considering and ignoring effects of wake turbulence, were independent of dissipation rates, while predictions ignoring wake turbulence were independent of particle diameter as well. However, predictions considering wake turbulence exhibit somewhat different shapes at high frequencies, reflecting effects of different wake Reynolds numbers for different-sized particles.

Both predictions exhibit significant signal energy at low frequencies in Fig. 30, similar to the measurements. This supports the idea that the low-frequency region is caused by mean velocities in the particle wakes, since both predictions include this contribution. The prediction that includes wake turbulence also exhibits enhanced signal energy at high frequencies, where an effect of particle size is also seen due to the variation of wake Reynolds numbers with particle size. Unfortunately, this region could not be observed due to effects of step-noise. The step in the predicted spectra due to wake turbulence is somewhat analogous to the appearance of step-noise in the measured spectra, which initially motivated our concern to establish step-noise properties for our measurements. The agreement between predicted and measured streamwise temporal spectra is reasonable - particularly for the predictions where wake turbulence is ignored. The more rapid decay of the spectra considering wake turbulence at low frequencies is

caused by the presence of larger signal energies at high frequencies due to turbulence. Thus, the poorer agreement of the predictions considering wake turbulence at low frequencies suggests that the turbulence field of the particle wakes may not be developed to the extent observed by Uberoi & Freymuth (1970). This would not be surprising, since the wake Reynolds numbers considered by Uberoi & Freymuth (1970) were much larger than those of present particle wakes.

The measurements of the temporal spectra of the cross-stream velocity fluctuations, illustrated in Fig. 30, are similar to the streamwise temporal spectra. As before, there is significant signal energy at low frequencies and probably a large range of frequencies in the spectra if effects of step-noise had not intruded due to combined contributions of both mean and turbulent properties of particle wakes. Due to the small magnitude of mean radial velocities in comparison to radial velocity fluctuations in wakes, however, the turbulence contributions to the spectra are two orders of magnitude higher than the mean velocity contributions. Therefore, the cross-stream spectra provide a more sensitive indication of wake turbulence effects than the streamwise turbulence spectra - analogous to the relative effect of wake turbulence on cross-stream and streamwise velocity fluctuations that was discussed earlier. Thus, the shapes of the predicted spectra with and without consideration of wake turbulence differ to a greater extent for the cross-stream velocity fluctuations. The measurements in the step-noise free portion of the spectrum lie between the two predictions, which suggests a lower degree of development of wake turbulence than observed by Uberoi & Freymuth (1970) at higher wake Reynolds numbers. While this is plausible, additional measurements of the properties of turbulent wakes behind spheres at moderate Reynolds numbers are needed to resolve the properties of homogeneous particle-laden flows.

Spatial Correlations. The measured spatial correlations of streamwise velocity fluctuations in the cross-stream direction are illustrated in Fig. 32. Measurements at various particle loadings for the three particle sizes are plotted as a function of cross-stream distance normalized by the cross-stream integral length scale. Consideration of the cross-stream integral length scales themselves will be taken up later. These measurements were repeated for both positive and negative separation distances to check the symmetry of the correlations. These results are not illustrated to avoid crowding of the figure. However, they showed that the correlations were symmetric within experimental uncertainties.

The spatial correlation measurements for various loadings and particle sizes are essentially the same. This is consistent with the general conclusion of the theory that correlation coefficients should be independent of the rate of dissipation, and the earlier finding that velocity fluctuations are relatively independent of particle size. The measurements exhibit an exponential-like decay of the correlation with increasing separation distances. This observation is influenced to some extent by experimental problems since effects of step-noise precluded resolving the smallest scales of the flow which would be expected to influence the curvature of the correlation at the smallest separation distances (Hinze, 1975).

Predictions of spatial correlations used the same T_∞ as the temporal spectra. The prediction of the spatial correlation of streamwise velocity fluctuations in the cross-stream direction, illustrated in Fig. 32, had to be limited to consideration of only mean properties in the particle wakes. To include effects of wake turbulence in these predictions would require measurements of lateral correlations in turbulent wakes, and no such measurements have been reported. However, since the measurements emphasize the large-scale features of the flow, which are also emphasized by predictions using only mean wake properties, comparing this prediction with measurements is reasonable. In agreement with the measurements, the prediction indicates that the correlation should be independent of particle

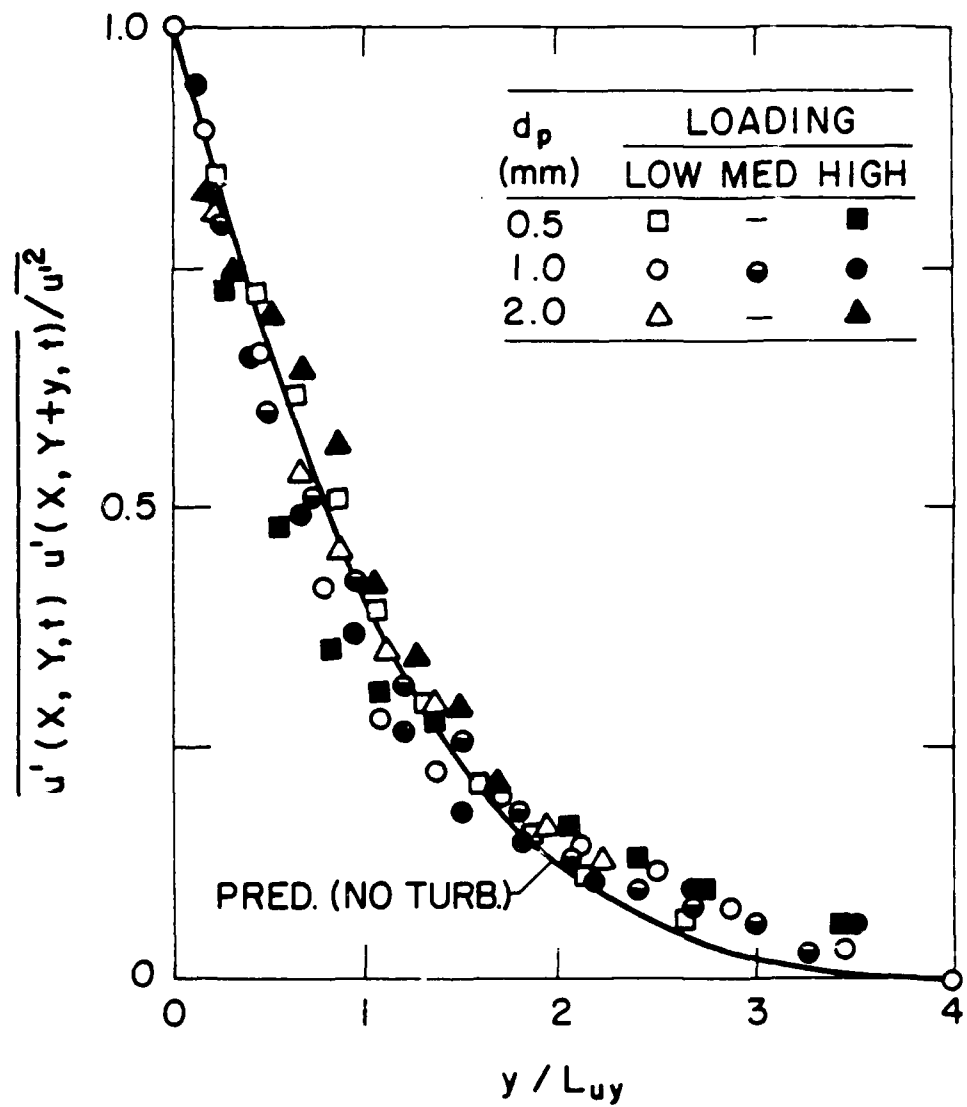


Figure 32 Lateral spatial correlation of liquid streamwise velocity fluctuations.

loading and size. The quantitative agreement between the predictions and measurements is reasonably good for small separation distances. However, the predictions decay more rapidly than the measurements for large separation distances. Reasons for this behavior will be taken up when integral scales are discussed.

The measured spatial correlations of streamwise velocity fluctuations in the streamwise direction are illustrated in Fig. 33. As before, measurements for the various particle sizes and loadings are plotted as a function of streamwise separation distance normalized by the streamwise integral length scale. The data scatter of the correlations for the streamwise direction, for particular test conditions, is somewhat greater than the correlations for the cross-stream direction. However, within experimental uncertainties, the correlation is independent of particle loading and size. The reasons for this behavior are the same as for the lateral correlations.

For correlations in the streamwise direction, spatial correlations needed to compute the contribution of wake turbulence are available. Therefore, predictions both considering and ignoring the contribution of wake turbulence are illustrated in Fig. 33. In agreement with the measurements, both predictions are essentially independent of particle size and loading over the present test range. When wake turbulence is ignored, the correlation decreases quite rapidly at small separation distances, since the flow is dominated by relatively large length scales associated with the mean velocity profiles of the wake. A greater degree of signal energy is present at small length scales when wake turbulence is considered due to the smaller length scales of wake turbulence. This reduces the rate of decline of the correlation at small separation distances and yields a somewhat more rapid decrease of the correlation at large separation distances. The measurements are in better agreement with the predictions that allow for wake turbulence. This is consistent with other evidence that turbulence in the particle wakes makes a significant contribution to the turbulence properties of the continuous phase for present test conditions.

Length and Time Scales. The measured and predicted length and time scales are summarized in Table 5. Measured integral time scales are only available for the lowest particle loadings due to limitations in correcting for mean velocities, as noted earlier. Measured integral length scales are averages for all loadings. The standard deviations over the range of loadings are given in parentheses. Two sets of predictions appear in the table, with and without consideration of turbulence in the particle wakes.

Measured temporal and spatial integral scales do not vary significantly with particle size. Furthermore, loading appears to have relatively little effect on the integral scales as well. This behavior is consistent with the weak variation of correlations with particle size and loading that was discussed earlier. The ratio between streamwise and cross-stream temporal integral scales is roughly 1.5. However, the available data base for this ratio is relatively limited. The ratio between streamwise and cross-stream spatial integral scales is roughly 3, which reflects the high level of anisotropy of the present flows.

Predicted integral scales, considering and ignoring wake turbulence, are summarized in Table 5. T_∞ was chosen to match measured streamwise velocity fluctuations for baseline predictions; taking $x/d_p = U_\infty T_\infty/d_p = 175$ and 2730 when wake turbulence was considered and ignored, respectively. The sensitivity of predicted integral scales to variations in T_∞ is also indicated in Table 5 by including results for $x/d_p = U_\infty T_\infty/d_p = 25,000$, which was used for temporal spectra and spatial correlations in Figs. 30-33.

Predicted integral scales in Table 5 are properly independent of the rate of dissipation but are generally unsatisfactory otherwise. A possible exception is T_u

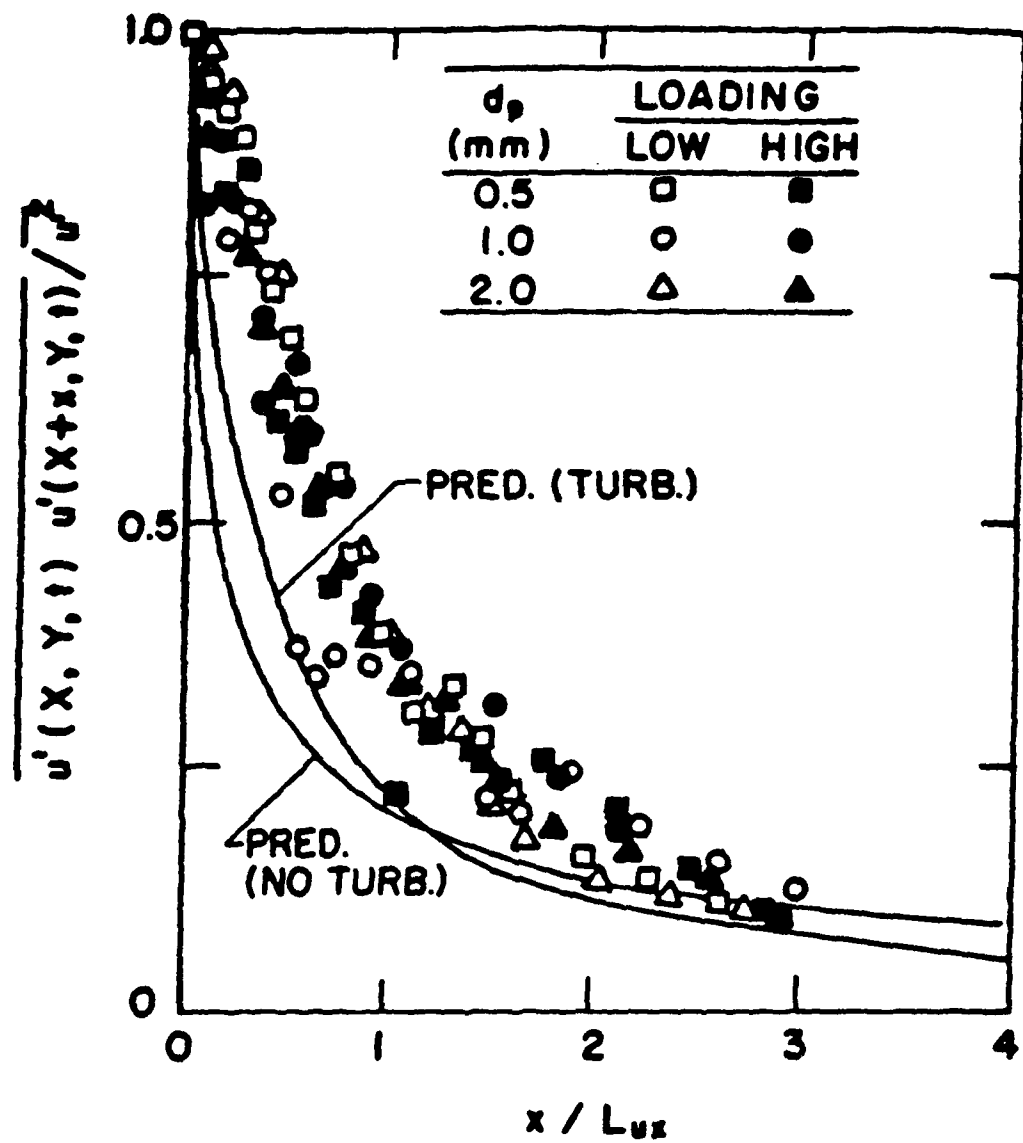


Figure 33 Longitudinal spatial correlation of liquid streamwise velocity fluctuations.

Table 5. Measured and Predicted Integral Time and Length Scales

d_p (mm)	0.5	1.0	2.0
T_u (s):			
Measured ^a	6	7	7
Predicted (turb.) ^b	10 (10)	10 (13)	12 (21)
Predicted (no turb.) ^c	130 (130)	130 (166)	130 (225)
T_v (s):			
Measured ^a	4	---	---
Predicted (turb.) ^b	0.001	0.001	0.001
Predicted (no turb.) ^c	0.17	0.17	0.17
L_{uy} (mm):			
Measured ^d	17 (2)	15 (2)	21 (3)
Predicted (turb.) ^b	---	---	---
Predicted (no turb.) ^c	2	4	7
L_{ux} (mm):			
Measured ^d	59 (2)	59 (6)	57 (2)
Predicted (turb.) ^b	70 (710)	140 (1,900)	280 (5,600)
Predicted (no turb.) ^c	850 (9,200)	1,700 (23,700)	2,550(59,800)

^aMeasured for lowest particle loading only.^bPredicted assuming $x/d_p = U_\infty T_\infty / d_p = 175$. Numbers in parentheses are for $x/d_p = 25,000$.^cPredicted assuming $x/d_p = U_\infty T_\infty / d_p = 2730$. Numbers in parentheses are for $x/d_p = 25,000$.^dAverage value for loading range of Table 1. Standard deviation is in parentheses.

considering turbulence, where predicted and measured magnitudes and trends are similar. For the rest, T_v is vastly underestimated by prediction, particularly when turbulence is considered. Predictions of T_u and L_{ux} are vastly overestimated when turbulence is ignored, and predicted spatial integral scales exhibit variations with particle diameter that are not supported by the measurements. Furthermore, the convergence problem that required an empirical selection of T_∞ has a significant impact on predictions of L_{ux} due to its sensitivity to this choice. Finally, no compromise selection of T_∞ could be found that provides good predictions of both velocity fluctuations and integral scales.

Discussion. In spite of numerous simplifications, the theory was helpful for explaining many features of the measurements and predictions were generally reasonable. However, the convergence problem when particle wakes are evaluated and the relatively poor predictions of integral scales and spatial correlations are disconcerting. Two phenomena that may be responsible for these difficulties are discussed in the following: disturbances of wakes due to turbulent dispersion of particles and the structure of particle wakes on the present turbulent environment.

Recall that predictions were based on particles settling along vertical lines, i.e., effects of turbulent dispersion of particles were ignored. For present experimental conditions, however, turbulent dispersion was significant, and crosstream particle and liquid velocity fluctuations were comparable (this will be taken up in the next section). Thus, particle wakes were actually deposited along sinuous paths — affecting the apparent width of the wakes and augmenting crosstream velocity fluctuations by placing a component of the mean velocity along the wake axis into a horizontal plane. Since wakes grow relatively slowly in the radial direction and have small mean radial velocities, these effects can be significant for homogeneous particle-laden flows.

Dye tracks released into the wakes of individual particles were photographed in order to help quantify potential effects of turbulent dispersion of particles. Considering only fresh wakes, with the particle still in view, showed that the projected crosstream displacements of particles were comparable to characteristic wake radii (based on the mean streamwise velocity being 1-5% of the mean streamwise velocity at the axis), e.g., 2-6 mm for $x/d_p = 175$, which is consistent with crosstream liquid and particle velocity fluctuation being comparable. Rough calculations show that this effect was sufficient to increase predictions of L_{uy} to the range of the measurement and reduce its sensitivity to particle diameter, so the effect is significant. Additionally, projected particle tracks were oriented up to 10° from the vertical direction, which causes momentum along the wake axis to be deposited into the crosstream direction. This would tend to reduce potential effects of wake turbulence inferred earlier and modify predictions of crosstream scales as well. Thus, the effect of turbulent dispersion of particles on the turbulent field that they create must be considered when defining the particle flow field for predictions using the present approach.

Another nonlinear interaction is the effect of the turbulent field generated by the particles on the properties of their wakes. Present predictions were based on the properties of wakes for rigidly-mounted spheres in a nonturbulent environment. Turbulent dispersion of particles and deflection, distortion and improved mixing of wakes in a turbulent environment are likely to modify behavior from wakes in a nonturbulent environment. In particular, wakes in a turbulent environment should mix more quickly and observe different scaling rules than wakes in nonturbulent environments (Tennekes & Lumley 1972). For example, similarity was assumed to obtain the turbulent wake properties of equations (3.33) and (3.34), with specific results requiring a turbulent viscosity that is constant over the wake cross-section and decreases with increasing streamwise distance. Such scaling is unlikely to be relevant for wakes with modest Reynolds numbers in a turbulent environment, and proper scaling might resolve the convergence problem directly. Finally,

as mentioned earlier, little is known about the turbulent structure of wakes at the modest Reynolds numbers of the present tests, which also impacts predictions.

Clearly, further progress concerning turbulence modulation in homogeneous dilute particle-laden flows will require a better understanding of particle wake properties. This includes the structure of turbulent wakes at moderate Reynolds numbers, the structure of wakes in turbulent environments, and the structure of wakes of freely-moving particles undergoing turbulent dispersion.

3.4.3 Dispersed-Phase Properties

Velocities. Measured and predicted particle properties included mean and fluctuating velocities and velocity probability density functions. These results are considered in the following, concluding with a study of the sensitivity of predictions to various parameters of the analysis.

Measurements of mean streamwise and fluctuating streamwise and cross-stream particle velocities are illustrated in Fig. 34. The velocities are plotted as a function of dissipation similar to the earlier liquid velocity measurements. Results are shown for 0.5, 1.0 and 2.0 mm diameter particles. A range of particle loadings (rates of dissipation) are considered, rather than just the loadings for each particle size summarized in Table 4, so that the trends of the measurements can be observed more readily.

Mean particle velocities illustrated in Fig. 34 do not exhibit any systematic variation with dissipation and are identical to the terminal velocities of the particles within experimental uncertainties (see Tables 3 and 4). This is in sharp contrast to the behavior of particles during sedimentation processes, where mean settling velocities tend to decrease as the particle number flux (which is analogous to dissipation through equation (3.5)) increases. The main reason for this behavior is that the present rather large particles have terminal velocities that are substantially greater than the velocities of the liquid phase (roughly an order of magnitude larger), while terminal velocities are relatively low for sedimentation processes and are comparable to velocities induced in the liquid phase by particle motion. In particular, liquid phase velocities during sedimentation are primarily caused by the flow field immediately around the particle, since the particles have low Reynolds numbers in the Stokes flow regime, not the wake (Batchelor, 1972). Thus, the downflow of the particle flow field is counteracted by a mean bulk liquid upflow for sedimentation, which tends to slow the particle settling rate as the concentration of particles increases.

Effects of this type are much less significant for present conditions, since liquid velocities are associated with velocities in the particle wakes which are much lower than the particle terminal velocity and the velocity field immediately around the particle. Furthermore, since wake properties dominate the present liquid phase properties, the cross-sectional area associated with downflow is larger than for sedimentation, tending to increase the probability that particles are in a region of downflow. The net effect is that terminal velocities are influenced to only a small extent by bath flow properties, and this effect could not be resolved during the present experiments. At higher loadings than those tested here, however, the picture could change. Through equations (3.60) - (3.64), velocity fluctuations increase according to $\epsilon^{1/2}$, so that very large particle loadings could yield velocities more comparable to terminal velocities and the process might display effects more like sedimentation. Particle concentrations at such conditions would be very high, however, more like fluidized bed processes, so that such flows would not be dilute and extrapolation of present results to these conditions would be very questionable.

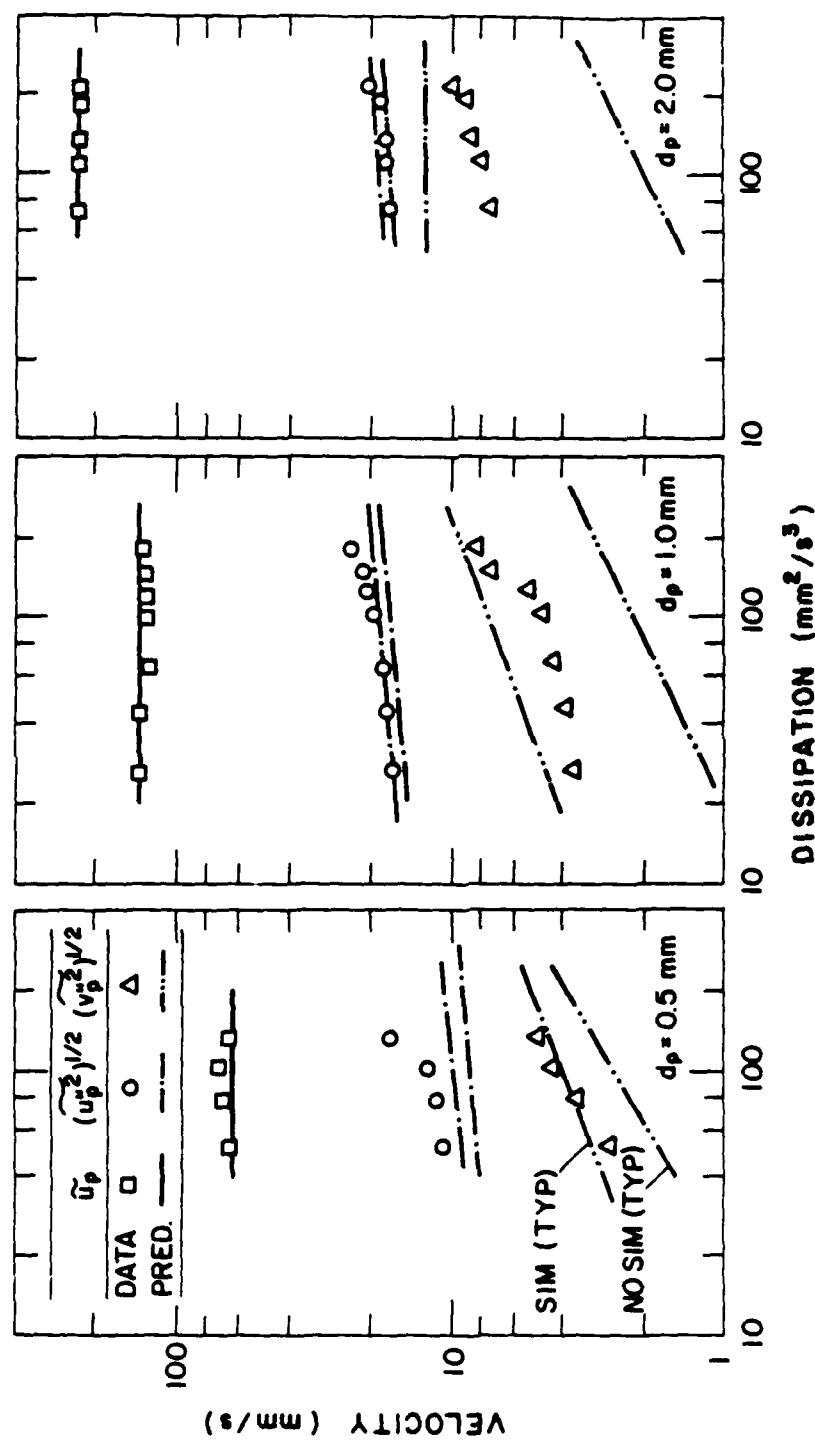


Figure 34 Particle velocities.

Nevertheless, the evolution between the present dilute particle flows and fluidized bed conditions has interesting implications for better understanding of both flows and certainly merits study.

The particle velocity fluctuations illustrated in Fig. 34 are influenced by several phenomena: self-induced particle motion, apparent streamwise velocity fluctuations due to the variation of terminal velocities over the size range of the present experiments, and turbulent dispersion of the particles. Results summarized in Table 6 help provide some insight about the relative importance of these phenomena for present test conditions. This table is a summary of the ratios of particle velocity fluctuations normalized by the analogous bath liquid velocity fluctuations. Test conditions include low and high loadings and all three particle sizes. Streamwise and cross-stream velocity fluctuations are considered for self-induced motion (obtained by calibration) and motion within the bath itself. However, only the streamwise apparent velocity fluctuations due to particle size variations (obtained by calibration) have been considered, since this is the only velocity component that is relevant for this effect.

Comparing the velocity fluctuation ratios listed in Table 6 for self-induced motion and terminal velocity variations with those measured in the bath provides a relative measure of the importance of these effects in comparison with turbulent dispersion. It is seen that streamwise velocity fluctuations due to self-induced motion are small, while apparent fluctuations due to terminal velocity variations are comparable to those measured in the bath. Therefore, streamwise particle velocity fluctuations are dominated by effects of terminal velocity variations due to variations of particle diameter for present test conditions, and little can be learned about turbulent dispersion from this velocity component. A possible exception is the highest loading with the 0.5 mm diameter particles, where effects of terminal velocity variations are roughly half the fluctuation levels observed in the bath. Nevertheless, reduced sensitivity due to direct effects of turbulent dispersion still makes this condition marginal for definitive conclusions. The results for cross-stream velocity fluctuations suggest that effects of self-induced motion are relatively small in comparison to turbulent dispersion for the 0.5 mm diameter particles. Therefore, this condition provides a reasonable indication of effects of turbulent dispersion. In contrast, cross-stream velocity fluctuations due to self-induced particle motion are generally larger than those observed in the bath for the 1.0 and 2.0 mm diameter particles, so that these test conditions are of questionable value for gaining information about turbulent dispersion. A curious phenomenon is that cross-stream velocity fluctuations observed in the bath for the larger particle sizes are actually smaller than those observed during the calibration tests for self-induced particle motion. This suggests that the turbulent field of the bath may be interfering with eddy-shedding that is thought to cause this behavior. Additional study of the possibility under more controlled conditions would be desirable.

The previous considerations imply that turbulent dispersion is the dominant process causing particle velocity fluctuations only for the cross-stream velocity fluctuations with the 0.5 mm diameter particles for present test conditions. In this case, the ratio of particle to liquid cross-stream velocity fluctuations are in the range 1.6-1.7, which implies that particle velocities overshoot liquid velocities. Similarly, if the contribution of terminal velocity variations is subtracted from the streamwise velocity fluctuations measured in the bath the result still yields particle streamwise velocity fluctuations greater than the liquid streamwise velocity fluctuations for the 0.5 mm diameter particles. Viewed in terms of turbulent transport of particles, this implies that the turbulent diffusivity of the particles is greater than that of the fluid, i.e., the turbulent Schmidt number for turbulent dispersion is less than unity. This type of behavior occurs since particle response varies over the spectra of the continuous-phase velocity fluctuations, and, depending upon the energy content of the range of frequencies where the response is greatest, the particle fluctuations can be greater

Table 6 Ratios of Particle/Liquid Velocity Fluctuations

d_p (mm)	0.5	1.0	2.0			
Loading	Low	High	Low	High	Low	High
$(\tilde{u}'_{ps}^2)^{1/2} / (\bar{u}'^2)^{1/2}$	0.6	0.4	0.6	0.3	0.1	0.1
$(\tilde{u}'_p^2)^{1/2} / (\bar{u}'^2)^{1/2}$	2.0	1.4	5.9	2.8	4.3	2.6
$(\tilde{u}'_p^2)^{1/2} / (\bar{u}'^2)^{1/2}$	3.3	2.6	7.1	4.3	5.1	3.4
$(\tilde{v}'_{ps}^2)^{1/2} / (\bar{v}'^2)^{1/2}$	0.7	0.4	4.7	2.4	7.9	4.4
$(\tilde{v}'_p^2)^{1/2} / (\bar{v}'^2)^{1/2}$	1.7	1.6	2.1	3.2	4.6	3.2

aThe loadings in this table have the following ranges of dissipation rates: low, 67-80 mm²/s³; high, 129-141 mm²/s³.

or smaller than a single measure of liquid-phase fluctuations, such as the root-mean squared velocity fluctuation. However, the results do indicate that turbulent dispersion is very effective in the homogeneous turbulence field generated by the particles themselves. This behavior is caused by the large frequency range of the continuous-phase velocity fluctuations, since both mean and turbulent wake properties contribute to the spectra. See Figs. 30 and 31. With such a large range of frequencies available, the probability that the particles will encounter a range of frequencies where their response is high is enhanced—enhancing effects of turbulent dispersion as well. In particular, particle response tends to be highest (approaching unity) at low frequencies (Al Tawee & Landau, 1977). Thus, the high signal energy content at low frequencies due to effects of mean wake velocities is probably a significant factor in the good turbulent dispersion properties of present homogeneous particle-laden flows.

Combining an efficient mechanism of turbulent dispersion with effects of self-induced motion and variations of terminal velocities generally yields particle velocity fluctuations that are greater than liquid velocity fluctuations (as much as 5.5 times greater) over the present test range. Thus, when considering effects of turbulent dispersion, intuitive ideas that particles will have some difficulty in responding to liquid-phase fluctuations due to their inertia and will necessarily mix more slowly than an infinitely-small particle as a result should be accepted with caution.

Effects of loading (dissipation) on particle velocity fluctuations can be best seen in Fig. 34. Streamwise particle velocity fluctuations are large and do not vary very much with dissipation, since they are dominated by variations of terminal velocities over the present test range (the highest loading for the 0.5 mm diameter particles exhibits a greater effect, but measurements are also least accurate at this condition since particle concentrations are greatest). In contrast, cross-stream particle velocity fluctuations are significantly increased with increasing rates of dissipation for all particle sizes. As just discussed, this increase can be attributed to effects of turbulent dispersion for the 0.5 mm diameter particles. In fact, noting that the ratio of $(\tilde{v}_p^2)^{1/2}/(v'^2)^{1/2}$ is roughly constant, (indicating similar particle response to cross-stream liquid velocity fluctuations) over the present test range (see Table 7), this increase simply follows the $\epsilon^{1/2}$ variation of liquid velocity fluctuations. Surprisingly, the cross-stream particle velocity fluctuations also exhibit significant increases with increasing dissipation for the 1.0 and 2.0 mm diameter particles, even though these results should be dominated by self-induced lateral motion of the particles (see Table 7). This suggests that eddy-shedding mechanisms leading to self-induced lateral motion in still liquids may be less effective in turbulent environments, so that effects of turbulent dispersion are greater than might be anticipated from the results summarized in Table 7.

Predictions based on the present stochastic analysis of the particle phase are also illustrated in Fig. 34. Recall that these predictions are based on the measured turbulence properties of the liquid phase and effects of particle size variations are considered. However, effects of self-induced motion of the particles have been ignored, since no information is available concerning the fluctuating forces on particles due to irregular particle shapes and eddy-shedding. In an effort to provide some indication of potential effects of self-induced particle motion, predictions are shown where mean-squared particle velocity fluctuations from the particle trajectory simulations and the self-induced motion are vectorially added, i.e., $\tilde{u}_p^2 = \tilde{u}_{p \text{ pred}}^2 + \tilde{u}_{ps}^2$, etc. These predictions are denoted SIM

Table 7 Results of Sensitivity Study of Particle Properties^a

Input Parameter (100% change)	Change of Output Parameter (%)		
	\tilde{u}_p	$(\tilde{u}_p^2)^{1/2}$	$(\tilde{v}_p^2)^{1/2}$
$(\bar{u}^2)^{1/2}$	~ 0	20 to 24	~ 0
$(\bar{v}^2)^{1/2}$	~ 0	~ 0	98 to 100
τ_L	~ 0	0 to 4	~ 0
C_D	-32 to -39	-28 to -32	~ 0

^aThese results were similar for the 0.5, 1.0 and 2.0 mm diameter particles over the present range of particle loadings; therefore, only the range of output changes are shown.

Use of standard values or $\Delta_A = \Delta_H = 0$ resulted in negligible changes of predictions.

to indicate that "self-induced motion" has been considered. The baseline predictions without consideration of self-induced motion are denoted by NO SIM.

Mean velocity predictions are in excellent agreement with measurements in Fig. 34. This is not a very critical test of predictions, however, since the predictions largely reflect the correct calibration of particle drag properties that was discussed earlier. About the only new feature that the simulations include is the upward biasing of mean particle drag properties by turbulent fluctuations, i.e., computing particle drag using average liquid-phase properties is not correct, since drag is not a linear function of the relative velocity for Reynolds numbers greater than unity (Faeth, 1983, 1987). This is considered by the simulation, since drag is based on instantaneous relative velocities with final averages only being obtained over ensembles of trajectory predictions. However, even this effect is not very significant for present test conditions, since mean particle velocities are much greater than bath velocity fluctuations ($(\bar{u}'^2)^{1/2}/\bar{u}_p$) never exceeds 8% for present test conditions) and differences between the two types of averages are small in comparison to experimental uncertainties.

Predicted streamwise particle velocity fluctuations in Fig. 34 generally agree with measurements within experimental uncertainties. In this case, the fluctuations are dominated by the effects of variations of terminal velocities, and effects of self-induced motion are small (see Table 7). Nevertheless, it is encouraging that the relatively small increase of particle velocity fluctuations due to increased turbulent dispersion with increasing dissipation is represented quite well by the predictions.

The comparison between predicted and measured cross-stream velocity fluctuations in Fig. 34 is somewhat hampered by effects of self-induced particle motion. However, this effect is modest for the 0.5 mm diameter particles, and the baseline predictions (NO SIM) are reasonably good, while the present ad hoc correction for self-induced particle motion yields results (SIM) that are in excellent agreement with measurements. The present reasonably good simulation of particle motion suggests that the most important properties of the turbulent field have been considered and that effects of turbulence on particle drag are modest. The last observation is reasonable, since the relative velocities of the particles are large in comparison to liquid phase velocity fluctuations, i.e., relative turbulence intensities are small. Predictions ignoring self-induced motion are much smaller than the measurements for the 1.0 and 2.0 mm diameter particles, while including the self-induced motion causes cross-stream particle velocity fluctuations to be overestimated. This highlights the need to develop a rational method of including the self-induced forces on the particles in particle trajectory calculations. As noted earlier, the observation also suggests that the turbulent flow field may be modifying eddy-shedding mechanisms responsible for self-induced particle motion as well.

Probability Density Functions. The probability density functions of streamwise particle velocity fluctuations are plotted as a function of normalized variables in Fig. 35. Measurements from the different loadings of the 0.5 and 2.0 mm diameter particles appear on the plots. These measurements are not significantly different from the particle drag calibrations, since particle velocity fluctuations in the streamwise direction are dominated by terminal velocity variations. Thus, predictions both considering and ignoring self-induced motion are very nearly the same and are in reasonably good agreement with the measurements. However, since the results are normalized, this is not a very sensitive test of predictions. The predictions essentially yield Gaussian probability density functions.

The probability density functions of cross-stream particle velocity fluctuations are illustrated in Fig. 36. The method of plotting and test conditions are the same as Fig. 35.

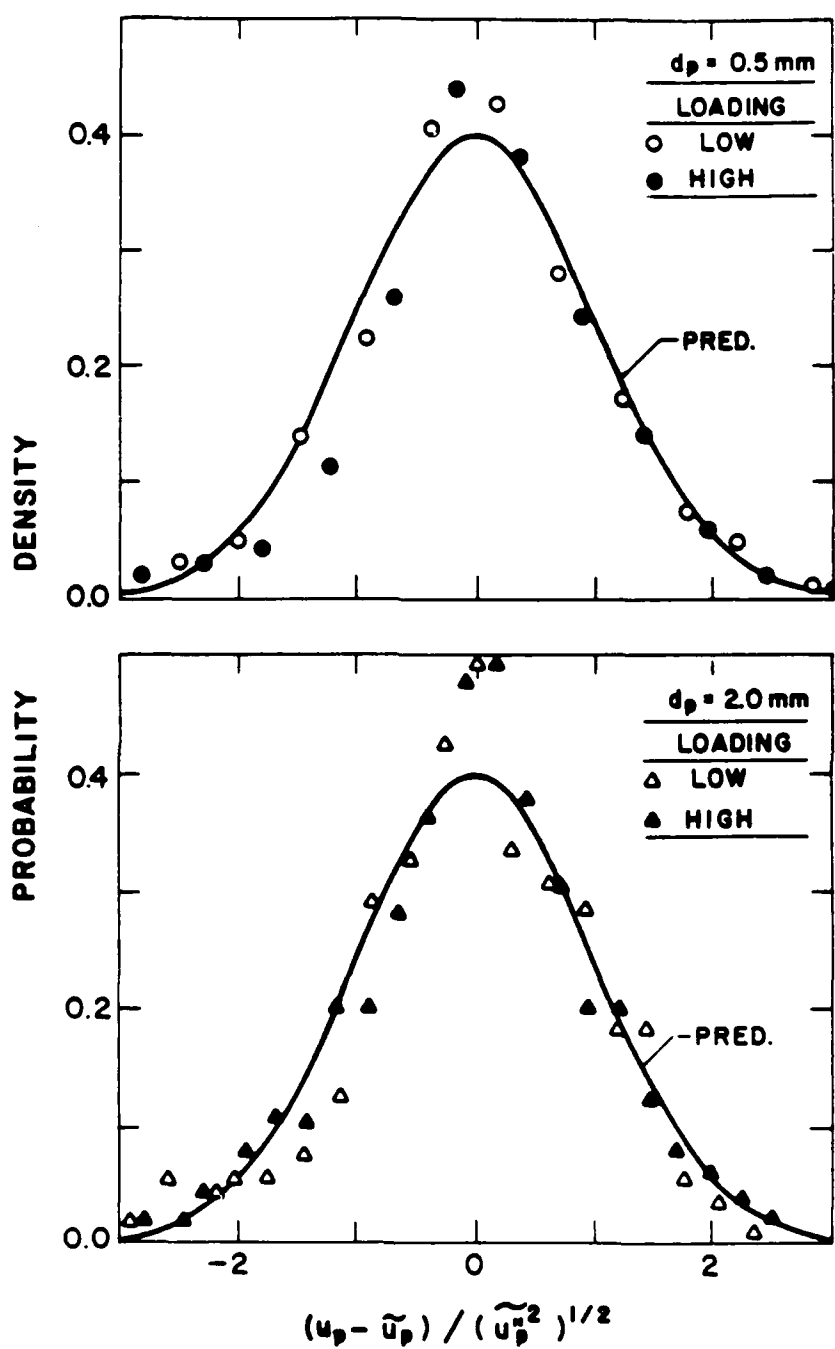


Figure 35 Probability density function of particle streamwise velocity fluctuations.

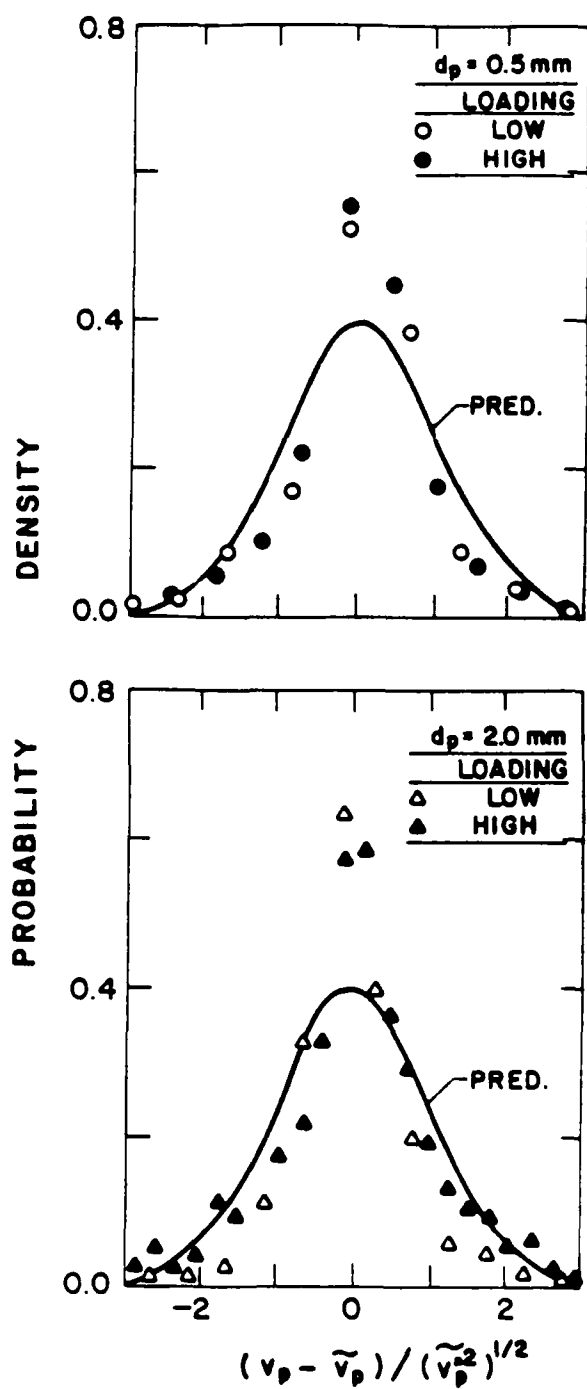


Figure 36 Probability density function of particle crosstream velocity fluctuations.

Due to the method of normalization, results for the 0.5 mm diameter particles (which are dominated by effects of turbulent dispersion) are essentially the same as results for larger particles (which are dominated by effects of self-induced particle motion). Similarly, the various predictions are nearly the same, and all of the results approximate Gaussian probability density functions.

Sensitivity Study. The numerical simulations of particle motion required the prescription of a number of parameters subject to significant uncertainties, as follows: the liquid velocity fluctuations, the Lagrangian integral time scale, the particle drag coefficients, and the virtual mass and Basset history force parameters of equation (3.48). In order to better understand the nature and limitations of the numerical simulation, the sensitivity of predictions to variations of these parameters was studied.

Results of the sensitivity study appear in Table 7, where changes in output parameters for 100% changes in input parameters are summarized. Effects of size variations were considered during these computations, but not effects of self-induced particle motion. These results were similar for all three particle sizes over the range of loadings considered during this investigation. Therefore, only the range of output variable changes is shown. Predicted mean streamwise particle velocities were only sensitive to estimates of particle drag coefficients, where 100% changes of C_D yielded 30-40% changes of the particle mean velocity. This behavior is expected, since terminal velocities of the particles were not influenced strongly by the bath turbulence and are proportional to $C_D^{1/2}$, see equation (3.67).

Predicted streamwise particle velocity fluctuations were primarily influenced by changes of the drag coefficient and streamwise liquid velocity fluctuations. The effect of drag coefficient is the same as for mean particle velocities — for the same reasons. The effect of 100% increase of liquid velocity fluctuations was only 20-24%, since streamwise particle velocity fluctuations were dominated by variations of particle terminal velocities due to size variations for present test conditions. The small effects of cross-stream liquid velocity fluctuations occurs since this variable primarily influences streamwise properties by modifying particle drag coefficients. Therefore, its effect is not large, since particle terminal velocities are much greater than liquid velocity fluctuations for present test conditions. The insensitivity to variations of τ_L is most closely associated with effects of turbulent dispersion that are small for this component of velocity.

Predicted cross-stream particle velocity fluctuations were only influenced by variations of cross-stream liquid velocity fluctuations, where the changes of the output have a one-to-one correspondence with changes of the input. This highlights the strong interaction between the particles and the turbulence of the liquid phase for present test conditions, yielding very effective turbulent dispersion, i.e., radial particle velocity fluctuations are greater than liquid velocity fluctuations in the cross-stream direction. The insensitivity to streamwise liquid velocity fluctuations follows for the same reasons that cross-stream liquid velocity fluctuations had little effect on streamwise particle velocity fluctuations. The insensitivity to both τ_L and C_D are probably related. The effective turbulent dispersion for present conditions implies that particles have sufficiently high drag to respond quite closely to the lateral liquid velocity fluctuations. Therefore, additional time to respond is not needed, while increasing drag only serves to reduce already small relative velocities in the cross-stream direction.

Finally, effects of using the standard values of Δ_A and Δ_H or setting these parameters equal to zero were small, since mean particle velocities are not affected by effects of acceleration, streamwise particle velocity fluctuations are dominated by particle

size variations, and particle response in the cross-stream direction is very high and is relatively insensitive to parameters influencing particle drag properties.

3.5 Summary of Results

1. Velocity fluctuations could be correlated solely as a function of the rate of dissipation of particle energy in the liquid.
2. Streamwise velocity fluctuations were roughly twice crosstream velocity fluctuations for all test conditions, suggesting a significant influence of wakes behind individual particles on the properties of the flow.
3. Normalized temporal spectra, spatial correlation coefficients, and temporal and spatial integral scales were relatively independent of both particle size and the rate of dissipation of particle energy in the liquid.
4. Temporal spectra indicated a large range of frequencies, even though particle and wake Reynolds numbers were relatively small, since both mean and fluctuating properties of the particle wakes contribute to the spectra because particle arrivals were random.
5. An analysis based on linear superposition of undistorted particle wakes in a nonturbulent environment predicted many properties of the flow reasonably well. However, it yielded poor estimates of integral scales and streamwise spatial correlations. These deficiencies are largely attributed to effects of turbulent dispersion of the particles and effects of an ambient turbulence field on the structure of the wakes.
6. Linear superposition of particle wakes in the analysis presented convergence problems similar to convergence problems encountered during analysis of sedimentation processes. This was resolved by assuming that only the near-field region of the wakes, $x/d_p = T_\infty U_\infty / d_p < 175$, would maintain sufficient coherence to contribute to flow properties as a wake — a choice that matched predictions and measurements of streamwise velocity fluctuations. However, a more rational resolution of the convergence problem should be sought.
7. Particle-laden flows typically involve turbulent dispersion of particles and particle Reynolds numbers less than 1000 within a turbulent environment. More information is needed concerning the mean and turbulent structure of wakes under these conditions in order to address the difficulties of the present analysis in a rational manner.
8. Present particles exhibited drag coefficients that were within 14% of the standard drag curve of spheres in spite of the presence of some ellipticity in their shapes. Individual particles falling in a stagnant water bath, however, exhibited self-induced motion, particularly in the lateral direction. Self-induced motion increased with increasing particle size due to eddy-shedding at large particle Reynolds numbers, as well as increased ellipticity of the larger particles.

9. Mean particle velocities were independent of dissipation and approached the terminal velocity of the particles. Particle velocity fluctuations exceeded liquid velocity fluctuations for all test conditions. Streamwise particle velocity fluctuations were relatively independent of dissipation as they were dominated by modest size differences leading to terminal velocity differences. This masked effects of turbulent dispersion for this velocity component. Cross-stream velocity fluctuations were less affected by size variations and showed increases with increasing dissipation. They were large due to effects of turbulent dispersion which was enhanced by effects of self-induced lateral motion of the particles—particularly for the 1.0 and 2.0 mm diameter particles. Measurements indicated that effects of self-induced motion were reduced in the turbulent bath, suggesting that turbulence may interfere with eddy-shedding mechanisms thought to be responsible for this behavior.
10. The stochastic simulation of particle motion yielded encouraging results and was insensitive to the empirical parameters used in the particle motion equation and the Lagrangian integral time scale. The use of statistical time-series techniques to simulate liquid-phase properties is recommended for analysis of turbulent dispersion processes since it eliminates many ad hoc features of earlier methods.

4. SUMMARY OF INVESTIGATION

4.1 Articles and Papers

- Bulzan, D. L., Shuen, J.-S. & Faeth, G. M. (1987) Particle-laden swirling free jets: measurements and predictions. AIAA Paper No. 87-0303.
- Bulzan, D. L., Shuen, J.-S. & Faeth, G. M. (1988) Particle-laden weakly swirling free jets: measurements and predictions. AIAA Paper No. 88-3138.
- Bulzan, D. L., Shuen, J.-S. & Faeth, G. M. (1988) Particle-laden weakly swirling free jets: measurements and predictions. Proceedings of the 1988 Spring Technical Meeting, Central States Section of the Combustion Institute, Pittsburgh, pp. 21-26.
- Faeth, G. M. (1987) Mixing, transport and combustion in sprays. Prog. Energy. Combust. Sci. 13, 293-345.
- Faeth, G. M. (1987) Structure of nonpremixed and premixed combusting pressure-atomized sprays. Proceedings of the Twentieth Fall Technical Meeting, Eastern Section of the Combustion Institute, Pittsburgh, pp. B.1-B.10.
- Faeth, G. M. (1987) Turbulent multiphase flows. Turbulent Reactive Flows (S.N.B. Murthy and R. Borghi, eds.), Springer-Verlag, New York, pp. 784-814.
- Parthasarathy, R. N. & Faeth, G. M. (1987) Structure of particle-laden turbulent water jets in still water. Int. J. Multiphase Flow 13, 699-716.

- Parthasarathy, R. N. & Faeth, G. M. (1987) Structure of turbulent particle-laden jets having comparable phase densities. Proceedings of the 1987 Spring Technical Meeting, Central States Section of the Combustion Institute, Pittsburgh, pp. 464-469.
- Parthasarathy, R. N. & Faeth, G. M. (1988) Homogeneous turbulence in dilute particle-laden flows. 41st Annual Meeting: American Physical Society Division of Fluid Dynamics, Buffalo.
- Ruff, G. A., Sagar, A. D. & Faeth, G. M. (1987) Structure of large-scale pressure-atomized sprays. First Annual Conference of ILASS-Americas, Madison, WI.
- Ruff, G. A., Sagar, A. D. & Faeth, G. M. (1989) Structure and mixing properties of pressure-atomized sprays. AIAA J. 27, 901-908.
- Ruff, G. A., Bernal, L. P. & Faeth, G. M. (1988) Structure of near-injector region of nonevaporating pressure-atomized sprays. AIAA Paper 89-0050; also J. Prop. Power, submitted.
- Ruff, G. A., Bernal, L. P. & Faeth, G. M. (1989) Dense-spray properties of nonevaporating pressure-atomized sprays. Proceedings of the 1989 Spring Technical Meeting, Central States Section of the Combustion Institute, Pittsburgh, pp. 281-286.

4.2 Participants

- G. M. Faeth, Principal Investigator; Professor, The University of Michigan.
- R. N. Parthasarathy, Graduate Assistant, Doctoral Candidate, The University of Michigan.
- G. A. Ruff, Graduate Assistant, Doctoral Candidate, The University of Michigan.
- A. Sagar, Graduate Assistant.

4.3 Oral Presentations

- G. M. Faeth, "Turbulence/Drop Interactions in Sprays," Southwest Mechanics Seminar Series: Southwest Research Institute, San Antonio; University of Houston, Houston; and Shell Development Company, Houston, October 1986.
- G. M. Faeth, "Turbulence/Particle Interactions in Dilute Particle-Laden Liquid Jets," Department of Mechanical Engineering, Carnegie-Mellon University, Pittsburgh, February 1987.
- G. M. Faeth, "Particle-Laden Jets having Comparable Phase Densities," Chemical and Physical Sciences Laboratory Seminar Series, Ford Scientific Research Laboratories, Dearborn, MI, March 1987.
- G. M. Faeth, "Turbulent Multiphase Flows," U.S.-France Workshop on Turbulent Reactive Flows, University of Rouen, France, July 1987.

- G. M. Faeth, "Structure of Nonpremixed and Premixed Combusting Pressure-Atomized Sprays," Fall Technical Meeting, Eastern Section of the Combustion Institute, Gaithersburg, MD, November 1987.
- G. M. Faeth, "Structure and Mixing Properties of Pressure-Atomized Sprays," AIAA 26th Aerospace Sciences Meeting, Reno, NV, January 1988.
- G. M. Faeth, "Dense Spray Structure and Phenomena," AFOSR Contractors' Meeting on Combustion, Pasadena, CA, June 1988.
- G. M. Faeth, "Structure of Pressure-Atomized Sprays," Propulsion Seminar Series, University of Alabama, Huntsville, AL, September 1988.
- G. M. Faeth, "Turbulence Modulation in Homogeneous Particle-Laden Flows," State University of New York at Buffalo, Buffalo, NY, February 1989.
- G. M. Faeth, "Turbulence/Dispersed-Phase Interactions in Homogeneous Multiphase Flows," University of Maryland, College Park, MD, February 1989.
- G. M. Faeth, "Structure and Mixing Properties of Dense Sprays," Applied Mechanics Colloquium, Yale University, New Haven, CT, March 1989.
- G. M. Faeth, "Structure of Dense Sprays," Brigham Young University, Provo, UT, March 1989.
- G. M. Faeth, "Dense-Spray Phenomena," General Motors Research Laboratories, Warren, MI, April 1989.
- G. M. Faeth, "Particle/Turbulence Interactions in Dilute Dispersed Flows," AFOSR Droplet/Spray Workshop, Ann Arbor, MI, June 1989.
- R. N. Parthasarathy, "Structure of Turbulent Particle-Laden Jets having Comparable Phase Densities," Spring Technical Meeting, Central States Section of the Combustion Institute, Argonne, IL, May 1987.
- R. N. Parthasarathy, "Structure of Turbulent Particle-Laden Water Jets in Still Water," Seminar, Department of Aerospace Engineering, The University of Michigan, Ann Arbor, MI, March 1987.
- R. N. Parthasarathy, "Turbulence Properties in Homogeneous Particle-Laden Flows," Seminar, Department of Aerospace Engineering, The University of Michigan, Ann Arbor, MI, April 1988.
- R. N. Parthasarathy, "Homogeneous Dilute Particle-Laden Water Flows," Johns Hopkins University, Baltimore, MD, March 1989.
- R. N. Parthasarathy, *Ibid.*, University of Maryland, College Park, MD, March 1989.
- R. N. Parthasarathy, *Ibid.*, University of Michigan, Ann Arbor, MI, April 1989.
- R. N. Parthasarathy, *Ibid.*, University of Iowa, Iowa City, IA, April 1989.
- G. A. Ruff, "Structure of Large-Scale Pressure-Atomized Sprays," First Annual Conference of ILASS-Americas, Madison, WI, May 1987.

- G. A. Ruff, "Structure of the Dense-Spray Region of Pressure-Atomized Sprays," Seminar, Department of Aerospace Engineering, The University of Michigan, Ann Arbor, MI, November 1987.
- G. A. Ruff, "Structure of Dense Sprays," Drexel University, Philadelphia, PA, March 1989.
- G. A. Ruff, *Ibid.*, University of Missouri, Rolla, MO, March 1989.
- G. A. Ruff, *Ibid.*, University of Michigan, Ann Arbor, MI, April 1989.
- G. A. Ruff, *Ibid.*, Sandia Corp., Albuquerque, NM, May 1989.
- G. A. Ruff, *Ibid.*, Naval Postgraduate School, Monterey, CA, June 1989.
- G. A. Ruff, *Ibid.*, Sandia Corp., Livermore, CA, June 1989.

REFERENCES

- Adrian, R. J. & Yao, C. S. (1987) Power spectra of fluid velocities measured by laser Doppler velocimetry. *Expts. in Fluids* 5, 17-28.
- Al Tawee, A. M. & Landau, J. (1977) Turbulence modulation in two-phase jets. *Int. J. Multiphase Flow* 3, 341-351.
- Batchelor, G. K. (1972) Sedimentation in a dilute dispersion of spheres. *J. Fluid Mech.* 52, 245-268.
- Batchelor, G. K. (1973) *An Introduction to Fluid Dynamics*, Cambridge University Press, Cambridge, 450-455.
- Bilger, R. W. (1976) Turbulent jet diffusion flames. *Prog. Energy Combust. Sci.* 1, 87-109.
- Box, G.E.P. & Jenkins, G. M. (1976) *Time Series Analysis*, Revised Edition, Holden-Day, San Francisco, 47-84.
- Bracco, F. V. (1983) Structure of high-speed full-cone sprays. *Recent Advances in Gas Dynamics* (C. Casci, ed.), Plenum Publishing Corporation, New York
- Chehroudi, B., Onuma, Y., Chen, S.-H. & Bracco, F. V. (1985) On the intact core of full-cone sprays. SAE Paper 850126.
- Clift, R., Grace, J. R. & Weber, M. E. (1978) *Bubbles, Drops and Particles*. Academic Press, New York, 266-269; 296-302.
- Csanady, G. T. (1963) Turbulent diffusion of heavy particles in the atmosphere. *J. Atmos. Sci.* 20, 201-208.

- Desjonquieres, P. G., Gouesbet, G., Berlemont, A. & Picart, A. (1986) Dispersion of discrete particles by continuous turbulent motion: new results and discussions. Phys. Fluids 29, 2147-2151.
- Faeth, G. M. (1977) Current status of droplet and liquid combustion. Prog. Energy Combust. Sci. 3, 191-224.
- Faeth, G. M. (1983) The evaporation and combustion of sprays. Prog. Energy Combust. Sci. 9, 1-76.
- Faeth, G. M. (1987) Mixing, transport and combustion in sprays. Prog. Energy Combust. Sci. 13, 293-345.
- Ferguson, J. R. & Stock, D. E. (1986) Particle dispersion in decaying isotropic homogeneous turbulence. Gas-Solid Flows (J. J. Jurewicz, ed.), ASME New York, 9-14.
- Gomi, H. & Hasegawa, K.-I. (1984) Measurements of the liquid phase mass in gas-liquid sprays by X-ray attenuation. Int. J. Multiphase Flow 10, 553-662.
- Gouesbet, G., Berlemont, A. & Picart, A. (1984) Dispersion of discrete particles by continuous turbulent motions. Extensive discussion of the Tchen's theory using a two-parameter family of Lagrangian correlation functions. Phys. Fluids 27, 827-837.
- Hinze, J. O. (1972) Turbulent fluid and particle interaction. Progress in Heat and Mass Transfer, Vol. 6, Pergamon Press, Oxford, 433-452.
- Hinze, J. O. (1975) Turbulence, 2nd ed., McGraw-Hill, New York, 427 and 724-734.
- Hiroyasu, H., Shimizu, M. & Arai, M. (1982) The breakup of a high speed jet in a high pressure gaseous atmosphere. Proceedings of the 2nd International Conference on Liquid Atomization and Spray Systems, Madison, Wisconsin.
- Humphreys, W. J. (1964) Physics of the Air, Dover Publications, Inc., New York, 279-281.
- Jeng, S.-M. & Faeth, G. M. (1984) Species concentrations and turbulence properties in buoyant methane diffusion flames. J. Heat Transfer 106, 721-727.
- Katz, E. J. (1966) Atmospheric diffusion of settling particles with sluggish response. J. Atmos. Sci. 23, 159-166.
- Kounalakis, M. E., Gore, J. P. & Faeth, G. M. (1988) Turbulence/radiation interactions in non-premixed hydrogen/air flames. Twenty-Second Symposium (International) on Combustion, The Combustion Institute, Pittsburgh, pp. 1281-1290.
- Kounalakis, M. E., Gore, J. P. & Faeth, G. M. (1988a) Mean and fluctuating radiation properties of turbulent nonpremixed carbon monoxide/air flames. J. Heat Transfer, in press.
- Kraichnan, R. K. (1970) Diffusion by a random velocity field. Phys. Fluids 13, 22-31.

- Lance, M. & Bataille, J. (1982) Turbulence in the liquid phase of a bubbly air-water flow. Advances in Two-Phase Flow and Heat Transfer (S. Kakac and M. Ishii, ed.), Vol. 1, Martinus Nijhof Publishers, The Hague, 403-427.
- Lance, M., Marie, J. L., Charnay, G. & Bataille, J. (1980) Turbulence structure of a co-current air-water bubbly flow. NUREG/CP-0014, Vol. 2, Nuclear Regulatory Commission, Washington, 1363-1383.
- Lance, M., Marie, J. L., & Bataille, J. (1985) Homogeneous turbulence in bubbly flows. Publication FED-29, ASME, New York, 117-124.
- Lefebvre, A. H. (1980) Atomization. Prog. Energy Combust. Sci. 6, 223-246.
- Lockwood, F. C. & Naguib, A.S. (1975) The prediction of fluctuations in the properties of free, round-jet turbulent diffusion flames. Comb. Flame 24, 109-124.
- Lopes, J. C. & Dukler, A. E. (1986) Droplet dynamics in vertical gas-liquid flow. A.I.Ch.E. J., submitted.
- Mao, C.-P., Szekely, G. A., Jr. & Faeth, G. M. (1980) Evaluation of a locally homogeneous flow model of spray combustion. J. Energy 4, 78-87.
- Mao, C.-P., Wakamatsu, Y. & Faeth, G. M. (1980a) A simplified model of high pressure spray combustion. Eighteenth Symposium (International) on Combustion, The Combustion Institute, Pittsburgh, 337-347.
- Meek, C. C. & Jones, B. G. (1973) Studies of the behavior of heavy particles in a turbulent fluid flow. J. Atmos. Sci. 30, 239-244.
- Miesse, C. C. (1955) Correlation of experimental data on disintegration of liquid jets. Ind. Engr. Chem. 470, 1690-1697.
- Modarress, D., Tan, H. & Elghobashi, S. (1984) Two-component LDA measurements in a two-phase turbulent jet. AIAA J. 22, 624-630.
- Nakamura, I. (1976) Steady wake behind a sphere. Phys. Fluids 19, 5-8.
- Nir, A. & Pisman, L. M. (1979) The effect of a steady drift on the dispersion of a particle in a turbulent fluid. J. Fluid Mech. 94, 369-381.
- Odar, F. & Hamilton, W. S. (1964) Force on a sphere accelerating in a viscous fluid. J. Fluid Mech. 18, 302-314.
- Ohba, K. (1979) Relationships between radiation transmissivity and void fraction in two-phase/dispersed flow. Technical Report 29, Osaka University, 245-254.
- Parthasarathy, R. N. (1989) Homogeneous dilute turbulent particle-laden water flow. Ph.D. Thesis, University of Michigan, Ann Arbor.
- Parthasarathy, R. N. & Faeth, G. M. (1988) Homogeneous turbulence in dilute particle-laden flows. 41st Annual Meeting: American Physical Society Division of Fluid Dynamics, Buffalo.

- Parthasarathy, R. N., Ruff, G. A. & Faeth, G. M. (1988) Turbulence modulation and dense-spray structure. Annual Report for Grant No. AFOSR-85-0244, Department of Aerospace Engineering, The University of Michigan, Ann Arbor.
- Parthasarathy, R. N. & Faeth, G. M. (1987) Structure of particle-laden turbulent water jets in still water. Int. J. Multiphase Flow 13, 699-716.
- Parthasarathy, R. N. & Faeth, G. M. (1987a) Structure of turbulent particle-laden jets having comparable phase densities. Proceedings of the 1987 Spring Technical Meeting, Central States Section of the Combustion Institute, Pittsburgh, 464-469.
- Parthasarathy, R. N. & Faeth, G. M. (1987b) Dense-spray structure and phenomena: Part I - Turbulence/dispersed-phase interactions. Annual Report for Grant No. AFOSR-85-0244, Department of Aerospace Engineering, The University of Michigan, Ann Arbor.
- Parthasarathy, R. N., Sagar, A. D. & Faeth, G. M. (1986) Dense-spray structure and phenomena. Annual Report for Grant No. AFOSR-85-0244, Department of Aerospace Engineering, The University of Michigan, Ann Arbor.
- Phinney, R. E. (1973) The breakup of a turbulent liquid jet in a gaseous atmosphere. J. Fluid Mech. 63, 689-701.
- Picart, A., Berlemont, A. & Gouesbet, G. (1986) Modeling and predicting turbulence fields and the dispersion of discrete particles transported by turbulent flows. Int. J. Multiphase Flow 12, 237-261.
- Pisman, L. M. & Nir, A. (1978) On the motion of suspended particles in stationary homogeneous turbulence. J. Fluid Mech. 84, 193-206.
- Putnam, A. (1961) Integrable form of droplet drag coefficient. ARS J. 31, 1467-1468.
- Ranz, W. E. (1958) Some experiments on orifice sprays. Can. J. Chem. Engr. 36, 175-181.
- Reeks, M. W. (1980) Eulerian direct interaction applied to the statistical motion of particles in a turbulent fluid. J. Fluid Mech. 94, 369-381.
- Reitz, R. D. (1978) Atomization and other breakup regimes of a liquid jet. Ph.D. Dissertation No. 1375-T, Princeton University.
- Reitz, R. D. & Bracco, F. V. (1982) Mechanism of atomization of a liquid jet. Phys. Fluids 25, 1730-1742.
- Reitz, R. D. & Bracco, F. V. (1984) Mechanisms of breakup of round liquid jets. Encyclopedia of Fluid Mechanics (N. P. Cheremisinoff, ed.), Vol. III, Chap. 11.
- Reitz, R. D. & Diwakar, R. (1987) Structure of high-pressure fuel sprays. SAE Paper No. 870598.
- Rice, S. O. (1954) Mathematical analysis of random noise. Noise and Stochastic Processes (N. Wax, ed.), Dover Publications Inc., New York, 133-294.

- Ricou, F. P. & Spalding, D. B. (1961) Measurements of entrainment by axisymmetrical turbulent jets. J. Fluid Mech. 11, 21-32.
- Ruff, G. A. & Faeth, G. M. (1987) Dense-spray structure and phenomena: Part II - Pressure-atomized sprays. Interim Report for Grant No. AFOSR-85-0244, Department of Aerospace Engineering, The University of Michigan, Ann Arbor.
- Ruff, G. A., Sagar, A. D. & Faeth, G. M. (1987) Structure of large-scale pressure-atomized sprays. First Annual Conference of ILASS-Americas, Madison.
- Ruff, G. A., Sagar, A. D. & Faeth, G. M. (1989) Structure and mixing properties of pressure-atomized sprays. AIAA J. 27, 901-909.
- Ruff, G. A., Bernal, L. P. & Faeth, G. M. (1989a) Structure of the near-injector region of non-evaporating pressure-atomized sprays. AIAA Paper No. 89-0050; also J. Prop. Power, submitted.
- Santoro, R. J., Semerjian, J. H., Emmerman, P. J. & Goulard, R. (1981) Optical tomography for flow field diagnostics. Int. J. Heat Mass Trans. 24, 1139-1150.
- Schlichting, H. (1979) Boundary Layer Theory, seventh edition, McGraw-Hill, New York, 234-235; 599.
- Schrock, V. E. (1969) Two-Phase Flow Instrumentation. ASME, New York, 24-35.
- Serizawa, A., Kataoka, I. & Mishigoshi, I. (1975) Turbulence structure of air-water bubbly flow. Int. J. Multiphase Flow 2, 221-225.
- Shearer, A. J., Tamura, H. & Faeth, G. M. (1979) Evaluation of a locally homogeneous flow model of spray evaporation. J. Energy 3, 271-278.
- Shuen, J.-S., Chen, L.-D. & Faeth, G. M. (1983) Evaluation of a stochastic model of particle dispersion in a turbulent round jet. A.I.Ch.E. J. 29, 167-170.
- Shuen, J.-S., Chen, L.-D. & Faeth, G. M. (1983a) Predictions of the structure of turbulent, particle-laden, round jets. AIAA J. 21, 1480-1483.
- Shuen, J.-S., Solomon, A.S.P., Zhang, Q.-F. & Faeth, G. M. (1985) Structure of particle-laden jets: Measurements and predictions. AIAA J. 23, 396-404.
- Shuen, J.-S., Solomon, A.S.P. & Faeth, G. M. (1986) Drop-turbulence interactions in a diffusion flame. AIAA J. 24, 101-108.
- Smith, R. H. & Wang, C.-T. (1944) Contracting cones giving uniform throat speeds. J. Aero. Sci. 11, 356-360.
- Snyder, W. H. & Lumley, J. L. (1971) Some measurements of particle velocity autocorrelation functions in a turbulent flow. J. Fluid Mech. 48, 41-71.
- Solomon, A.S.P., Shuen, J.-S., Zhang, Q.-F. & Faeth, G. M. (1985) Structure of nonevaporating sprays: I. Near-injector conditions and mean properties. AIAA J. 23, 1548-1555. *Ibid.* II. Drop and turbulence properties. AIAA J. 23, 1724-1730.

- Solomon, A.S.P., Shuen, J.-S., Zhang, Q.-F. & Faeth, G. M. (1985a) Measurements and predictions of the structure of evaporating sprays. J. Heat Transfer 107, 679-686.
- Spalding, D. B. (1977) GENMIX: A General Computer Program for Two-Dimensional Parabolic Phenomena, Pergamon Press, Oxford.
- Sun, T.-Y. & Faeth, G. M. (1986) Structure of turbulent bubbly jets. -- I. Methods and centerline properties. Int. J. Multiphase Flow 12, 99-114.
- Sun, T.-Y. & Faeth, G. M. (1986a) Structure of turbulent bubbly jets. -- II. Phase property profiles. Int. J. Multiphase Flow 12, 115-124.
- Sun, T. Y., Parthasarathy, R. N. & Faeth, G. M. (1986) Structure of bubbly round condensing jets. J. of Heat Transfer, 108, 951-959.
- Taylor, G. I. (1940) Generation of ripples by wind blowing over a viscous liquid. Collected Works of G. I. Taylor 3, 244-254.
- Tennekes, H. & Lumley, J. L. (1972) A First Course in Turbulence, The MIT Press, Cambridge, 113-124.
- Uberoi, M. S. & Freymuth, P. (1970) Turbulent energy balance and spectra of the axisymmetric wake. Phys. Fluids 13, 2205-2210.
- Wells, M. R. & Stock, D. E. (1983) The effects of crossing trajectories on the dispersion of particles in turbulent flow. J. Fluid Mech. 136, 31-62.
- Wu, K.-J., Su, C.-C., Steinberger, R. L., Santavicca, D. A. & Bracco, F. V. (1983) Measurements of the spray angle of atomizing jets. J. Fluids Engr. 105, 406-415.
- Wu, K.-J., Coghe, A., Santavicca, D. A. & Bracco, F. V. (1984) LDV measurements of drop velocity in diesel-type sprays. AIAA J. 22, 1263-1270.
- Wygnanski, I. & Fiedler, H. E. (1969) Some measurements in the self-preserving jet. J. Fluid Mech. 38, 577-612.
- Yudine, M. T. (1959) Physical considerations on heavy-particle diffusion. Adv. Geophys. 6, 185-191.